Investigation of Hopped Frequency Waveforms for Range and Velocity Measurements of Radar Targets

Umur Kathree

A project report submitted to the Department of Electrical Engineering, University of Cape Town, in partial fulfilment of the requirements for the degree of Master of Science in Engineering.

Cape Town, August 2014

Declaration

I know the meaning of plagiarism and declare that all the work in the document, save for that which is properly acknowledged, is my own. It is being submitted for the degree of Master of Science in Engineering in the University of Cape Town. It has not been submitted before for any degree or examination in any other university.

Signature of Author .....

Cape Town
26 August 2014

Abstract

In the field of radar, High Range Resolution (HRR) profiles are often used to improve tracking accuracy in range and to allow the radar system to produce an image of an object. This work focuses on the use of HRR profiles generated using a sub-class of HRR techniques termed hopped frequency and stepped frequency waveforms. These wideband waveforms are usually synthesised by combining the spectra of the transmitted pulses in the burst [1]. When used with hopped frequency waveforms, this adds the advantage of range-Doppler decoupling and robustness against electronic countermeasures (ECM) [2, 3]. However these waveforms suffer from high levels of sidelobes [4] and improving the spurious free dynamic range (SFDR) of target measurements was required. This was done with the CLEAN technique [5] which could reduce sidelobe levels to below -60 dB and would allow smaller targets masked by the sidelobes to be uncovered. To analyse the practicality of this work, simulated rotating scatterers were used and these techniques could perform adequately for signal to noise ratios (SNR) above -10 dB and signal to clutter ratios (SCR) above 14 dB. Clutter mitigation is to be investigated in future work to make it applicable to lower SCR and sub-clutter visibility.

Acknowledgements

Firstly I would like to acknowledge and give thanks to the following people:

To Dr Amit Mishra and Willie Nel for supervising my work and providing the technical and academic assistance when I needed it. Further acknowledgement is given to Dr Mishra for teaching the course EEE5105: Fundamentals of Radar Signal and Data Processing and providing me the knowledge needed for this project, and to Prof Mike Inggs for organising these courses and providing the lecturers to impart their knowledge and experience.

To Vanessa Janse van Rensburg for being a mentor and helping me with my day to day tasks as well as giving inputs and feedback to my work, and Annamarie Stanton who provided me with the work to get started with this project and the assistance needed in that regard.

To Jurgen Strydom and Kumaran Naicker for providing me the tools needed for the clutter modelling and simulation.

I would then like to thank the Council of Scientific and Industrial Research (CSIR), more specifically the Defence, Peace, Safety and Security (DPSS) unit, for funding my studies, as well as living expenses, and providing the needed facilities. Special regard here is given to Anria Breytenbach who helped me get my footing at the CSIR and who gave me general assistance from the day I started working there.

I would finally like to thank my family and friends for being the pillar of moral and spiritual support that was needed to get me through this programme.

Contents

List of Figures

List of Tables

Nomenclature

Taken from the IEEE Standard Radar Definitions [6]:

Azimuth—The angle between a horizontal reference direction (usually north) and the horizontal projection of the direction of interest, measured clockwise.

Beam—The formation of radiation into a constrained volume using an antenna.

Doppler radar—A radar that utilizes the Doppler effect to determine the radial component of relative radar target velocity or to select targets having particular radial velocities.

Clutter—Unwanted echoes, typically from the ground, sea, rain or other precipitation, chaff, birds, insects, meteors, and aurora.

Coherent processing interval (CPI)—The time during which the radar signal is received and processed coherently. Such processing is usually for Doppler filtering.

Dwell—A data acquisition interval during which the data is usually processed together for detection or measurement. The radars parameters may be unchanged during the dwell, but often parameters such as the radar frequency, target range, and aspect angle change.

Electronic countermeasures (ECM)—Any electronic technique designed to deny detection or accurate information to a radar. Screening with noise, confusion with false targets, and deception by affecting tracking circuits are typical ECM.

Elevation—In radar, the angle between the line-of-sight in the direction of interest and a horizontal reference plane, measured upwards.

Inverse synthetic aperture radar (ISAR)—An imaging radar in which cross-range resolution (angular resolution) of a target (such as a ship, aircraft, or other reflecting object) is obtained by a synthetic aperture formed by the rotation or translation of the target, as opposed to motion of the radar. Cross-range resolution of target whose exact angular motion is unknown (e.g. non-cooperative targets such as ships at sea) is often achieved by resolving in the Doppler domain the different Doppler frequencies produced by echoes from the individual parts of the object.

Matched filter—A filter that maximizes the output ratio of peak signal power to mean noise power. For white noise, it has a frequency response function that is the complex conjugate of the transmitted spectrum. Its impulse response is the time inverse of the transmitted waveform.

Moving target indication (MTI)—A technique that enhances the detection and display of moving radar targets by suppressing fixed targets. Doppler processing is one method of implementation.

Pulse repetition frequency (PRF)—The number of pulses per unit of time, usually per second, to express the value in Hertz.

Pulse repetition interval (PRI)—The time duration between successive pulses. PRI is the reciprocal of the PRF.

Radar—An electromagnetic system for the detection and location of objects that operates by transmitting electromagnetic signals, receiving echoes from objects (targets) within its volume of coverage, and extracting location and other information from the echo signal. Note that (1) radar is an acronym for radio detection and ranging; (2) radar equipment can be operated with the transmitter turned off, as a passive direction finder on sources radiating within the band of the receiving system.

Range—Distance between a radar and a target.

Range resolution—The ability to distinguish between two targets solely by the observation of their ranges; usually expressed in terms of the minimum range separation at which two targets at the same azimuth and elevation angles can be distinguished and (in the case of Doppler processing) in the same Doppler filter can be distinguished. The required separation should be specified for targets of given relative power level at the receiver. Equal powers are often assumed, but it may be necessary to specify the separation at two or more power ratios where resolution of targets of different powers is important.

Signal to clutter ratio (SCR)—The ratio of target echo power to the power received from clutter sources lying within the same resolution element.

Signal to noise ratio (SNR)—In radar, the ratio of the power corresponding to a specified target measured at some point in the receiver to the noise power at the same point in the absence of the received signal.

Stepped frequency—A radar system that steps the transmission frequency on successive pulses by anything up to its instantaneous bandwidth, usually for the purposes of synthesizing wide bandwidths over a pulse train and therefore high range resolution.

Subclutter visibility—The ratio by which the target echo power may be weaker than the coincident clutter echo power and still be detected with specified detection and false-alarm probabilities. Target and clutter powers are measured on a single pulse return, and all target radial velocities are assumed equally likely.

Target—(A) Specifically, an object of radar search or tracking. (B) broadly, any discrete object that scatters energy back to the radar.

Tracking—The process of following a moving object or a variable input quantity. In radar, target tracking in angle, range, or Doppler frequency is accomplished by keeping a beam or angle cursor on the target angle, a range mark or gate on the delayed echo, or a narrowband filter on the signal frequency, respectively. This process may be carried out manually or automatically for one or more of the preceding input quantities. The beam, range gate, or filter can be either centered on the input quantity or can be coarsely placed, with interpolation measurements

providing accurate data to a computer that does the fine tracking. Tracking may utilize a filter to smooth the measurement data and measure target motion characteristics.

Chapter 1

Introduction

1.1 Background

Tracking as well as imaging operations depend on adequate measurement of the target's range and velocity and the ability to distinguish between individual targets. In practice, High Range Resolution (HRR) techniques are used to finely distinguish scatterers in range and is typically done using wideband stepped frequency modulated (FM) waveforms [1]. Pulse Doppler processing is used to estimate and resolve targets in velocity and this is done with the Fast Fourier Transform (FFT) across many pulses within a Coherent Processing Interval (CPI), with finer velocity resolutions requiring a greater number of pulses. For imaging techniques such as Inverse Synthetic Aperture Radar (ISAR), velocity discrimination is needed to separate the scatterers in cross-range.

This investigation will focus on the use of hopped frequency waveforms to produce HRR profiles for range and velocity estimation. While linear stepped FM waveforms involve transmitting each pulse in the burst by a constant linear offset of the carrier frequency, hopped frequency waveforms involve transmitting these pulses with a randomised order of carrier frequencies. By compensating the phase of the hopped frequency returns at different velocities, the ambiguity response of these waveforms would allow scatterers to be sorted according to their

ranges and velocities [7]. This would allow information from multiple scatterers to be extracted from one target return. Therefore HRR profiles using hopped sequences can be used to provide measurements for tracking algorithms so as to track multiple scatterers, as well as to allow alternative methods for imaging targets according to ISAR. Most importantly these sequences would provide a measure of robustness against electronic countermeasures (ECM) during imaging and tracking operations. However it was found that using hopped frequency waveforms result in high levels of sidelobes which would limit their ability to discern between scatterers [4, 7]. So work is done on developing techniques that would improve the spurious free dynamic range (SFDR) of target measurements using this approach.

1.2 Objective

The problem consists of the following:

- Investigate ways in which to develop techniques that would improve the SFDR of target measurements using HRR profiles generated from hopped frequencies.
- Investigate the applicability of these techniques using hopped frequencies to imaging and tracking.
- Evaluate the performance of these techniques under different interference conditions such as noise and clutter.

1.3 Scope and limitations of work

- This work is limited to simulations done through the use of Octave and real-world data was not considered here.
- The target model is limited to point scatterers having a constant radial velocity.

- Stepped frequency waveforms are used and no specific form of intra-pulse modulation is assumed.

1.4 Plan of development

The report will be laid out as follows:

Chapter 2: This chapter gives an overview of the literature that provides a context to this work. It describes the work done on motion compensation, hopped frequency waveforms and using HRR profiles to do velocity estimation. It also looks at work that was done on waveform design and the CLEAN algorithm that would help in developing techniques to aid the range and velocity measurements.

Chapter 3: This chapter describes the method of range and velocity estimation using motion compensation of HRR profiles. It shows how the hopped frequencies are useful for this method with the disadvantage of high sidelobes. It also discusses issues relating to energy, ambiguity, resolution and noise.

Chapter 4: This chapter discusses the techniques to improve the SFDR of the target measurements. It describes two approaches: apodization and the CLEAN technique. It also describes a way to further improve the CLEAN technique through an optimisation method at the cost of increased computation.

Chapter 5: This chapter describes the incorporation of rotating scatterers into the simulations to touch on application areas such as ISAR and tracking. It shows how the techniques developed in this work are able to resolve those scatterers in down range and cross range. It also tests the performance of these techniques under different dominant scatterer and SNR conditions.

Chapter 6: This chapter looks at the effects of clutter and how the techniques developed in this work apply despite those conditions. The clutter is modelled as correlated Gaussian noise. It also looks at the performance of the said methods for different SCR conditions.

Chapter 7: This chapter summarises and discusses the results presented in this report. It then goes on to discuss future work.

Chapter 2

Literature Review

2.1 Synthetic range profiling and motion compensation

Synthetic Range Profiling (SRP) involves the reconstruction of the target's reflectivity spectrum by combining the spectra of the transmitted pulses in the burst. The IFFT operation is then used to create the HRR profiles [1]. The advantage of this approach is that there would be a lessening of the need for high instantaneous bandwidths and sampling requirements in a radar system. However there would also be a need for increased dwell times and signal processing complexity. Doppler processing is thereafter used to resolve scatterers in the cross range dimension and this forms the radar image in SAR and ISAR operations.

Target motion is shown to create distortion in the HRR profiles. This is due to its radial velocity inducing a linear term in the signal's phase that causes an apparent offset in the peak of the profile, as well as a quadratic phase term (and cubic in the event of target acceleration) that causes a dispersion in the mainlobe. This result in errors in range measurements, mainlobe widening (loss in resolution) and reduction in peak amplitude (loss in SNR) [8, 9, 10].

To mitigate these effects, motion compensation is applied onto the received signals that would attempt to cancel out the velocity term in the signal's phase. This would require accurate estimation of the target's velocity. In [8], this was done through the use of a correlation cost function that detects periodic replicas and uses that in a minimisation to estimate the velocity, provided that the target length does not exceed the range period of the replicas, and the results were comparable to that obtained by the contrast and entropy cost functions. This was extended in [9] where these cost functions were used to jointly estimate the velocity and acceleration of the targets in the HRR profiles. It was also mentioned in [9] that these cost functions do not represent optimal solutions when trying to jointly estimate the velocity and acceleration and the entropy and contrast cost functions gave better performance than the correlation cost functions in this regard.

In [10], an algorithm involving maximum likelihood detection was used to estimate velocity. This was done by estimating the coefficients of the quadrature phase term (QPT) given the signal model. For it to work, the number of scatterers in the target had to be determined beforehand which would pose an issue for non-cooperative targets. This was done using Schwarz's Bayesian approach to determine the dimensionality of a model [11], known as the minimum description length (MDL) criterion. This method was more suitable for dealing with mainlobe distortion in the HRR profiles and less so for range shift errors. Then in [12], to obtain better accuracies than the QPT based methods in [10] and with a focus on range shift compensation, an algorithm using a non-linear least square estimator was proposed. These methods did not address the issue of compensating multiple targets with different velocities as well as extended targets in HRR profiles. But the method in [12] was an attempt to deal with the range-Doppler decoupling issue which is a limitation of using linear stepped FM waveforms.

2.2 Hopped frequency waveforms and ISAR applications

Apart from velocity compensation, the waveform itself also impacts the severity of the velocity effects. To this end, hopped frequency waveforms were investigated to overcome some of the limitations of the linear stepped FM waveform. These sequences offer the benefit of range-Doppler decoupling, reduced range ambiguity, reduced cross-talk between adjacent sensors and less susceptibility to ECM interference [2, 3, 13]. The ambiguity function of hopped frequency waveforms is shown to have a thumbtack characteristic. The main disadvantage of these waveforms is the high levels of sidelobes that are introduced into the profiles as a result of uncompensated target motion [4].

Work has been done on trying to find ways in which to estimate velocity for a hopped FM radar. In [3], an iterative algorithm similar to that in [10] and [12] is used to obtain range and velocity estimates of multiple targets using randomised stepped frequency waveforms. However the number the targets would have to be determined beforehand so the MDL criterion like in [10] was used here. In the context of ISAR operations, a method that measures the dispersion of the signal's energy was used in [2] to estimate velocity i.e the minimum entropy waveform method. This is based on the fact that moving targets in hopped FM radar cause a large dispersion of energy in the HRR profiles, known as the de-focus problem. Using this measure in a cost function, the global minima would suggest the most focused profile and hence where the true velocity would lie. In [13], in order to overcome the de-focus problem, the ISAR image is formed by calculating the generalized Doppler of the echoes, which takes into account the randomised sequences used for frequency modulation. Both range and tangential velocity were considered and dealt with. However the methods in [2] and [13] do not address the compensation of multiple targets. Because of the optimisation processes in the above techniques, they involve considerable complexity and one of the focuses of implementing them practically is to make them more computationally efficient.

In [7], an investigation was done into the use of HRR profiles for estimating the range and velocity of scatterers and to be able to resolve multiple scatterers for tracking purposes. This method involved the following steps:

1. Apply motion compensation to the received signal at different velocities.
2. Form a two-dimensional matrix (in range and velocity) of HRR profiles where each profile is compensated at different velocities.
3. See where the profiles have the most focused mainlobe i.e. no dispersion of the mainlobe energy. The true velocity of the scatterer(s) would likely be found by knowing which velocities those profiles were compensated for.

This work was tested for different types of waveforms and the most promising results for range and velocity estimation were shown for HRR profiles produced from hopped frequency waveforms, due to the range-Doppler decoupling of their thumbtack ambiguity functions.

This method suggests that the range and velocity histories of scatterers are contained in a single profile, as opposed to standard Doppler techniques that require processing from one burst to the next. The use of HRR profiles to track multiple scatterers has been dealt with in [14] where a Bayesian approach involving a Monte Carlo algorithm, known as the particle filter, is used to jointly infer the range and motion parameters of the scatterers in a rotating target. This would aid the ISAR process by compensating for unknown target motion. The method mentioned in [7] would also aid in the tracking process by providing range and velocity measurements of multiple scatterers to a tracking algorithm with the added advantage of frequency diversity.

Besides having the potential to resolve multiple scatterers for tracking purposes, at fine velocity resolutions it would be able to separate the scatterers of a rotating target according to their velocities and this would allow ISAR imaging to be done with hopped frequency waveforms. Unlike the iterative processes of the abovementioned techniques, such as in [3], the range and velocity information is

contained in the HRR matrix of profiles and can be extracted by locating the associated scatterer peak in those profiles.

However, as was mentioned above, it was found that these waveforms suffered from high levels of sidelobes which would limit their ability to resolve between scatterers. It was suggested in [7] that work be done on the design of waveforms and ambiguity functions that would improve on the sidelobe performance of hopped frequency waveforms.

2.3 Waveform design

There have been different approaches to designing waveforms with desired ambiguity functions. In [15], an iterative least squares method is used to approximate to desired ambiguity functions using the minimum mean-square error. This is done using both the complex autoambiguity and complex cross-ambiguity functions. A similar approach was found in [16] where minimising a cost function containing the desired ambiguity function would lead to its approximation. Here the approach was more centred on finding the coefficients of phase modulated waveforms. In [17], the Zak domain is used to design ambiguity functions and its inverse would be taken to obtain the waveform corresponding to that ambiguity function. Using this approach, a hopped FM (and amplitude modulated) waveform was derived that had its sidelobes pushed out leaving an area of ultra-low sidelobes in the vicinity of the peak. This method was extended in [18] with a focus on designing frequency modulated waveforms without the amplitude modulation.

Non-linear frequency modulated waveforms has been considered for ultra-low sidelobe operations. In [19], as part of a design for a satellite-borne weather monitoring radar, a modulation scheme was used where the majority of the waveform was modulated linearly in frequency while the beginning and end portions had higher rates of FM i.e. discrete non-linear FM. Using this scheme, the sidelobes were suppressed to below -60 dB. In [20], the work was extended to investigate continuous non-linear FM and sidelobe suppression to under -70 dB

was achieved. This is one of many approaches that involve mismatch filtering which is well known in controlling the sidelobes, at a cost of loss in SNR and resolution.

2.4 Mismatched filtering

An example of work done on mismatched filtering is in [21] where filter coeffiecients were optimised using the sidelobe measure (L_P-norms) as cost functions. Here mismatch lengths of up to 100% were used and they gave better sidelobe suppression than matched filtering but at a loss in resolution, known as mismatch loss. Complementary sequences are also an example of mismatched filtering. An example of this are the Golay codes which are a set of two binary sequences introduced by Marcel Golay that gave perfect autocorrelation qualities [22]. Work was done in [23] to create Golay complementary phase-coded sequences that would have resilience for modest Doppler shifts.

The well known window functions described in [24] i.e. Hamming, Hanning, Blackman, etc are an example of mismatched filtering in amplitude. At a cost of increased complexity, non-linear techniques of amplitude weighting are used in order to decouple the sidelobe reduction from the loss in resolution. For example, multi-apodization mentioned in [25] and [26] would use two or more windows (eg. rectangular and Hanning) per sample and the minimum output would be chosen for that sample. This would result in the lower sidelobes of the windowed signal while preserving the mainlobe width of the unwindowed signal. Although due to taking the minimum output, the lower peak value is chosen and it therefore does not mitigate the SNR loss.

2.5 CLEAN technique

When dealing with radio imagery, one technique to deconvolute the spread of energy that dominant pixels contribute to the image is through the CLEAN

technique that was introduced by Högbom for radio interferometry [5]. It does this by finding the highest pixel, generating its point spread function and subtracting that energy from the image. It then repeats the operation for successive pixels. In [27], the CLEAN technique was applied for coherent microwave imaging with the aim of dealing with grating sidelobes resulting from thinned out antenna arrays. This approach is useful for faint targets that are masked by the sidelobes of the more dominant ones and it can help to improve the target dynamic range. A modified version of the CLEAN technique, known as statistical CLEAN, was developed in [28] in order to detect scatterer centres in ISAR images. Here a detection algorithm, known as a Gaussianity test, is used to reduce the likelihood of false alarms and lighten the computational burden. An attempt to apply this method to extended targets is through another version of the CLEAN technique, known as Sequence CLEAN [29], that uses a tree search algorithm to find the best possible sequence to cancel the sidelobes from scatterer peaks. This is based on the possibility that a peak may be an artifact resulting from the constructive interference of sidelobes and a smaller peak may be from a real target. Because search algorithms are in use here, this work was extended in [30] to make use of a genetic algorithm to find the optimal sequence of sidelobe cancellation.

2.6 Conclusion

Wideband stepped FM waveforms are used in practice when profiling targets using HRR techniques. However in the event of target motion, these profiles suffer from range shift and distortion of the mainlobe which causes errors in range measurement and resolution loss. Therefore different techniques are used to compensate for this motion such as the correlation cost function or using a maximum likelihood detection algorithm to estimate the QPT terms in the signal. These methods make use of linear stepped FM waveforms and range-Doppler coupling is one of their limitations. Methods such as [12] attempt to deal with this issue by focusing on range shift compensation.

Therefore hopped frequency waveforms were investigated to overcome this range-Doppler decoupling due to their thumbtack ambiguity functions and to provide other advantages such as reduced interference between sensors and frequency diversity that would be useful against ECM. However these waveforms suffer from high sidelobes that are introduced into the profiles as a result of uncompensated target motion. And due to the thumbtack characteristic of hopped frequencies, target motion would also cause the mainlobe to disperse rapidly, known as the defocus problem. So different iterative methods such as in [2] and [13] were investigated in the context of ISAR that would use this mainlobe dispersion to estimate the velocity i.e. the entropy method. The method in [3] is another iterative algorithm applied to hopped FM that attempts to deal with multiple targets.

Then there is the approach in [7] that applies motion compensation to HRR profiles at different velocities and this would form an array of profiles where the velocity can be estimated by seeing where these profiles have the most focus. This method works well in conjunction with hopped frequency waveforms due to their thumbtack ambiguity functions and was investigated specifically for obtaining measurements of multiple scatterers. A comparable method to this is in [3] that also deals with multiple targets for a hopped FM radar. However this method has the limitation that the number of iterations would be dependent on the number of scatterers known in the target and this would have to be determined beforehand using a Bayesian approach. The method in [7] however allows this information to be contained in the set of HRR profiles itself which can be extracted by locating the most focused profiles and their peaks. This method can also be applied onto rotating scatterers to resolve them in range and velocity so that ISAR imaging can be done. Therefore this is the approach that is dealt with in this work since it has potential applications to tracking of multiple targets and ISAR imaging and doing so with hopped frequency waveforms that would be useful against ECM. This approach and the issues thereof will be elaborated in Chapter 3.

However the high sidelobes that come with hopped frequencies still remain an issue and methods to design particular sequences of hopped frequency waveforms were investigated to help overcome this problem. This would require designing

waveforms with desired ambiguity functions that would maintain their thumb-tack ambiguity functions but would have their sidelobes pushed out so that they dont interfere with adjacent scatterers. This could be done using Zak domain methods or different mismatched filtering approaches such as (L_P-norms) and apodization. The CLEAN approach is another method of dealing with the side-lobe issue since each scatterer in the image contributes their own set of sidelobes.

Even though these waveform design methods such as the Zak domain still have the potential to be investigated to yield desired waveforms that can be used in conjunction with the approach in [7], in this work the apodization and CLEAN approaches are investigated as initial attempts to deal with the sidelobe problem of hopped frequencies. One reason for this is that instead of trying to yield a particular set of hopped frequencies that the waveform design methods entail, the above techniques can be applied for any hopped frequency sequence and would therefore preserve the frequency diversity that is needed in ECM conditions. It will firstly be shown in this work that different sets of hopped frequency sequences correspond to different sidelobe locations in the HRR profiles. Apodization can be used to combine the results from different transmitted hopped frequency sequences to form an overall set of profiles with lower sidelobe levels. And secondly, a CLEAN algorithm will be utilised based on the transmitted time and hopped frequency sequences as well as the estimated range, velocity and amplitude of the scatterers. This would allow the sidelobe response of each scatterer to be generated and would subtract from the profiles to reduce the sidelobes that come with hopped frequencies. These techniques will be described in Chapter 4.

Chapter 3

HRR Formation and Compensation

3.1 Introduction

This chapter describes the use of HRR profiles to do range and velocity estimation as mentioned in [7] and forms the basis of this work. Issues such as sidelobes, ambiguity, resolution and noise are also looked at.

3.2 Overview of theory

To form an HRR profile from a signal, we consider a burst of N pulses transmitted from a radar, each with a centre frequency of $f(m)$. For a target consisting of M scatterers, and assuming the target return falls into one coarse range sample, the signal can be modelled by:

$$S(m) = \sum_{s=1}^{M} A_s \exp(\frac{-j4\pi f(m)(R_s + v_s t(m))}{c}) \tag{3.1}$$

where c is the speed of light, A_s is the amplitude of the individual scatterer, t is the time of the return sampled by the PRI of each pulse in the burst and R_n and v_n are the respective range and velocity of the individual scatterer [7, 10]. A constant v_s is used as each scatterer is assumed to be moving radially with a constant range rate.

As was mention in Chapter 2, target motion will create distortion due to the induced velocity terms in the phase [8, 9, 10]. This can be seen when multiplying out the phase in Equation 3.1:

$$S_{phase}(m) = \frac{-j4\pi}{c}(f_1 R_s + (f_1 v_s(PRI) + \Delta f R_s)m + \Delta f v_s(PRI)m^2) \tag{3.2}$$

where $f(m) = f_1 + m\Delta f$, f_1 being the frequency of the first transmitted pulse and Δf being the frequency step size, and $t(m) = m(PRI)$ assuming a uniform PRI of the transmitted pulses. For the linear stepped FM waveform, the term in Equation 3.2 that is linear in m will create an offset in the peak and will cause errors in range measurements. The term that is quadratic in m will create a dispersion of the peak that will cause mainlobe widening and amplitude loss. Therefore to compensate for the motion term in the signal phase, $S(m)$ is multiplied by the following:

$$V(m) = \exp(\frac{j4\pi v_{est} f(m) t(m)}{c}) \tag{3.3}$$

where v_{est} is the estimated velocity for which $S(m)$ should be compensated for. This results in the signal:

$$P(m) = \sum_{s=1}^{M} A_s \exp(\frac{-j4\pi f(m)(R_s + v_{er} t(m))}{c}) \tag{3.4}$$

where $v_{er} = v_s - v_{est}$ is the residual velocity, the ideal being $v_{er} = 0$. Thereafter, the Inverse Discrete Fourier Transform (IDFT) is applied onto the resultant signal, to translate the frequency signal $P(m)$ into the time domain, and this forms the HRR profile.

On reception of the target return, $S(m)$ would be multiplied by $V(m)$ for different motion compensation terms v_{est} and an array of HRR profiles would be formed. The profile with $v_{er} = 0$ would have the most focus, due to the cancelling of the linear and velocity terms in Equation 3.2, and the velocity compensation v_{est} that formed that profile would be the most likely velocity of the scatterer.

For the multiple scatterer case, the scatterers contribute independently to the formation of the profiles due to the linearity of Equations 3.1 and 3.4. Ideally, this would show different areas of focusing in the HRR profiles that would correspond to the different scatterer velocities and hence a way to descern between them.

3.3 HRR profiling using hopped frequency waveforms

To demonstrate the method of range and velocity estimation using HRR profiles, two waveform cases will be considered: the linear stepped frequency waveform and the hopped frequency waveform. The hopped frequency waveform was generated from the linear stepped frequency waveform by randomising its indices. These waveforms are shown in Figure 3.1. The results were generated using Octave.

The waveforms were generated with the parameters, used in [7], of 256 frequency steps, 256 MHz bandwidth, a centre frequency of 5 GHz and a PRF of 1 kHz. Then the HRR profiles were formed by the IDFT after applying the motion compensation. The velocity estimation was stepped from 0 to 10 m/s in 200 steps. The results for the two waveform cases were generated and is shown in Figure 3.2. The assumed target is a single point scatterer at a range of 80 m from the radar having a velocity of 4 m/s. The Blackman window was used to weight the return before the IDFT to help reduce the sidelobes.

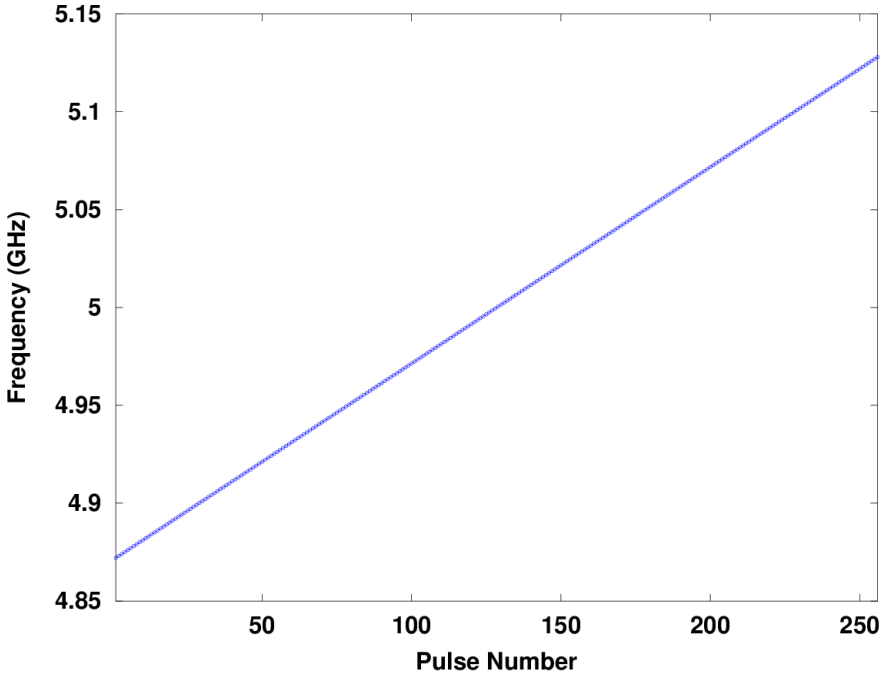

(a) Linear stepped frequency waveform

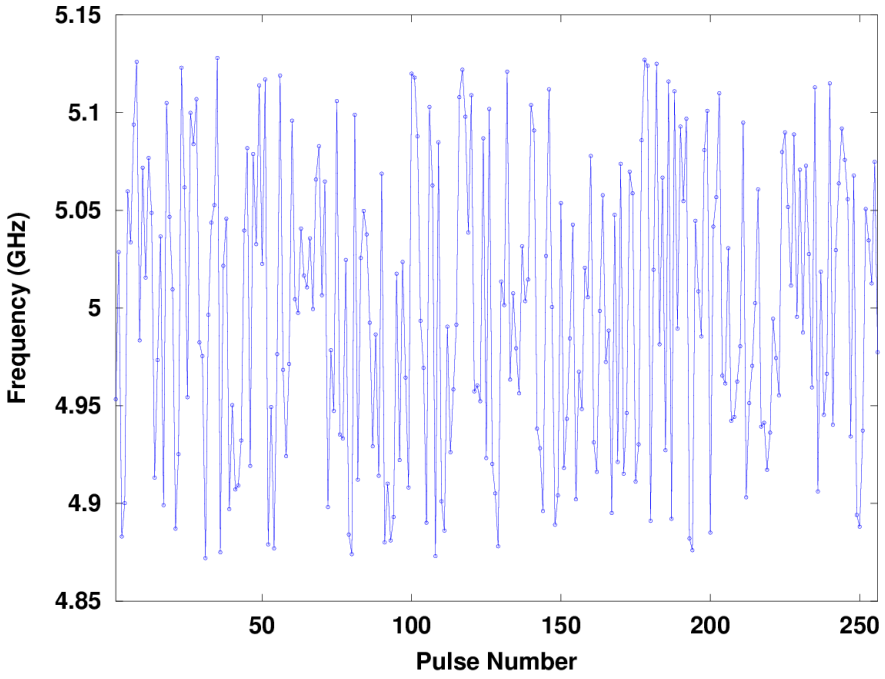

(b) Hopped frequency waveform

Figure 3.1: Plots showing the two waveforms for comparison

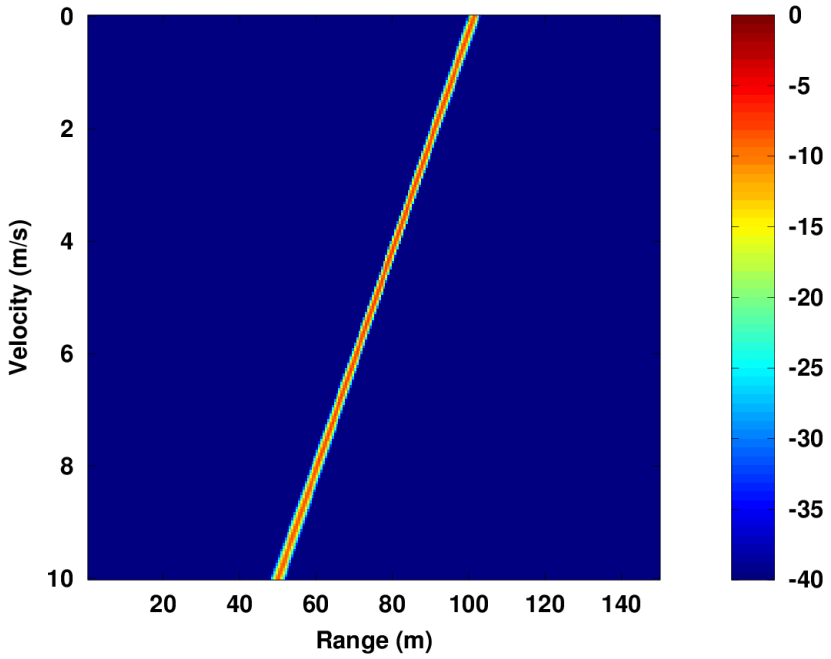

(a) Linear stepped frequency waveform

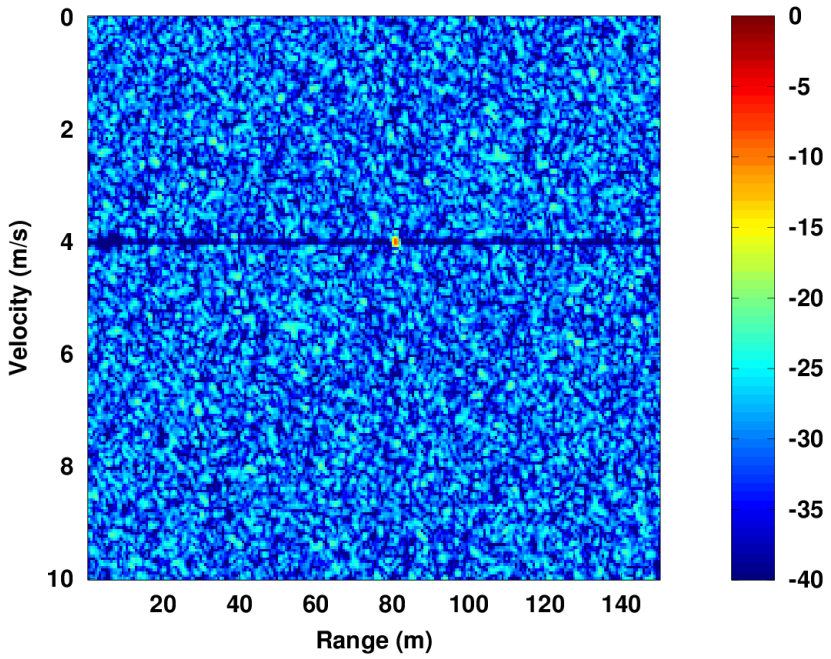

(b) Hopped frequency waveform

Figure 3.2: HRR profile results for scatterer at 80 m range and 4 m/s velocity

The diagonal ridge in Figure 3.2(a) is due to the offset in range that the linear component in Equation 3.2 induces in the profile, as well as some dispersion of the mainlobe at higher offsets due to the quadratic phase term. While the range and velocity of the scatterer could be determined by finding the narrowest portion of the mainlobe ridge, this is not an accurate indication of those parameters.

For the hopped frequency case, shown in Figure 3.2(b), a peak is shown at the correct range and velocity of 80 m and 4 m/s respectively. When using the hopped frequency waveform for generating HRR profiles, care has to be taken to reorder the samples of the return (Equation 3.1) to linearise its frequencies. This would allow the IDFT operation to be performed. The reordering of $S(m)$ to linearise the frequency vector $f(m)$ would result in a scrambling of the time vector $t(m)$ so the randomisation that comes with the hopped frequency waveform is preserved. This randomisation causes a complete dispersion of the mainlobe energy into the sidelobes except at the correct velocity where $v_{er} = 0$. At this point $t(m)$ gets cancelled out and this removes the randomisation component. Therefore a focused HRR profile is formed after the IDFT and with this information, the range and velocity of the scatterer can be determined more accurately than when using the linear stepped frequency waveform. Further examples of this is shown in Figure 3.3. Each result was generated using a different sequence of hopped frequencies.

To apply this method to a multiple scatterer scenario, and to see if it is able to distinguish between them as this would be required for imaging and tracking operations, three point scatterers are used that are of equal amplitude having ranges of 20, 80 and 120 m and velocities of 2, 4 and 8 m/s respectively. Forming the HRR profiles after applying motion compensation, the result is shown in Figure 3.4.

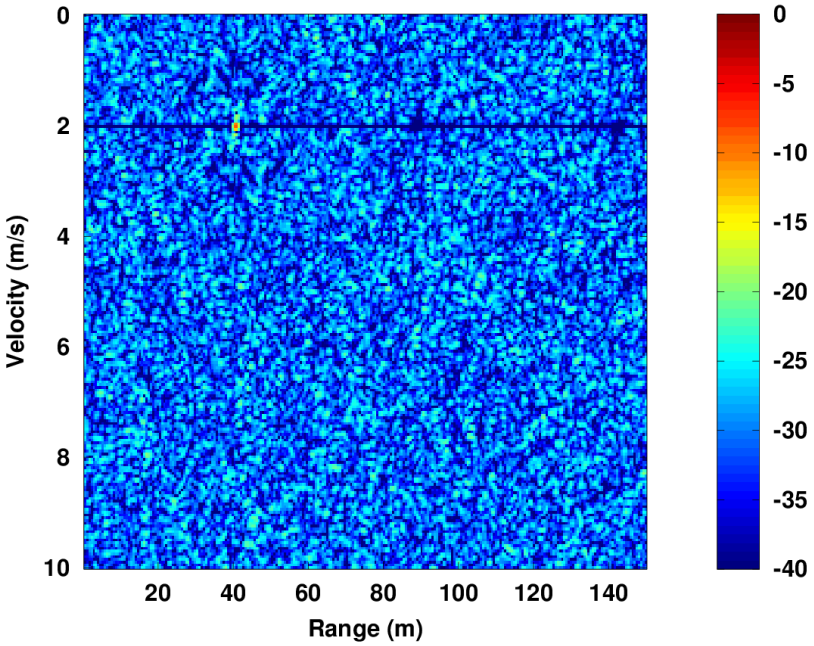

(a) Range: 40 m Velocity: 2 m/s

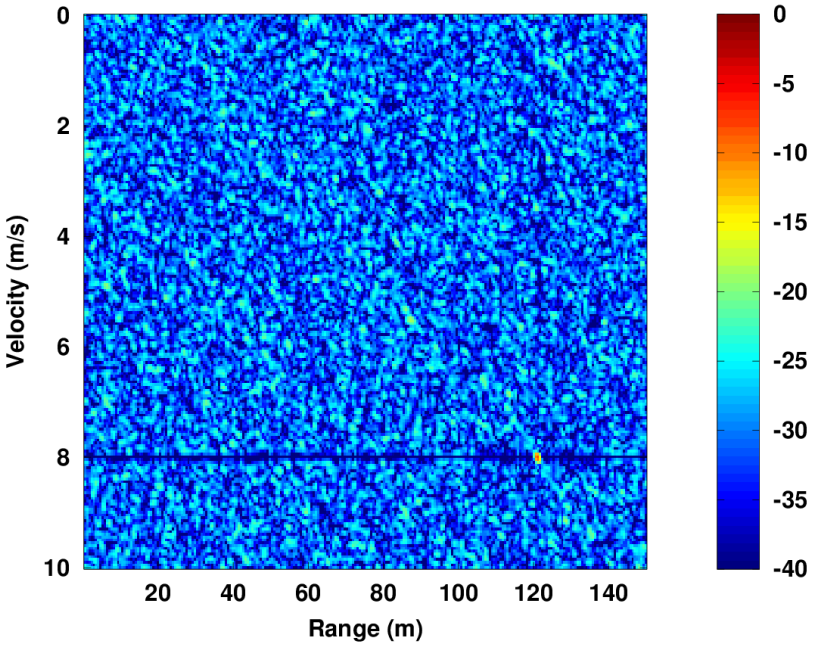

(b) Range: 120 m Velocity: 8 m/s

Figure 3.3: Further examples of parameter estimation using hopped FM sequences

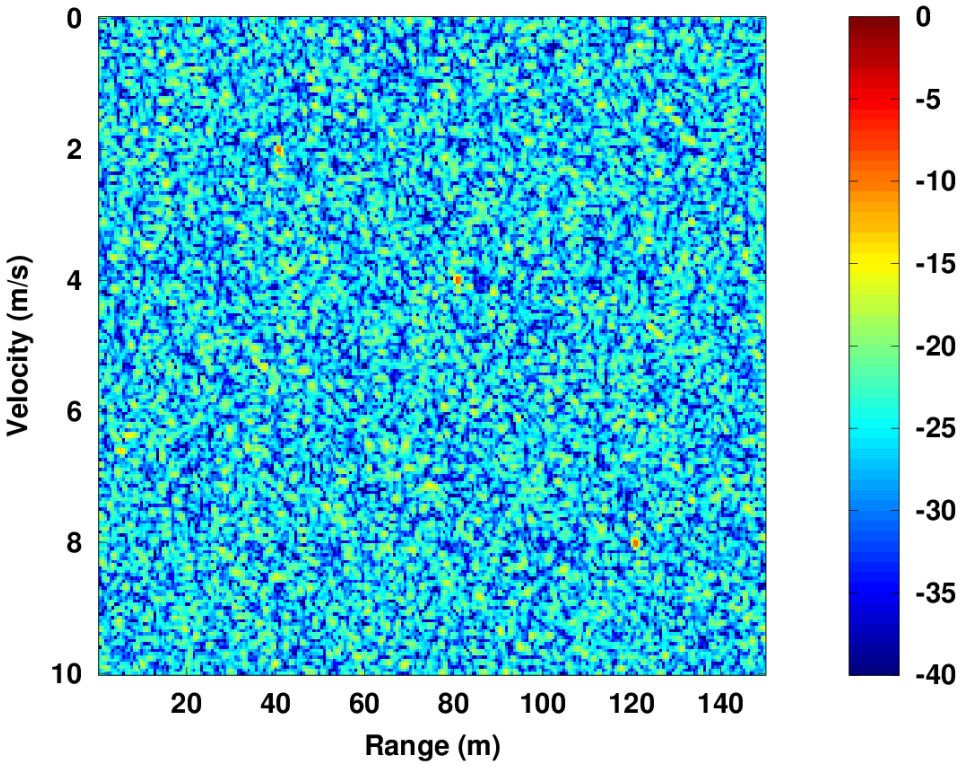

Figure 3.4: Result for target scenario with scatterers at 40 m, 80 m and 120 m range and 2 m/s, 4 m/s and 8 m/s velocity respectively

The peaks corresponding to the ranges and velocities of the target scatterers can be seen but against the backdrop of a higher noise floor i.e the SFDR in this case is significantly less. As was mentioned in Section 3.2, the linearity in Equations 3.1 and 3.4 shows that this result is the superposition of the results for the three individual scatterers. It also means that the increased noise floor is due to the sidelobe contribution of those scatterers. This would pose a risk for smaller scatterers being masked by the sidelobes of the larger ones.

Although the three scatterers are discernible making it possible for the target to be imaged, the high level of sidelobes would obscure the operation. For tracking applications, the localised target would risk being lost due to obtaining measurements in this high noise floor.

3.4 Target energy and sidelobes

To give an idea of the behaviour of the energy in the profiles, $P(m)$ from Equation 3.4 can be split into its range and velocity components:

$$P(m) = \exp(\frac{-j4\pi f(m)R}{c}).\exp(\frac{-j4\pi f(m)v_{er}t(m)}{c}) \tag{3.5}$$

assuming a single point scatterer of unity amplitude. The formula for the IDFT is:

$$x[n] = \frac{1}{N}\sum_{k=1}^{N} X[k]\exp(\frac{j2\pi nk}{N}) \tag{3.6}$$

where the discrete frequency domain signal $X[k]$ of N samples is transformed to the discrete time domain signal $x[n]$. When the IDFT is used to form the HRR profiles from the signal in $P(m)$, the resultant signal (at different compensated velocities v_{er}) is:

$$H(n, v_{er}) = \frac{1}{N}\sum_{k=1}^{N} \exp(\frac{-j4\pi f(k))R}{c}).\exp(\frac{j2\pi nk}{N}).\exp(\frac{-j4\pi f(k)v_{er}t(k)}{c}) \tag{3.7}$$

where k is used instead of m to suit the IDFT operation. $H(n, v_{er})$ mathematically describes the placement of energy in the HRR profiles and is in fact a formula for the results shown in Figures 3.2, 3.3 and 3.4, with velocity v_{er} on the one axis and the range $r = cn/2B$, B being the signal bandwidth, on the other axis. Equation 3.7 shows that for a single point scatterer, its energy placement in the profiles can be reproduced by using the transmitted frequencies $f(k)$, the transmitted times $t(k)$, the estimated scatterer range R and the estimated scatterer velocity v_{er} to generated $H(n, v_{er})$. $H(n, v_{er})$ would be scaled by a factor A to approximate to the correct reflectivity (amplitude) of the scatterer.

The results in Figure 3.2 show that $H(n, v_{er})$ is also the ambiguity function for the waveforms shown in Figure 3.1. This can be seen by looking at the form of

the ambiguity function:

$$\chi(\tau,\nu) = \int_{-\infty}^{\infty} X(t)X^*(t-\tau).\exp(j2\pi\nu t)dt \tag{3.8}$$

and seeing that Equations 3.7 and 3.8 resemble each other. In Equation 3.7, the matched filtering is performed by the IDFT operation and the term containing v_{er} is similar to the Doppler term $e^{j2\pi\nu t}$ in the ambiguity function. The peak that is seen in Figure 3.2(b) is due to the ambiguity function for the hopped frequency waveform having a thumbtack characteristic. For the multiple scatterer case, this results in a superposition of $H(n, v_{er})$ for different scatterers as was seen in Figure 3.4. This sidelobe response that forms for each point scatterer is analogous to the point spread function that each point source would convolve with an imaging system.

Further analysis can be done by considering the total energy present in the profiles. To calculate the total energy, the following formula is used:

$$E = \sum_{n=1}^{N} |H(n, v_{er})|^2 \tag{3.9}$$

This is done for each profile at the different compensated velocities and is shown in Figure 3.5. Figure 3.5(b) shows that the total energy is at a constant -10.36 dB and does not change across the profiles. Therefore the change of the phase of the signal that is done with motion compensation does not change the energy content, but merely the distribution of that energy. At the correct velocity where the point of focusing occurs, most of the energy is gathered at the mainlobe and this leaves a null area throughout the rest of the profile. The total energy itself is affected by the reflectivity of the scatterer and the windowing operation which induces a loss in signal energy.

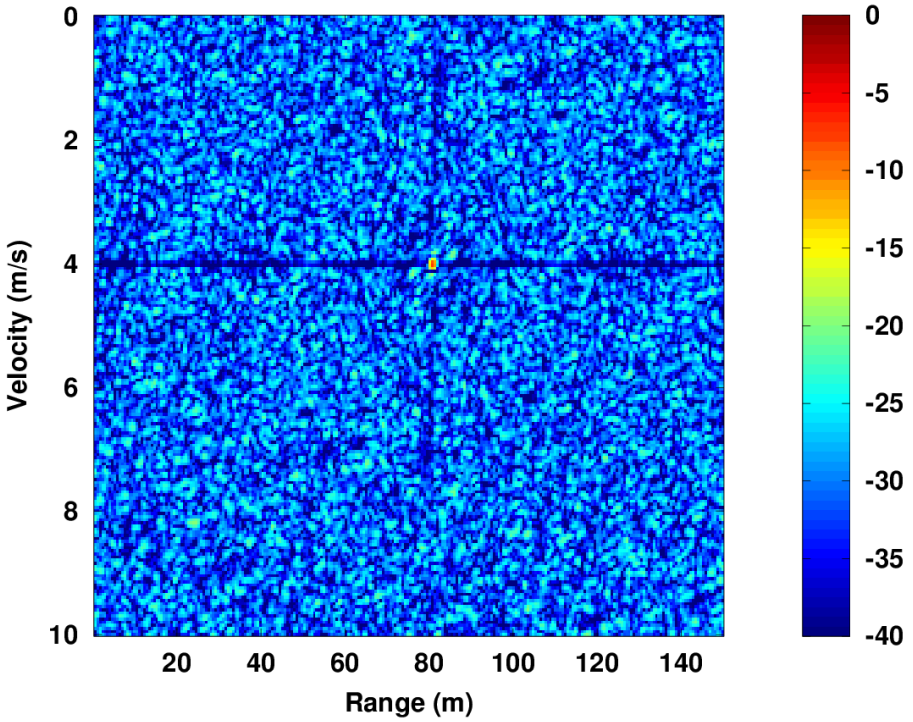

(a) HRR profiles

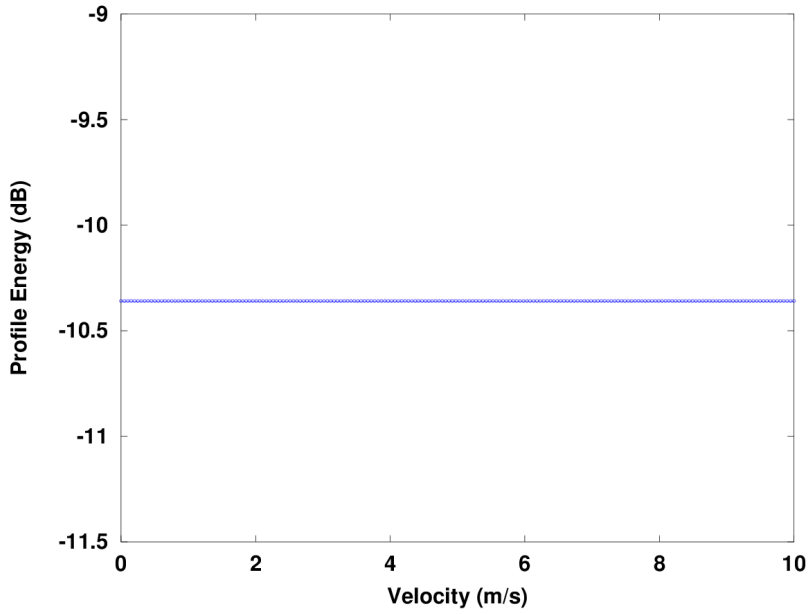

(b) Profile energy

Figure 3.5: Plot of total energy for each profile at different velocities

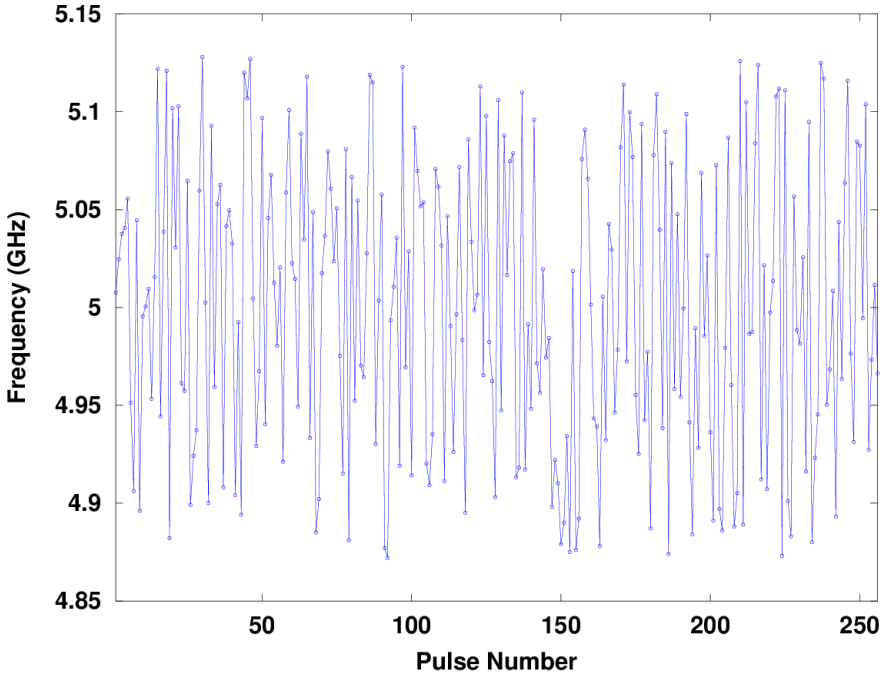

(a) Waveform A

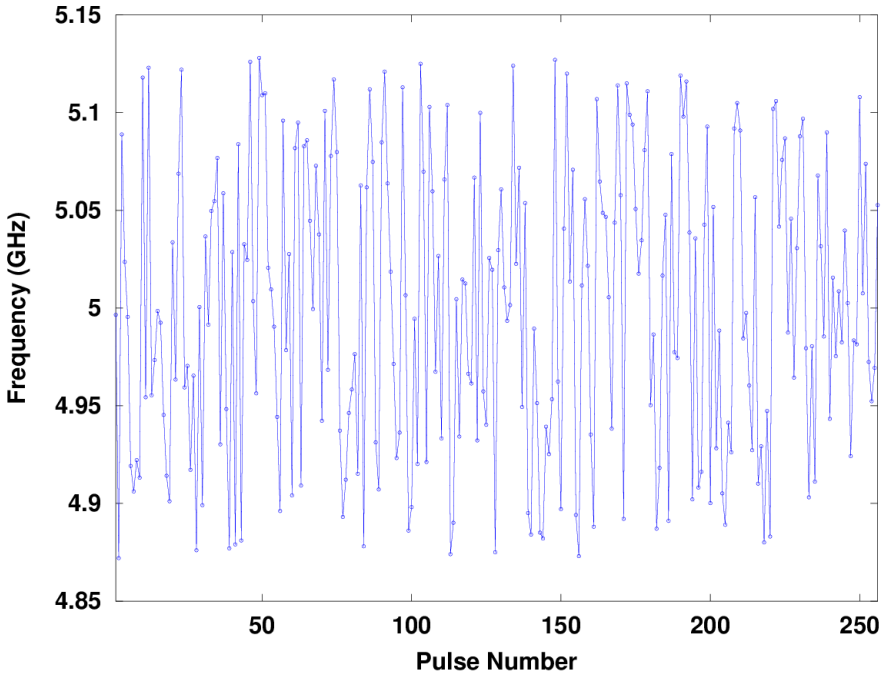

(b) Waveform B

Figure 3.6: Plots showing the two hopped frequency waveforms for comparison

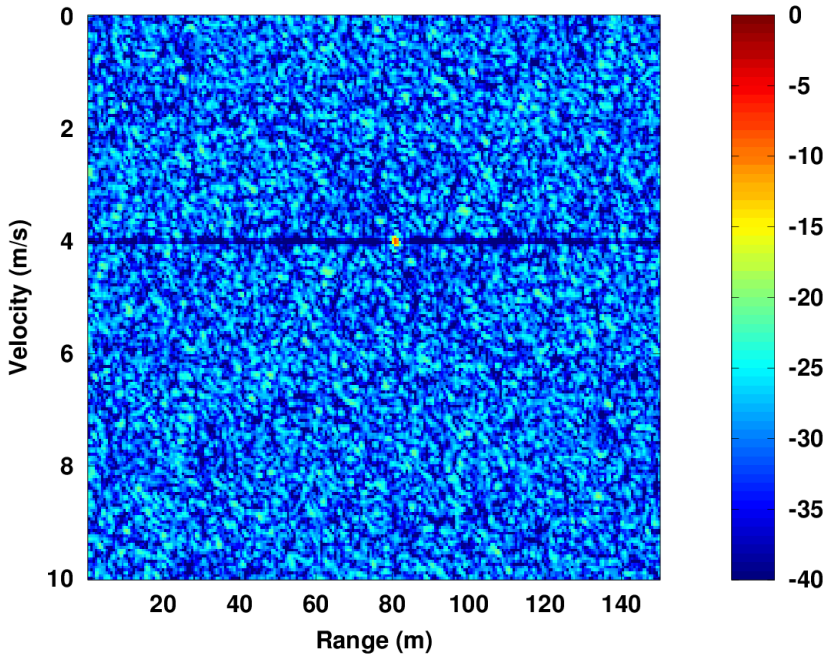

(a) Waveform A

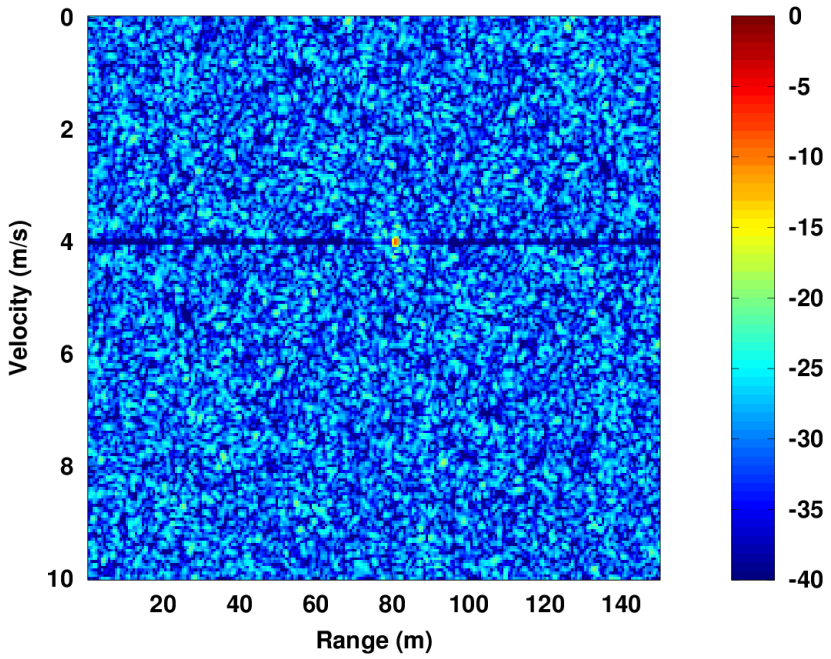

(b) Waveform B

Figure 3.7: Profile comparison for hopped frequency waveforms

Frequency modulation also involves a change in the signal's phase. This is the case when the frequencies are randomised in the modulation. Therefore different sequences of frequencies transmitted in the burst would yield different distributions of energy in the profiles. This is seen in Figure 3.7 where the profiles show a change in the placement of sidelobes between the two hopped frequency waveforms plotted in Figure 3.6. Alternatively, it can be said that the two waveforms result in different ambiguity functions.

3.5 Ambiguity and resolution of range and velocity

When forming the HRR profiles, the unambiguous range interval is determined by:

$$R_{amb} = \frac{c}{2\Delta f} \tag{3.10}$$

where Δf is the frequency step size. Here Δf is the sampling interval of the frequency domain input signal during the IDFT operation and this makes the time (range) domain HRR profile periodic beyond R_{amb}. Any returns beyond R_{amb} would fold back into the unambiguous range interval as a result of aliasing and this would create ambiguity in range.

Figure 3.8 shows how the range ambiguity is affected by the frequency step size. At 1 MHz, R_{amb} is 150 m and this is seen in Figure 3.8(a) where the scatterer at 80 m has a repeated artifact at 230 m. For the 2 MHz case, Figure 3.8(b) shows the scatterer having more repeated artifacts, spaced at $R_{amb} = 75$ m, within the same 250 m window. One artifact is shown folded into the 5 m range bin as a result of this aliasing. Therefore in practice, it is important that the target undergoing HRR profiling is not wider than this unambiguous range interval.

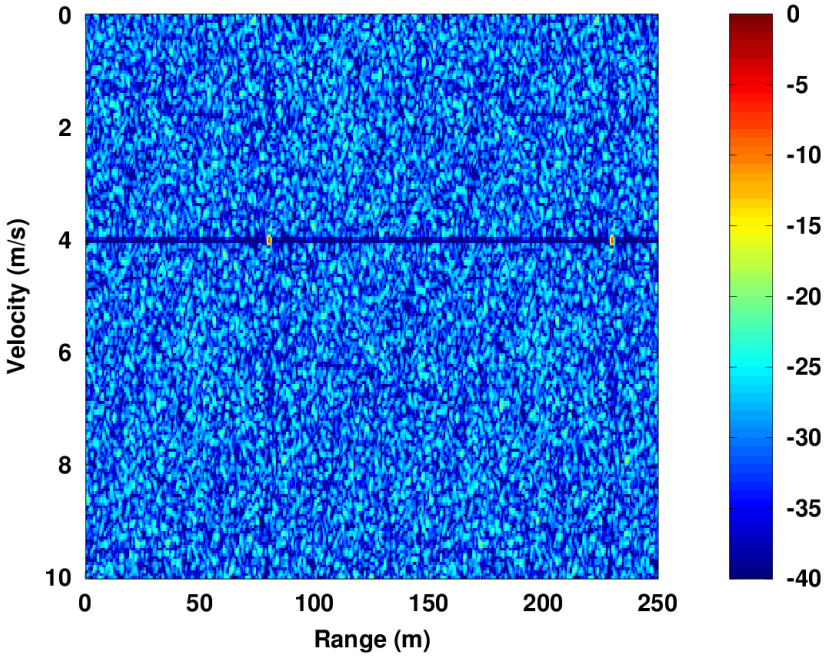

(a) 1 MHz

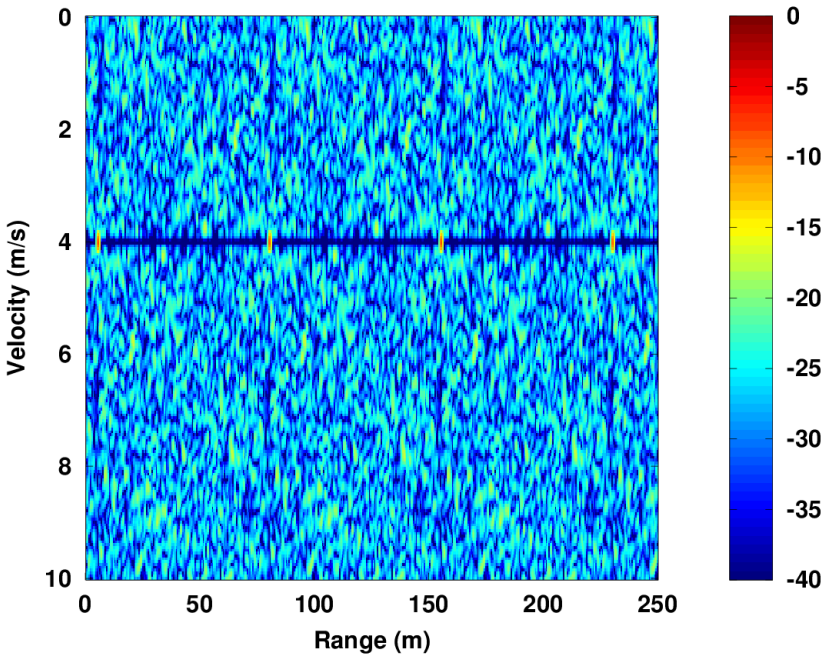

(b) 2 MHz

Figure 3.8: Plots showing range ambiguity for different frequency step sizes

Looking at velocity ambiguity, we know from conventional Doppler processing that it is determined by:

$$v_{amb} = \frac{\lambda_c}{2(PRI)} \tag{3.11}$$

where λ_c is the operating wavelength of the radar. Since the Doppler shift is determined by velocity i.e $f_d = 2v/\lambda_c$, the PRF is the sampling frequency when the FFT is taken across the slow-time data and would therefore be the unambiguous velocity interval in the Doppler domain. For conventional linear stepped FM processing, the FFT is taken over many HRR profiles and the Burst Repetition Frequency i.e. $BRF = PRF/N$ is what determines the sampling frequency and hence velocity ambiguity.

Equation 3.11 can also be shown to apply to the method of range and velocity estimation described in this work. There is also a difference in velocity ambiguity behaviour when compared to conventional Doppler processing and this is shown in Figure 3.9.

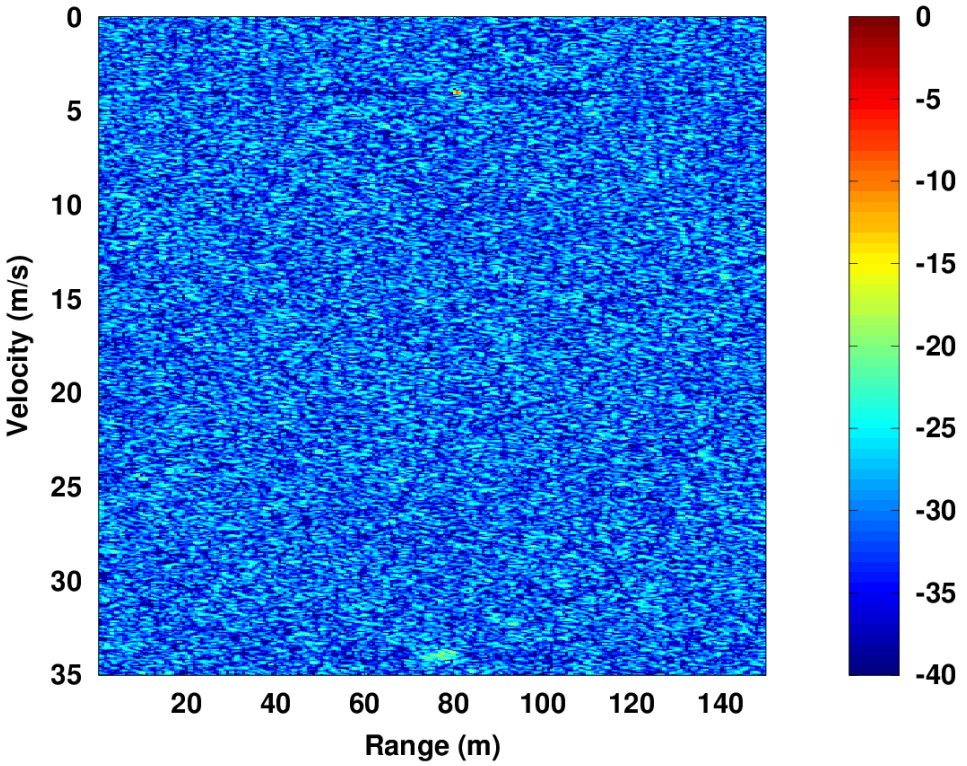

Figure 3.9: Velocity ambiguity for PRF of 1 kHz and 5 GHz centre frequency

At 1 kHz PRF, with $v_{amb} = 30$ m/s, the scatterer at 4 m/s shows an artifact at 34 m/s. However, instead of there being an exact replica of the peak at 4 m/s, the peak at 34 m/s is shown to be dispersed. To explain this, we go back to Equation 3.5 and make $v_{er} = v + v_{amb}$:

$$P(m) = \exp(\frac{-j4\pi f(m)R}{c}).\exp(\frac{-j4\pi f(m)(v + v_{amb})t(m)}{c}) \tag{3.12}$$

We then focus on the velocity terms and split them up between the scatterer velocity and the ambiguous velocity:

$$P_{vel}(m) = \exp(\frac{-j4\pi f(m)vt(m)}{c}).\exp(\frac{-j4\pi f(m)v_{amb}t(m)}{c}) \tag{3.13}$$

In order for there to be an exact replica of the peak at the ambiguous velocity:

$$\begin{aligned} &\iff \exp(\tfrac{-j4\pi f(m) v_{amb} t(m)}{c}) = 1 \\ &\iff \exp(\tfrac{-j4\pi f(m) c t(m)}{c f_c 2(PRI)}) = 1 \\ &\iff \exp(\tfrac{-j2\pi f(m) t(m)}{f_c (PRI)}) = 1 \end{aligned} \tag{3.14}$$

where $\lambda_c = c/f_c$. This requires:

$$\frac{f(m)t(m)}{f_c(PRI)} = i(m) \tag{3.15}$$

where $i(m)$ is a vector of integer values. Assuming a uniform PRI throughout the burst, $t(m)/(PRI)$ would yield a vector of integer values. However this is not the case for the term $f(m)/f_c$. Since the frequencies in the burst will vary within a certain bandwidth around the centre frequency:

$$\frac{f_c \pm B/2}{f_c} = 1 \pm \frac{B}{2f_c} \tag{3.16}$$

where $B/2f_c$ is the most that the pulse frequency can offset from the centre frequency. Therefore $f(m)/f_c$ will have its values vary around an integer, the worst case variation being $B/2f_c$, and this causes the dispersion of the peak seen at the ambiguous velocity in Figure 3.9. Therefore the smaller the ratio $B/2f_c$ is, the more $f(m)/f_c$ will have its values approximate to an integer. This means that the centre frequency will have to be made large in comparison to the bandwidth i.e $f_c \gg B$.

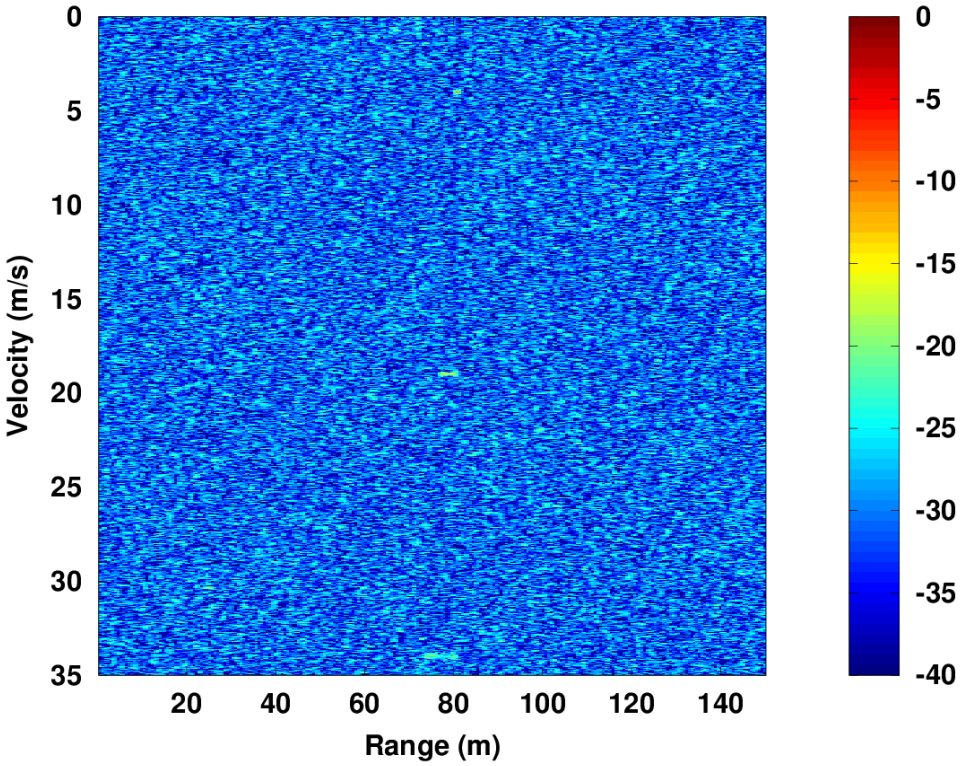

Figure 3.10: Velocity ambiguity for PRF of 1 kHz and 10 GHz centre frequency

Figure 3.10 shows the ambiguous velocities when using a centre frequency of 10 GHz. This makes $v_{amb} = 15$ m/s and the scatterer at 4 m/s would have artifacts at 19 m/s and 34 m/s. Here the same bandwidth is used so that $B/2f_c$ is smaller and the artifact at 19 m/s is more focused compared to the artifact at 34 m/s. The reason that the artifact at the second ambiguous velocity of 34 m/s is more dispersed is because at $2 \times v_{amb}$, this results in $2(B/2f_c)$ and therefore a greater variance of $f(m)/f_c$ from integer values.

Then we look at resolution of range and velocity. In the range domain it is determined by the bandwidth of the entire burst:

$$\Delta r = \frac{c}{2B} \tag{3.17}$$

This is the resolution after HRR profiling and is also known as the fine range resolution. We also know that in Doppler processing, the Doppler resolution is determined by the number of pulses processed in a CPI (which is also the number of slow-time samples when taking the FFT):

$$f_{d\_min} = \frac{PRF}{N} = \frac{1}{(PRI)N} \tag{3.18}$$

Using the Doppler shift $f_d = 2v/\lambda_c$, the velocity resolution is therefore:

$$v_{step} = \frac{f_{d\_min}\lambda_c}{2} = \frac{\lambda_c}{2(PRI)N} \tag{3.19}$$

It should again be mentioned that for linear stepped FM processing, the FFT is taken over many HRR profiles and this means the BRF determines the sampling of the FFT. Therefore $f_{d\_min} = BRF/N = PRF/N^2$.

The velocity resolution described in Equation 3.19 does apply to the method of range and velocity estimation described in this work. To see why this is the case, we go back to Equation 3.7 and look at its phase terms (normalised by $j2\pi$):

$$H_{phase}(n, v_{er}) = \frac{nk}{N} - \frac{2f(k))R}{c} - \frac{2f(k)v_{er}t(l)}{c} \tag{3.20}$$

Since hopped frequencies are the concern here, the frequencies would have to be reordered so that the IDFT operation can take place. As was mentioned in Section 3.3, reordering the hopped $f(k)$ would cause the linear time vector $t(k)$ to be scrambled. Therefore k is an ordered vector of indices from 1 to N whereas l is a randomised order of indices from 1 to N.

The DFT is a matched filtering operation that involves a correlation of the frequency of the signal. At the target range bin, matching occurs due to the alignment of the resultant phasors during the coherent summation and this gives rise to the peak amplitude value in the DFT operation, shown at point A_1 in Figure 3.9. The mainlobe amplitude reduces when the phasors move out of

alignment and this is shown at the points A_2 and A_3. For phasors normalised by $j2\pi$, the maximum that the phasors are allowed to vary from alignment before the peak disperses completely is 0.5.

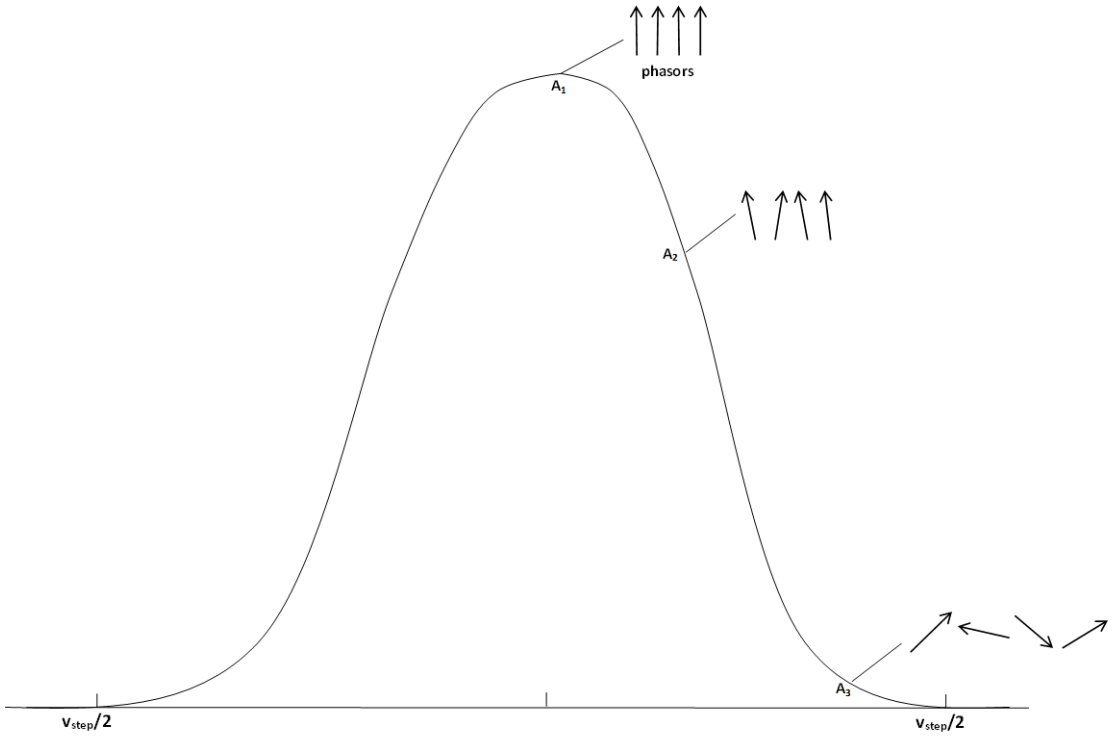

Figure 3.11: Effect of phasors on mainlobe amplitude after IDFT

Using this as the basis to explain velocity resolution, we go back to Equation 3.20 and let $f(k) = f_1 + k\Delta f$, f_1 being the lowest frequency in the burst:

$$H_{phase}(n, v_{er}) = \frac{nk}{N} - \frac{2f_1R}{c} - \frac{2k\Delta fR}{c} - \frac{2(f_1 + k\Delta f)v_{er}t(l)}{c} \tag{3.21}$$

Ignoring the constant phase offset $2f_1R/c$, at the most focused profile where $v_{er} = 0$, matching will occur when:

$$\frac{nk}{N} = \frac{2k\Delta fR}{c} \tag{3.22}$$

We therefore focus on the last term of Equation 3.21 to see what effect it has on the mainlobe for $v_{er} \neq 0$ at the point of matching:

$$H_{phase\_vel}(v_{er}) = \frac{2(f_1 + k\Delta f)v_{er}l(PRI)}{c} \tag{3.23}$$

where $t(l) = l(PRI)$. Then letting $v_{er} = v_{step}$:

$$\begin{aligned} & H_{phase\_vel} = \tfrac{2(f_1+k\Delta f)l(PRI)}{c} \cdot \tfrac{c}{2f_c(PRI)N} \\ \iff \quad & H_{phase\_vel} = \tfrac{(f_1+k\Delta f)l}{f_cN} \end{aligned} \tag{3.24}$$

where $\lambda_c = c/f_c$. Then letting $f_1 = f_c - B/2$:

$$H_{phase\_vel} = \frac{l}{N} - \frac{Bl}{2f_cN} + \frac{Bkl}{f_cN^2} \tag{3.25}$$

Assuming $f_c \gg B$:

$$H_{phase\_vel} \approx \frac{l}{N} \tag{3.26}$$

As was mentioned before, l is a random order of integers from 1 to N and thus l/N is a random order of values from $1/N$ to 1. Therefore at $v_{er} = v_{step}$, $l/N \leq 1$ and this gives a limit to how much the phasors will vary from alignment. Similarly at $v_{er} = v_{step}/2$, $l/N \leq 0.5$ and this reduces the limit by a factor of 2. Therefore when $v_{er} < v_{step}/2$, the limit on l/N is tighter and this brings the phasors closer to alignment which consequently increases the mainlobe amplitude until its peak value at $v_{er} = 0$. On the other hand, when $v_{er} > v_{step}/2$, $l/N > 0.5$ and it is at that point that the peak disperses into the sidelobes. The mainlobe will therefore have a width of v_{step} and this determines the velocity resolution.

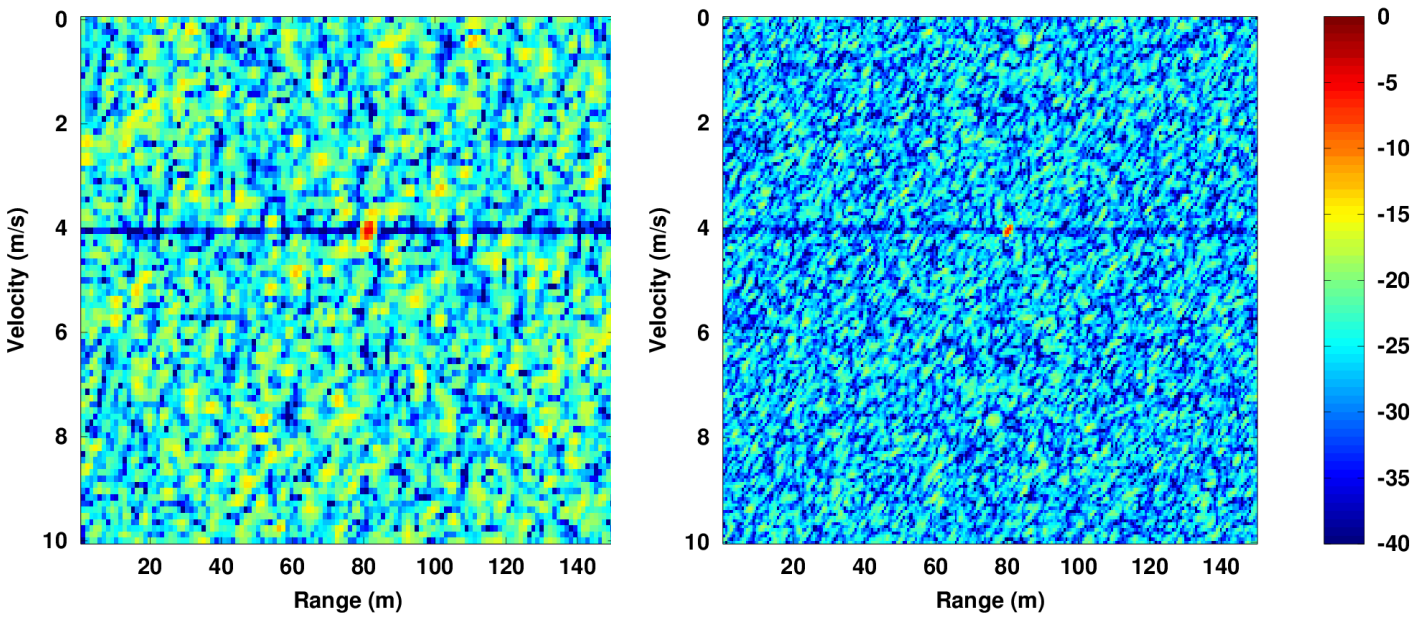

(a) 128 pulses

(b) 256 pulses

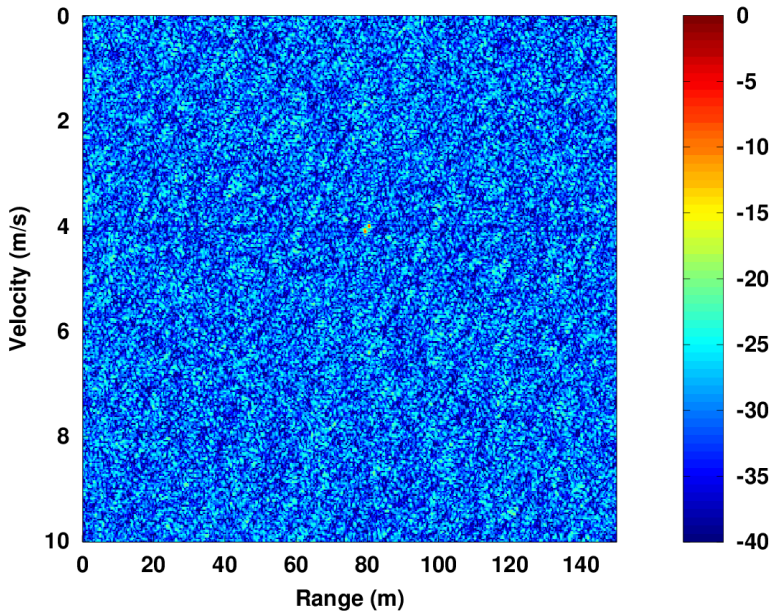

(c) 512 pulses

Figure 3.12: Results showing improved resolution for increased number of pulses for Δf and PRF of 1 MHz and 1 kHz respectively

For a fixed PRF and frequency step size, the range and velocity resolution will be dependent on the number of pulses that are processed. To illustrate this, we assume a target consisting of two scatterers at ranges of 79 and 80 m and velocities of 4.09 and 4 m/s respectively. With the frequency step size and PRF at 1 MHz and 1 kHz respectively, the results are shown in Figure 3.12.

Figure 3.12 shows the improvement in resolution for increased number of pulses and the two scatterers become resolvable at 512 pulses. It can also be seen that the number of pulses has an effect on the sidelobe distribution in the profiles. For more pulses, there are more samples that are processed in the IDFT operation. Due to the randomisation of the phasors, the likelihood of there being coherent addition of all the samples in the IDFT is less and this leads to a lower distribution of sidelobes. An alternate explanation is that since the total energy in the profiles are preserved, more bins would mean more space for that energy to be spread out and therefore a lower distribution of that energy i.e. sidelobes. This means that utilising more pulses will improve the SFDR of the range and velocity measurements.

3.6 The effect of noise

In this work, additive white Gaussian (AWG) noise is used to model the thermal noise that is present in the receiver. The Signal to Noise Ratio (SNR) is the figure of merit used here and the noise present in the receiver determines the input SNR before taking the IDFT for HRR profiling. Because the processing that takes place is complex, the receiver would utilise two channels, I and Q, to process and store complex values. The AWG noise would be present in both channels of the receiver and the input SNR would be the combined SNR of both channels. Therefore the combined noise of both channels would be Rayleigh distributed in amplitude and uniformly distributed from 0 to 2π in phase.

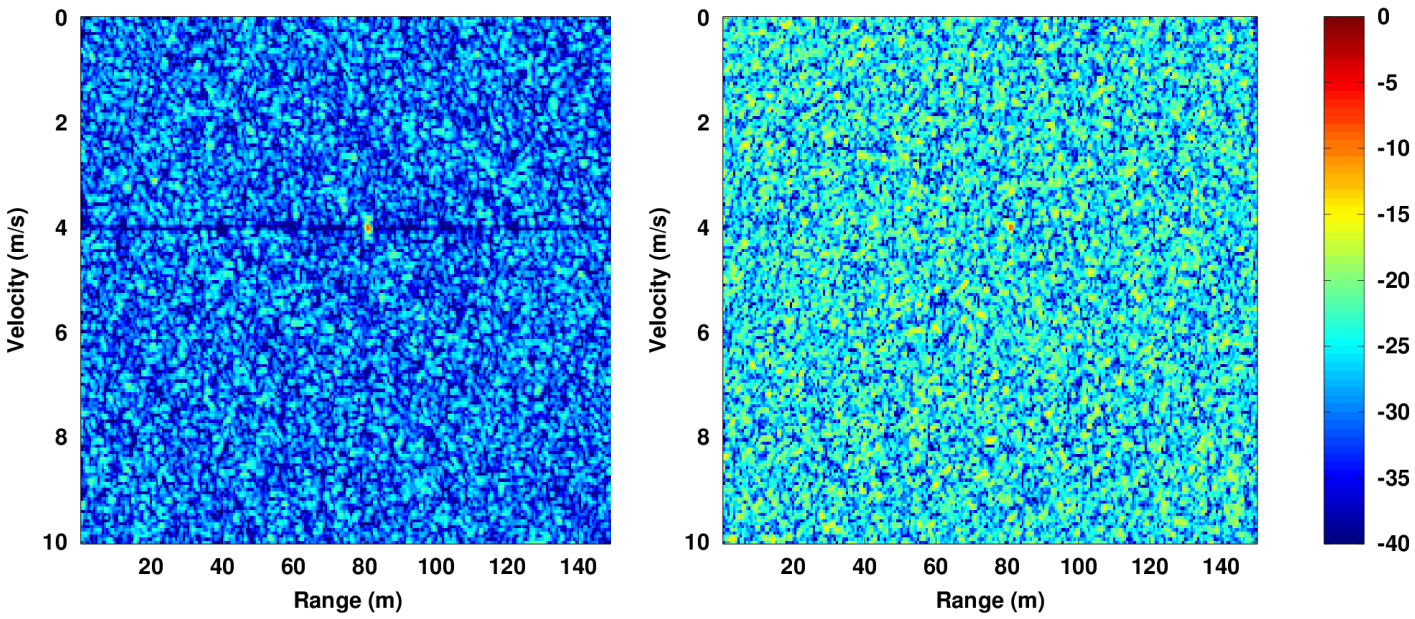

(a) 10 dB

(b) -5 dB

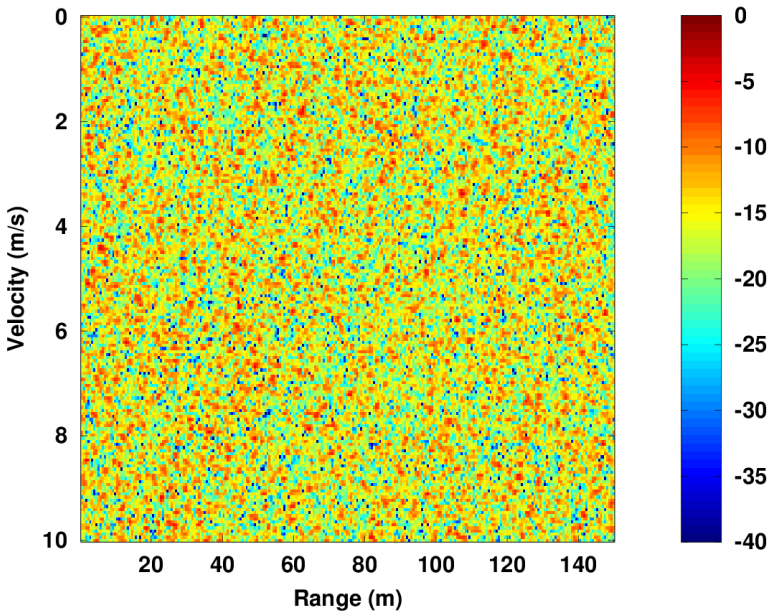

(c) -15 dB

Figure 3.13: Plot of HRR profiles for different input SNR

Figure 3.13 shows the results for different input SNR conditions for a target

signal at 0 dB. It is seen in Figure 3.13(b) that even at -5 dB, where the noise level is higher than the signal, the peak can still be discerned. This is due to the processing gain of the IDFT operation and is determined by the number of pulses N. At -10 dB, the peak is almost submerged into the noise floor as seen in Figure 3.13(c).

For conventional Doppler processing where the FFT is used, the processing gain comes from the fact that the signal energy adds coherently and its power is increased by a factor of N^2 while the noise energy adds non-coherently and its power is increased by a factor of N assuming no windowing was done. This means that the SNR will have a gain of N and more pulses would need to be processed to increase the number of samples for the FFT. This could be done by increasing the PRF to allow more pulses to be processed in a CPI and this would also increase the velocity ambiguity space. But increasing the PRF has the effect of widening the Doppler bin spacing, due to a larger Doppler sampling interval, and this could mean a lower velocity resolution.

For the approach in this work, it was shown in Figure 3.12 that increasing the number of pulses results in a lower distribution of sidelobes in the profiles. Additionally at the point of focusing ($v_{er} = 0$), the IDFT operation coherently sums the signal energy by a factor of N^2. This means that there is a similar processing gain for these methods when increasing the number of pulses. Likewise more number of pulses in a CPI can be processed by increasing the PRF. However Equations 3.11 and 3.19 similarly show that while this would improve velocity ambiguity, it could come at a cost of velocity resolution.

3.7 Conclusion

Hopped frequency waveforms can be used to estimate the range and velocity of scatterers by forming their HRR profiles and using motion compensation. This is due to the thumbtack characteristic of hopped FM ambiguity functions that shows a peak at the correct range and velocity for each scatterer in the set of HRR profile. This provides the potential for imaging and tracking operations while

maintaining frequency diversity and robustness against ECM countermeasures.

The sidelobe behaviour of the HRR profiles has been analysed and phase compensation was shown to only affect the distribution of the energy in the profiles, not the total energy content. Different sequences of hopped frequencies correspond to different distributions of the sidelobes. The transmitted set of frequencies and time, as well as the estimated scatterer range and velocity, can also be used to reproduce the sidelobe distribution for a single scatterer. This will be important when methods are described in Chapter 4 to improve the SFDR of the range and velocity measurements.

Then range and velocity ambiguity was looked at. While the range ambiguity is determined by the frequency step size, a known fact, the velocity ambiguity in this case differs from conventional Doppler processing in that the peaks at the ambiguous velocities show dispersion. This dispersion will be dependent on the ratio between the signal bandwidth and the centre frequency. This is similar to the linear stepped frequency case where Equation 3.2 and Figure 3.2(a) show that the mainlobe ridge undergo some spreading at higher velocity offsets due to the quadratic term in the phase. This dispersion of velocity ambiguous peaks is in fact useful since it lessens their interference when obtaining velocity measurements.

Range and velocity resolution was also looked at. Range resolution is dependent on the signal bandwidth while the velocity resolution that is obtained with the method described here is similar to that of conventional Doppler processing. However unlike standard Doppler processing that operates on a burst by burst basis, this approach allows the range and velocity information to be extracted from a single return by applying motion compensation and locating the focused profile.

Finally noise was incorporated and the peak was still discerned even at sub-SNR conditions due to the processing gain of the IDFT operation. The issue of clutter has not yet been looked at and will be dealt with in Chapter 6.

The disadvantage of this approach is that each scatterer would contribute its own

set of sidelobes to the profiles and this would limit the SFDR of the measurements. More pulses can be utilised to improve the SFDR level but this would mean a higher signal bandwidth and dwell time on target. There are approaches to designing ambiguity functions of hopped frequency waveforms with thumbtack characteristics where, for a given volume under its ambiguity function, sidelobes are pushed out to leave an area of null in the vicinity of the peak so that it doesn't mask nearby smaller scatterers. The disadvantage of this approach, in the context of EW, is that using only a certain sequence of hopped frequency would make it more susceptible to electronic countermeasures.

It would therefore be useful to develop techniques that would be applied onto the HRR profiles itself to improve the SFDR of the measurements without needing to increase the number pulses, and to be applicable for any sequence of hopped frequencies. The techniques for doing so will be discussed and demonstrated in Chapter 4.

Chapter 4

Techniques for Improving Target Measurements

4.1 Introduction

In Chapter 3, it was established that high levels of sidelobes are the main limitation to the range and velocity measurements with regards to the achievable spurious free dynamic range (SFDR). Lowering the distribution of the sidelobes (as well as improving the resolution) can be done by increasing the number of transmitted pulses and this would mean a higher dwell time and bandwidth, but that may not be practical for many radar operations.

This chapter will demontrate additional techniques for sidelobe reduction based on two approaches: One involving apodization and the other based on Högbom's CLEAN technique. These two approaches can be combined to reduce the sidelobe levels significantly. The issues and limitations of these approaches will be outlined as well as a means to address them.

4.2 Sidelobe reduction through apodization

As mentioned in [26], dual apodization is a technique that involves forming a windowed and unwindowed signal from the same return and taking the minimum of the samples between the two. At the cost of increased complexity, the lower sidelobe levels of the windowed signal would be maintained in addition to the narrow mainlobe width of the unwindowed signal. It was also shown in Section 3.4 that different sequences of hopped FM correspond to different sidelobe positions when generating the HRR profiles. Based on the idea of apodization, taking the minimum of the samples between these profiles would result in a combined set of HRR profiles with lower sidelobe levels.

To show this, the simulation parameters from Chapter 3 would be maintained with the exception of the number of frequency steps being 512 i.e a bandwidth of 512 MHz with a step size of 1 MHz. For a single point scatterer, Figure 4.1 shows profiles generated from a single sequence of transmitted frequencies compared to profiles after apodization from 5 and 10 sequences. The velocity of the scatterer was assumed to be at 0 m/s. Figure 4.1 shows an overall reduction of the sidelobes by 10 to 15 dB.

To give an indication of the sidelobe performance, the following figure of merit is proposed:

$$PMSR = \frac{P}{MS} \tag{4.1}$$

where $PMSR$ is the peak to mean sidelobe ratio, P is the highest pixel value in the image of HRR profiles and MS is the mean of the entire image after peak cancellation. The algorithm to detect the peak for cancellation is described in Appendix A. For now the consideration is in seeing how apodization will contribute to the reduction of the sidelobes and therefore the above measure does not take into account multiple scatterers.

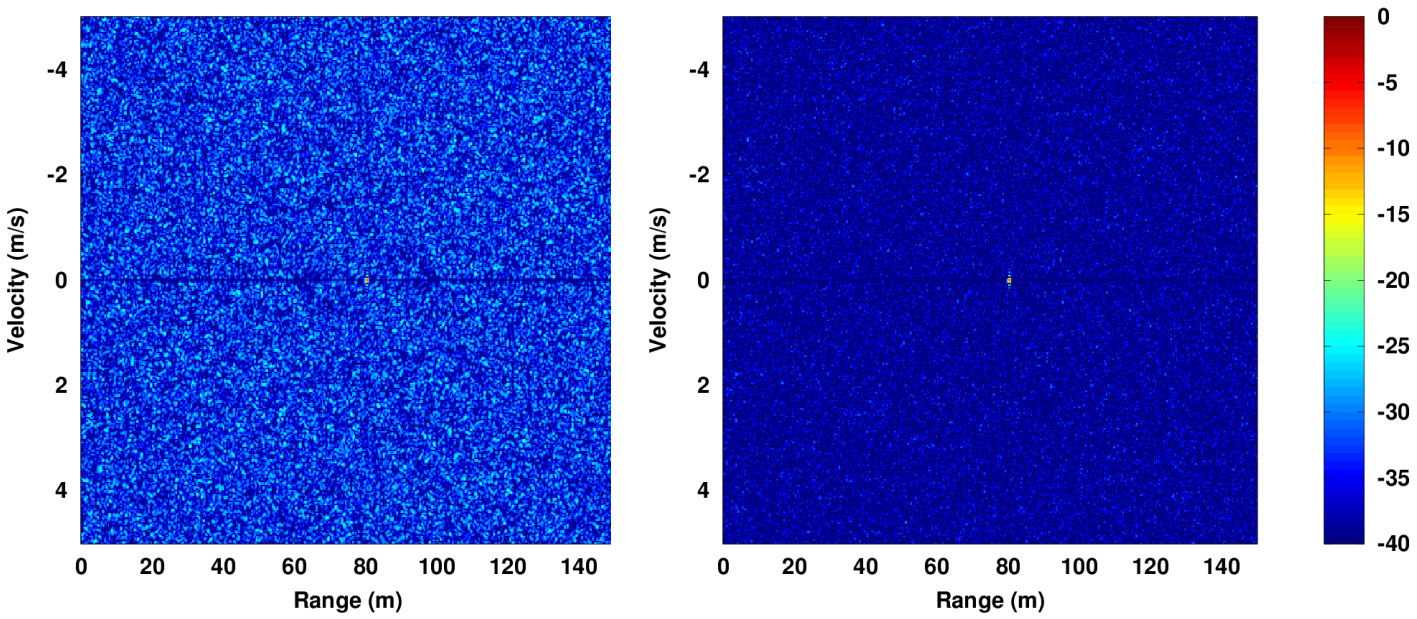

(a) Single sequence

(b) 5 sequences

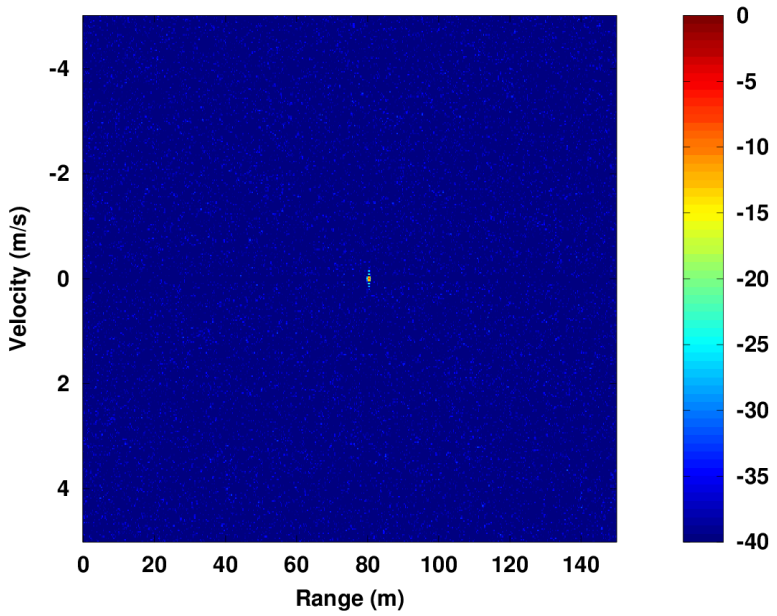

(c) 10 sequences

Figure 4.1: HRR profiles after apodization for different number of transmitted frequency sequences

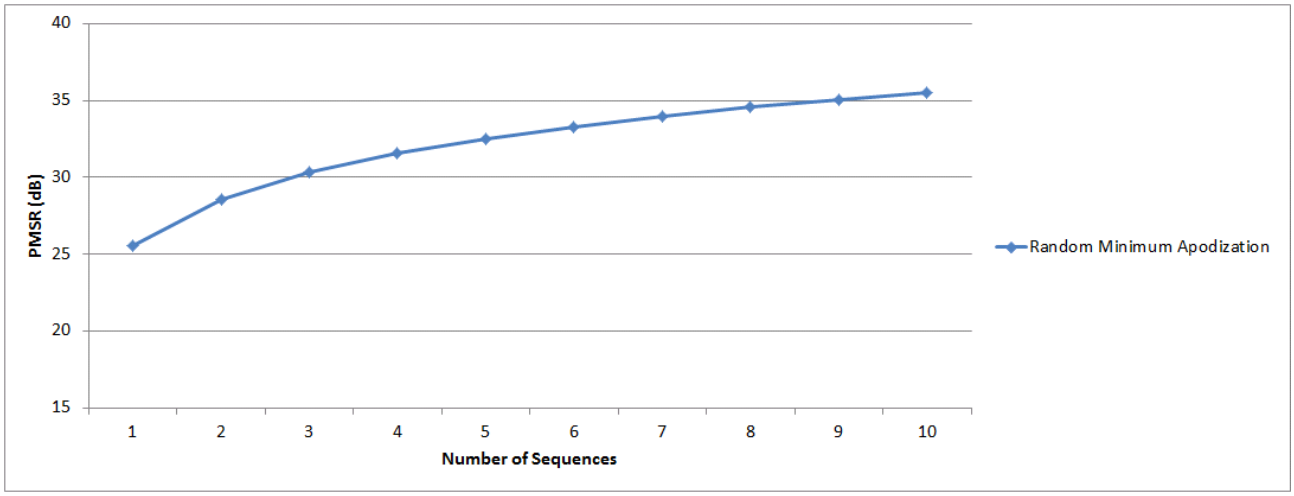

Figure 4.2: Performance evaluation of sidelobe reduction using apodization

Figure 4.2 shows the plot of PMSR with respect to the number of sequences used. It shows that the sidelobe levels continue to reduce as more sequences are added and is applicable if the radar is constrained to a certain bandwidth. It can also be seen as a form of averaging out the sidelobes. The $PMSR$ shows a slowing down of its growth as more sequences are incorporated and therefore it will saturate at some point.

To see how this approach applies to multiple scatterers, Table 4.1 shows the ranges and velocities of eight scatterers that are used in this example.

Scatterer	Range (m)	Velocity (m/s)
1	10	-4
2	30	-3
3	50	-2
4	60	1
5	80	0
6	100	2
7	120	3
8	140	4

Table 4.1: Range and velocity values for scatterers

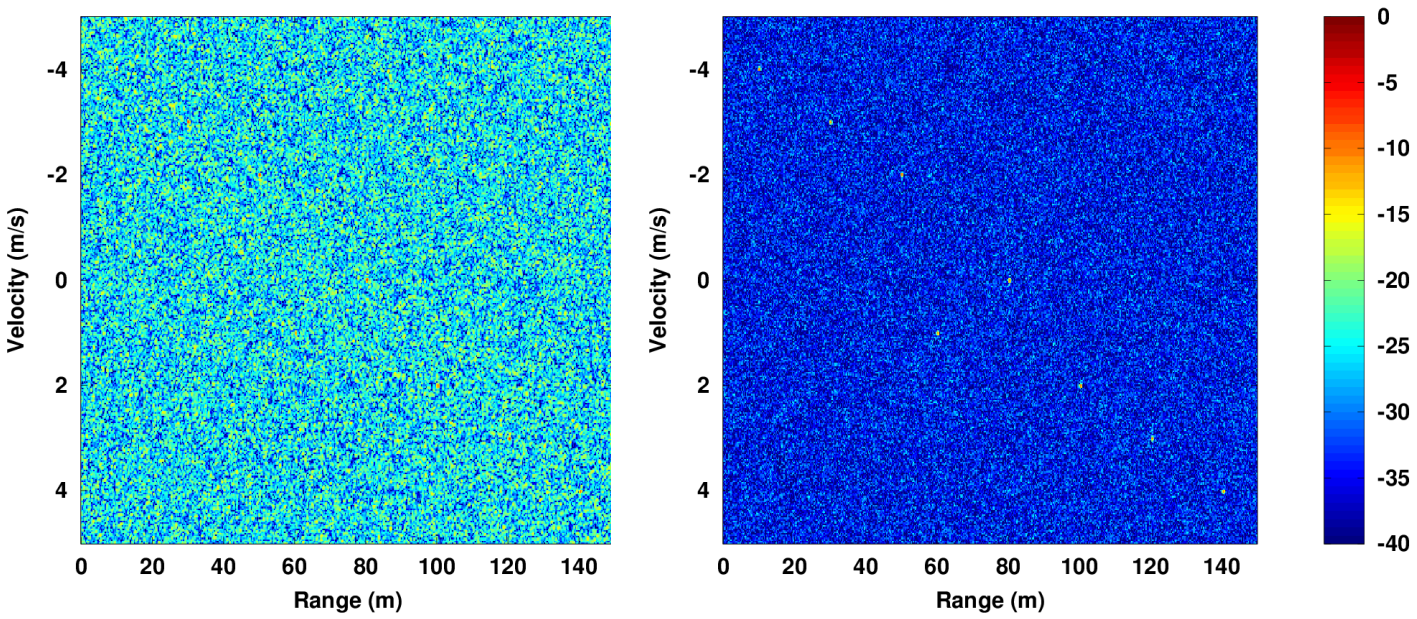

(a) Single sequence

(b) 10 sequences

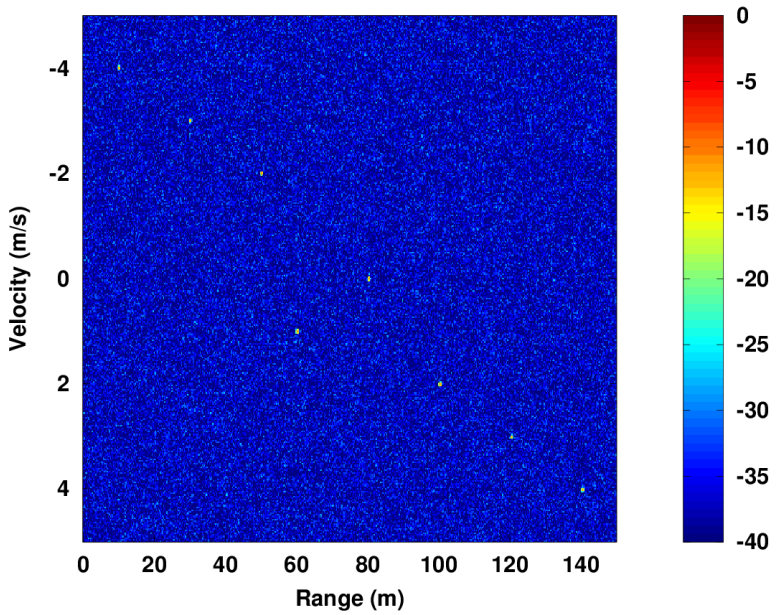

(c) 20 sequences

Figure 4.3: Results after apodization for multiple scatterer target scenario

Figure 4.3 shows profiles for scatterers of equal amplitude and compares it to the profiles after apodization for 10 and 20 sequences. It shows lower sidelobes while the scatterer peaks are still maintained and can be discerned in the plots.

Thereafter scatterer 5 was made 10 dB higher in amplitude than the other scatterers. Figure 4.4 shows that even though the dominant scatterer has a higher contribution of sidelobes, the scatterer peaks are still discernible after 20 sequences. Scatterer 5 was then made 20 dB higher in amplitude above the other scatterers. Figure 4.5 shows that apodization causes the scatterer peaks to disappear when they are masked by the sidelobes of the dominant scatterer. This presents a limitation when using this approach.

With many different random sequences of frequencies being used, there is the benefit of maintaining frequency diversity and hence robustness against ECM. While this approach allows the bandwidth to be constrained to a single burst, it does not address the issue of target dwell time. Though an improvement of sidelobe performance by 10 dB can be achieved by incorporating 10 sequences of hopped frequencies, doing so for 512x10 transmitted pulses would not be practical for many radar scenarios. Another issue is that the peak would have to remain in the same range and velocity bin position as the apodization is being performed. This would pose a problem for targets with high velocities and higher PRFs would be required so that enough profiles are generated before the likelihood of the peak moving out of the bin.

The following section will describe another approach based on the CLEAN technique in which the range and velocity estimates itself will aid the reduction of sidelobes. This technique could help uncover smaller scatterers being masked by the sidelobes of dominant scatterers.

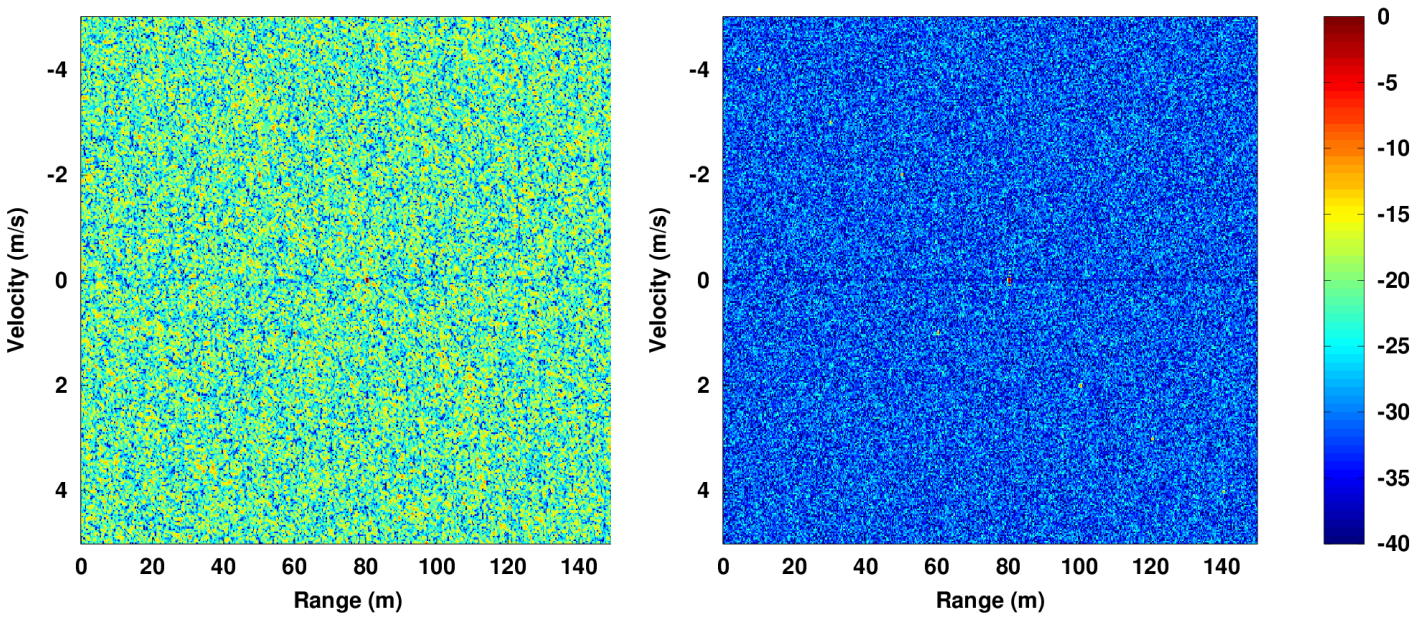

(a) Single sequence

(b) 10 sequences

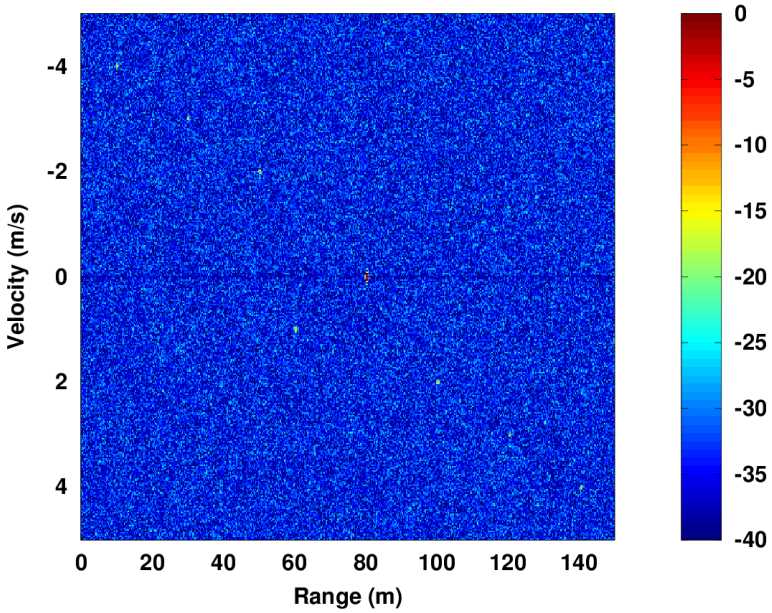

(c) 20 sequences

Figure 4.4: Results after apodization with 10 dB dominant scatterer

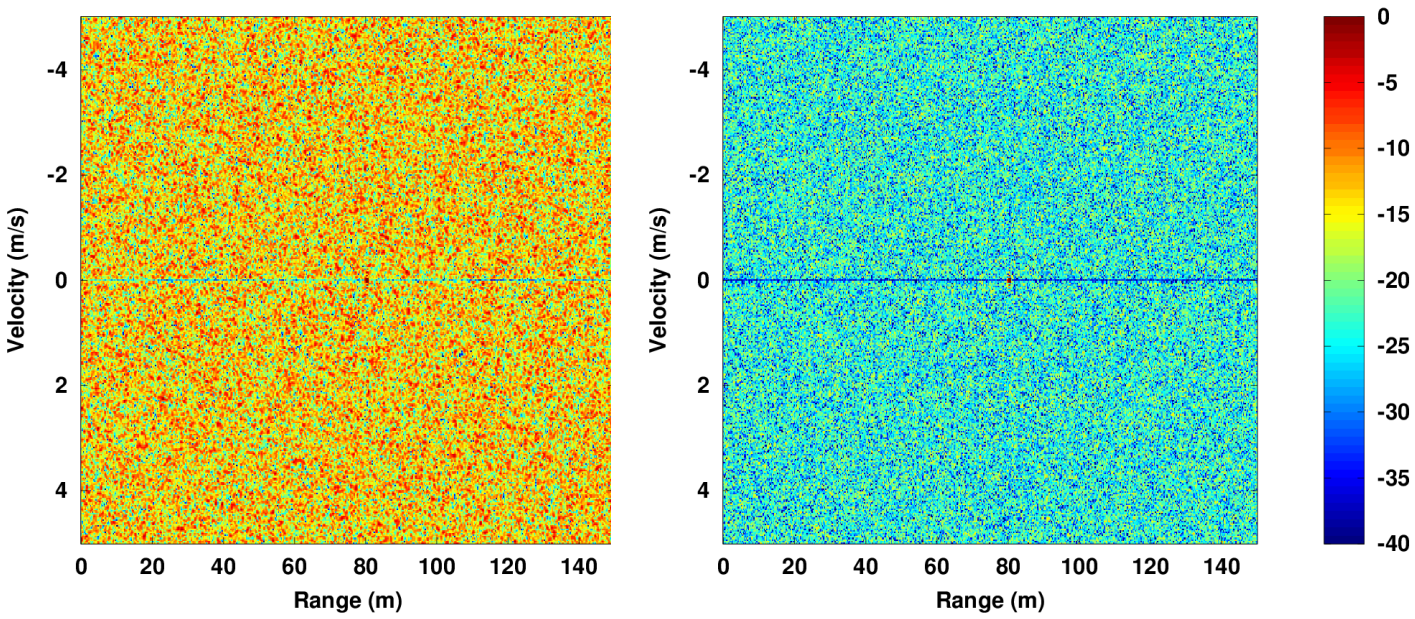

(a) Single sequences

(b) 10 sequences

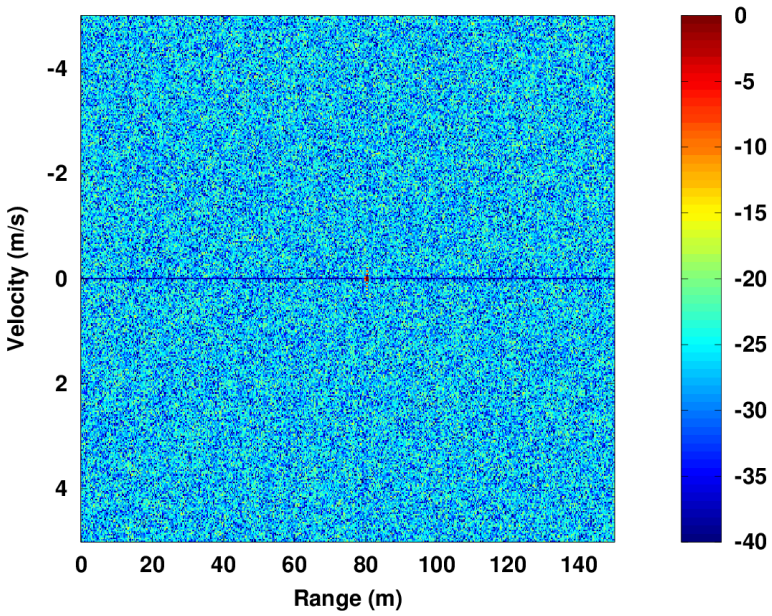

(c) 20 sequences

Figure 4.5: Results after apodization with 20 dB dominant scatterer

4.3 The CLEAN approach

As was mentioned in Section 2.5, the CLEAN technique involves a deconvolution of the energy in an image. It does this by finding the highest pixel, generating its point spread function and subtracting that energy from the image. It then repeats the operation for successive pixels. In Section 3.4, it was shown from Equation 3.7 that reproducing the sidelobes from a single point scatterer requires the transmitted sequence of frequencies and time as well as the scatterer's range, velocity and amplitude. While the frequency and time sequences can be recorded during transmission; the range, velocity and amplitude of the scatterer can be estimated by locating and measuring its associated peak in the profiles. The generated sidelobe response would subtract from the HRR image and would theoretically cancel out the sidelobes that scatterer would contribute to the profiles. To prevent the scatterer's peak from being subtracted, the peak in the reproduced sidelobe response would be removed using the peak detection algorithm described in Appendix A. Care has to be taken when estimating the scatterer's amplitude as the peak value does not necessarily correspond to the actual amplitude of the scatterer due to windowing, scalloping loss, etc. All the results in this simulation were generated using the Blackman window and it was found to reduce the amplitude by around 7 dB. So a scale factor has to be applied to the peak value so that it approximates to the amplitude of the scatterer. In this work, the CLEAN technique was applied non-coherently i.e the absolute values of the pixels were subtracted. Therefore the possibility exists that the sidelobe subtraction would result in negative values and a threshold was applied to make these negative values zero.

Figure 4.6 shows the results of sidelobe reduction using this approach. In this section, a 60 dB dynamic range is used to show that sidelobe reduction to below -60 dB can be achieved. Further sidelobe reduction can be seen when more than one result from the CLEAN algorithm is combined through apodization. For now, perfect range and velocity estimation is assumed and the residual sidelobes shown in Figure 4.6(b) are due to errors in amplitude estimation.

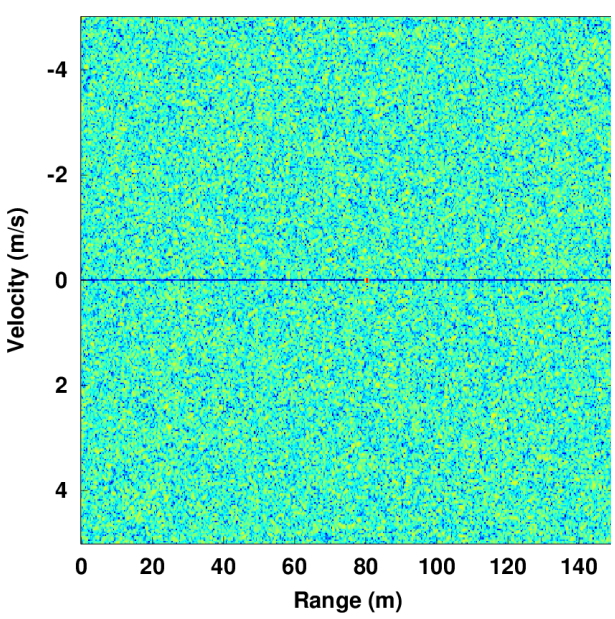

(a) Uncancelled sidelobes

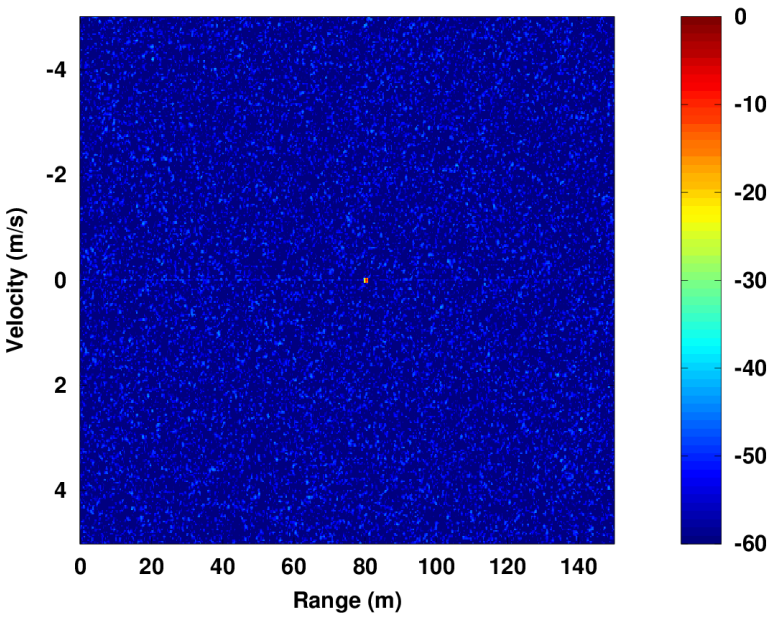

(b) Cancelled sidelobes

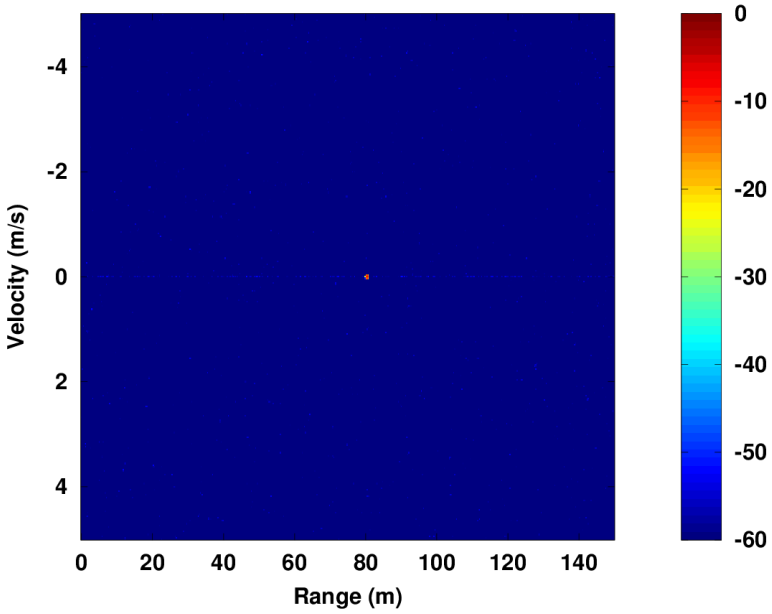

(c) Result after apodization for 5 sequences

Figure 4.6: Comparison of results using the CLEAN approach

To compare this CLEAN approach to the previous approach of only using apodization, the PMSR values were generated relative to the number of sequences and the result is shown in Figure 4.7. This technique shows a significant improvement in performance compared to apodization without the CLEAN technique. Just using a single sequence of frequencies, the sidelobe reduction that can be achieved is greater than using only apodization with 10 sequences.

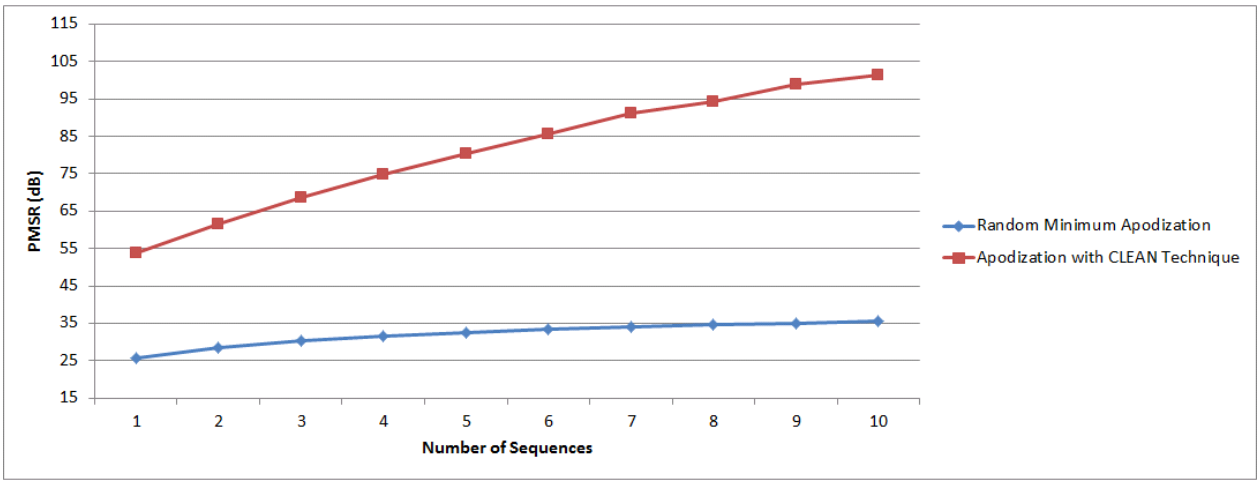

Figure 4.7: Performance comparison between sidelobe reduction techniques

To apply the CLEAN algorithm to a multiple scatterer scenario, the next scatterer would have to be searched once the sidelobes from a particular scatterer has been cancelled. To do so, a temporary copy of the image is formed. Using the peak pixel locations obtained from the peak detection algorithm, the peaks of the previous scatterers are removed leaving the highest peak of the next scatterer to be found. A fuller description of the CLEAN algorithm can be seen in Appendix A. For now, the number of times to search for peaks is hard coded into the algorithm and a terminating condition has not been developed.

To demonstrate this, Figure 4.8 shows the results using the scatterers of Table 4.1. It shows that the scatterer peaks are maintained but against a much lower backdrop of sidelobes compared to Figure 4.3. The residual sidelobes are mainly due to errors in the range, velocity and amplitude estimation of the scatterers.

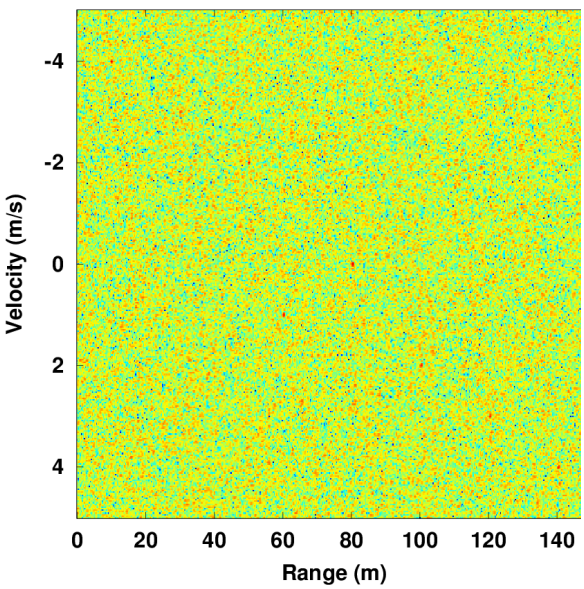

(a) Uncancelled sidelobes

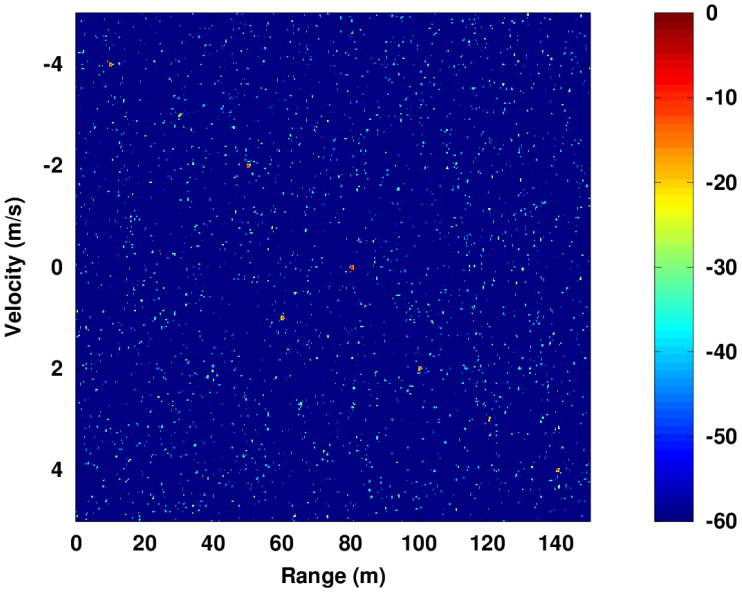

(b) Cancelled sidelobes

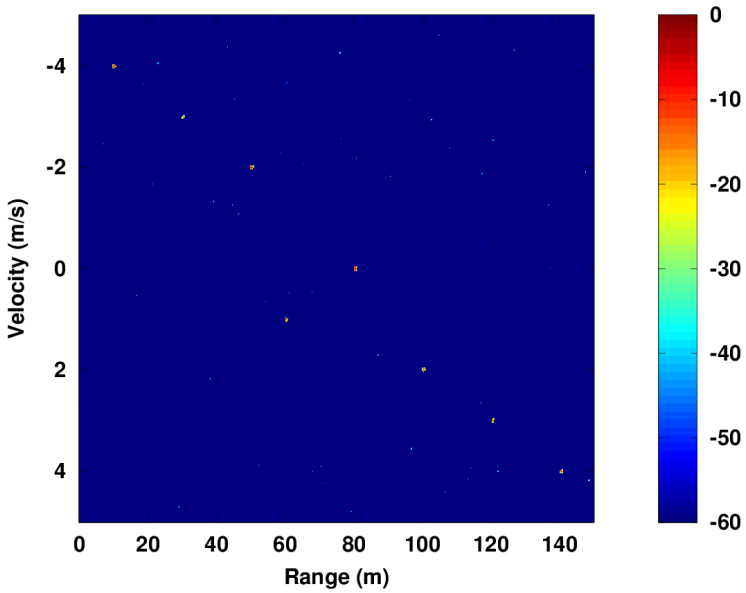

(c) Result after apodization for 2 sequences

Figure 4.8: Comparison of results using the CLEAN approach for the multiple scatterer scenario

4.4 Improving the CLEAN algorithm

Errors in range and velocity estimation of scatterers are one cause of residual sidelobes. This become an issue when a dominant scatterer is present. To see this, the CLEAN algorithm attempts to remove the sidelobes of a 20 dB amplitude scatterer. For purposes of clarification, perfect amplitude estimation was assumed and no noise was added. Figure 4.9 shows undesirably high residual sidelobes for range and velocity errors of 0.1 m and 0.01 m/s respectively. This is further shown in Figure 4.10 where the sidelobe performance was plotted against range and velocity error and in both cases, a loss of 15 dB is seen for range and velocity mismatches of up to 1 m and 0.005 m/s respectively.

Good accuracies in range and velocity estimation is not only useful for this approach of sidelobe cancellation using the CLEAN technique, but is generally useful when trying to obtain target measurements for tracking purposes. The way the measurements are obtained is to use the range and velocity bin position where its peak in the image is located. Here the worst case error in estimation is the range and velocity width (resolution) of those bins. However it is seen that the estimate tolerances are quite narrow and these errors might reduce the performance of the CLEAN algorithm.

One way to improve these range and velocity estimates is to use an optimisation using the sidelobe measure itself as an objective function. This can be seen in the PMSR performance trend and its relationship to the range and velocity error. Because the PMSR requires the use of the peak cancelling algorithm, only the mean of the entire image of HRR profiles after sidelobe cancellation would be sufficient for this process so that the algorithm would be more computationally efficient. Therefore the optimisation becomes a minimisation one.

When looking at the simulation parameters used thus far, a signal bandwidth of 512 MHz would yield a range bin size of 0.29 m. Also the velocity, using the formula in Equation 3.19, is stepped by 0.029 m/s and is therefore the velocity bin size. These would be the worst case errors of these estimates.

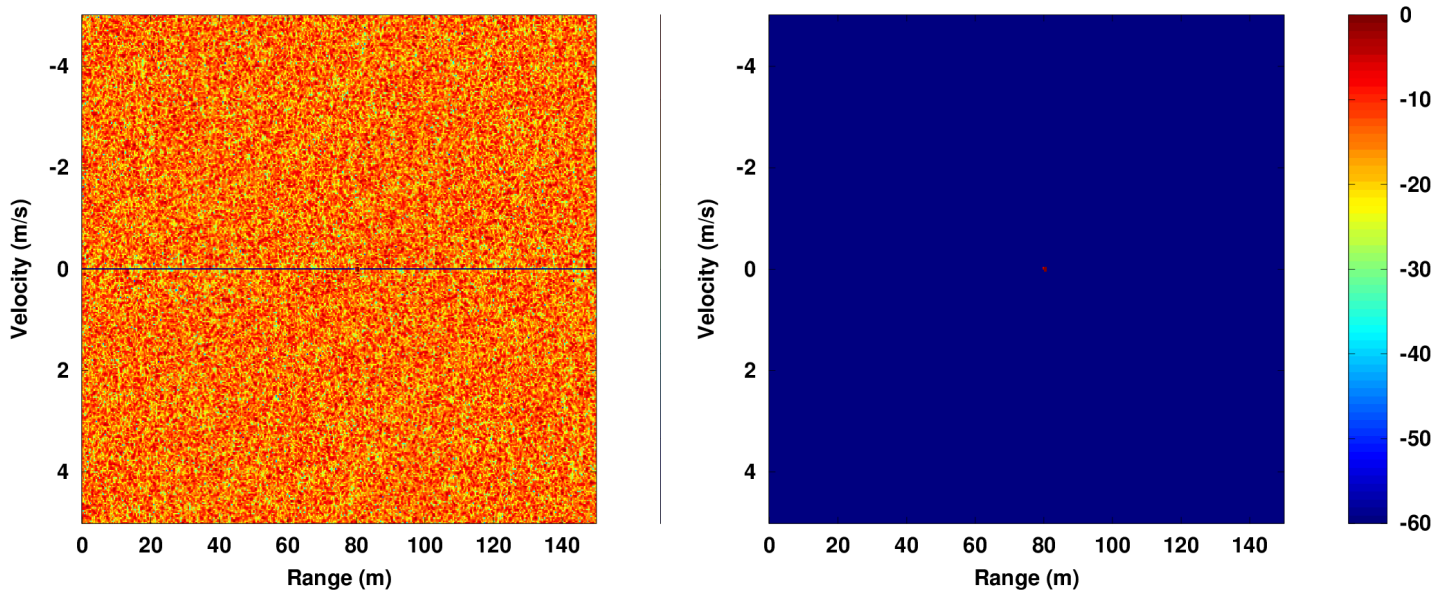

(a) Uncancelled sidelobes

(b) Perfect range and velocity estimation

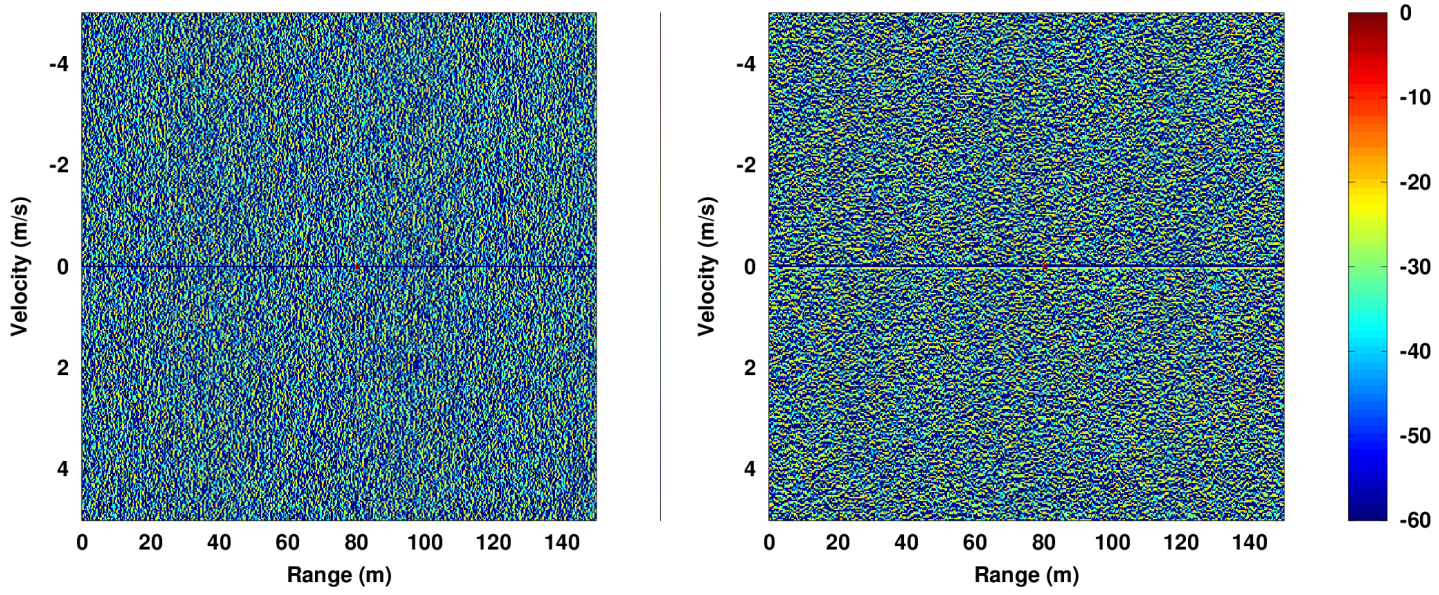

(c) 0.1 m range error

(d) 0.01 m/s velocity error

Figure 4.9: Errors in range and velocity estimation for 20 dB scatterer

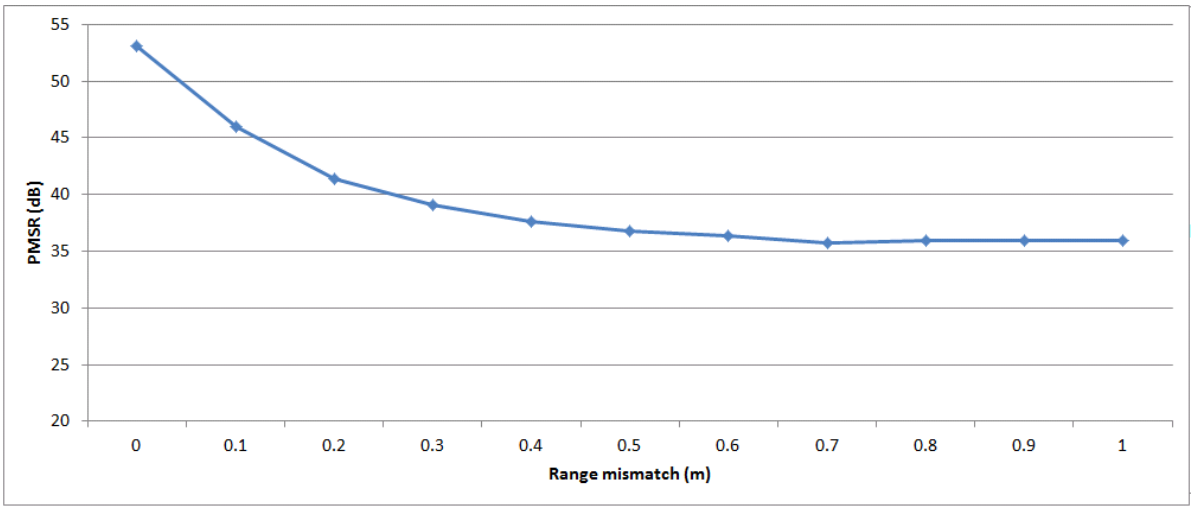

(a) Range error

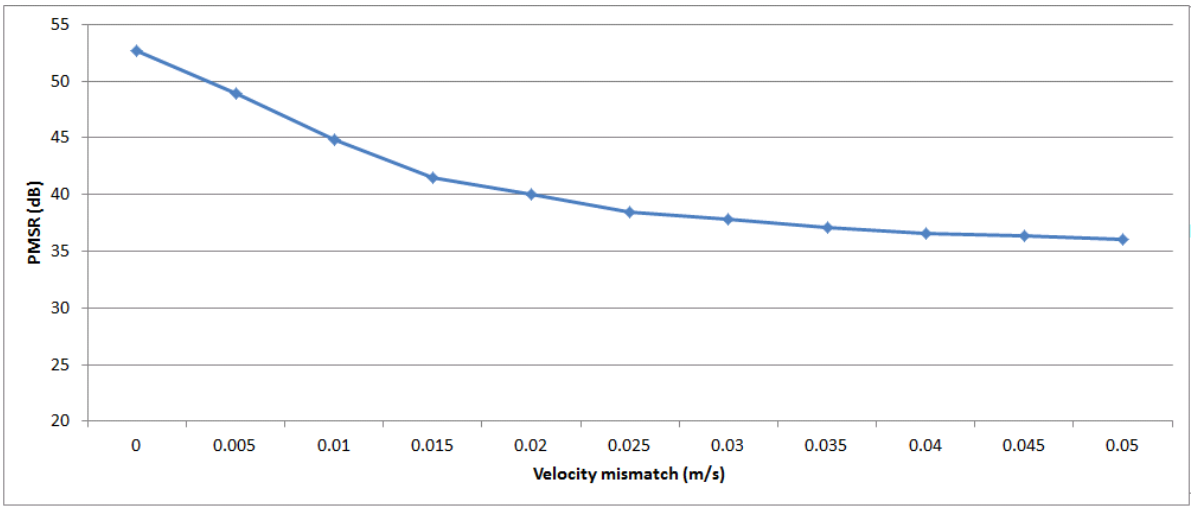

(b) Velocity error

Figure 4.10: Sidelobe performance for estimation errors

This can be seen for a scatterer at 80 m in range and 0 m/s of velocity. While its peak would lie on the velocity bin of 0 m/s, its position in range would be at the bin of 80.218 m. That mismatch in range can result in degraded sidelobe performance.

To give an idea of the nature of the problem, the values of the objective function

i.e. the mean of the image after sidelobe cancellation, were calculated for ranges and velocities situated in two bins around the peak position of 80.218 m and 0 m/s respectively. The range and velocity estimates were incremented in steps of 0.0059 m and 0.00059 m/s respectively i.e a fiftieth of the bin size. Figure 4.11 shows how the objective function varies with a dynamic range of 15 dB and that it converges to a minimum at the true range and velocity values of 80 m and 0 m/s respectively. It can be seen that the optimisation is convex in nature and this simplifies the problem. Within two bins from the peak location, the minima can be assumed to be global. For multiple scatterers contributing to the overall sidelobe levels, the dynamic range of the objective function would differ.

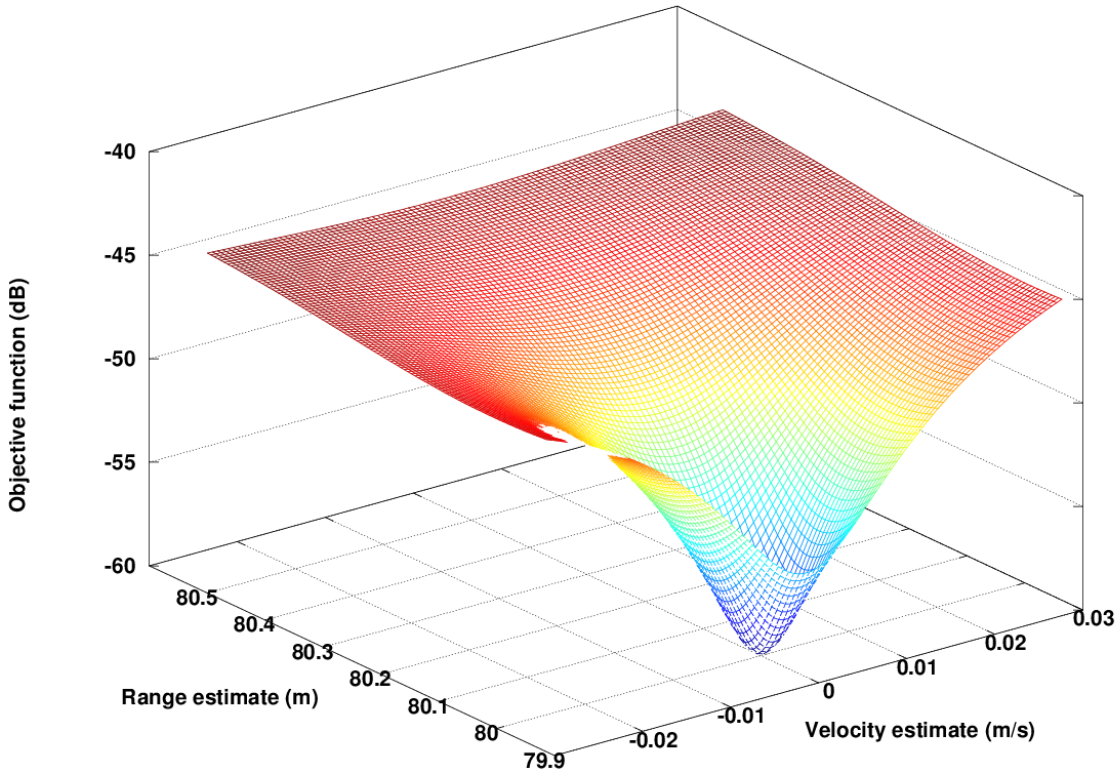

Figure 4.11: Objective function plotted against different range and velocity estimates

One way to improve the range and velocity estimates is to determine which quadrant in the range and velocity search space the minima is to be found, and then to search in that quadrant. The algorithm would operate recursively to narrow the search space until it hones into the peak at the required precision. Looking at Figure 4.12, the algorithm would proceed to calculate the objective function values at points X_1 and X_2 in the range direction of the initial estimate and X_3 and X_4 in the velocity direction. These points would lie one bin from the initial estimate. The quadrant in which the true values lie is determined in the following way: If the objective function value at X_2 is less than X_1, the true values are determined to be the in the positive half of the range domain, and vice versa. The same is assumed for the velocity domain. The algorithm would perform the same operation in the quadrant of interest where the objective function values at points X'_1, X'_2, X'_3 and X'_4 are calculated. The quadrant within that quadrant is determined and the process continues until the search space is narrowed enough. The details of the implementation of this approach is shown in Appendix A. Here the algorithm is made more efficient by not calculating the objective function at the same points more than once.

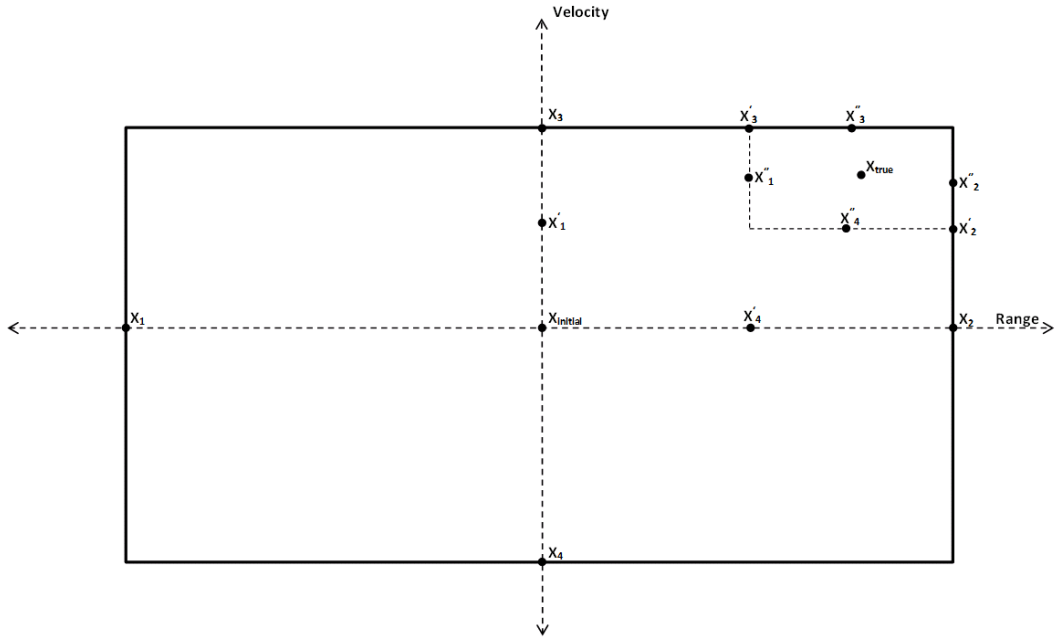

Figure 4.12: Description of searching the true range and velocity values

Going back to the 20 dB scatterer shown in Figure 4.9, Figure 4.13 shows the improve sidelobe performance using the optimised estimates with the residual sidelobes (ideally) completely removed after 5 iterations. Again it should be mentioned that perfect amplitude estimation was assumed in these results and in the actual implementation of this technique, residual sidelobes would be present as well as varying levels of peak amplitude shown in Figure 4.8 due to mismatches in amplitude estimation. But it does show that at the cost of increased computation, this approach of improving the estimates can help to improve the performance of the CLEAN technique to cancel the sidelobes.

4.5 Conclusion

Given that high sidelobe levels are a disadvantage of hopped FM waveforms, a first attempt at reducing those sidelobes is through apodization. Here the profiles are generated from different transmitted sets of hopped frequencies and are combined by finding the minimum output to result in profiles with lower sidelobe levels. This can be seen as a form of averaging to remove the sidelobe energy. The limitations of using this approach is that it does not deal with the issue of dwell time on target and that the peak would have to remain in the range and velocity bin during the operation. One possible means to address this would be involve some control mechanism that would keep the scatterer peak in the bin during the apodization process. The apodization by itself also does not perform well under dominant scatterer conditions where smaller scatterers are masked by larger ones and the peaks of those smaller scatterers have been shown to disappear.

The CLEAN approach was thereafter adopted that would make use of the range, velocity and amplitude estimations to help cancel out the sidelobes. When its results are combined with apodization, significant levels of sidelobe reduction can theoretically be achieved at comparatively low dwell times. It would even help to uncover smaller scatterers that are masked by larger ones.

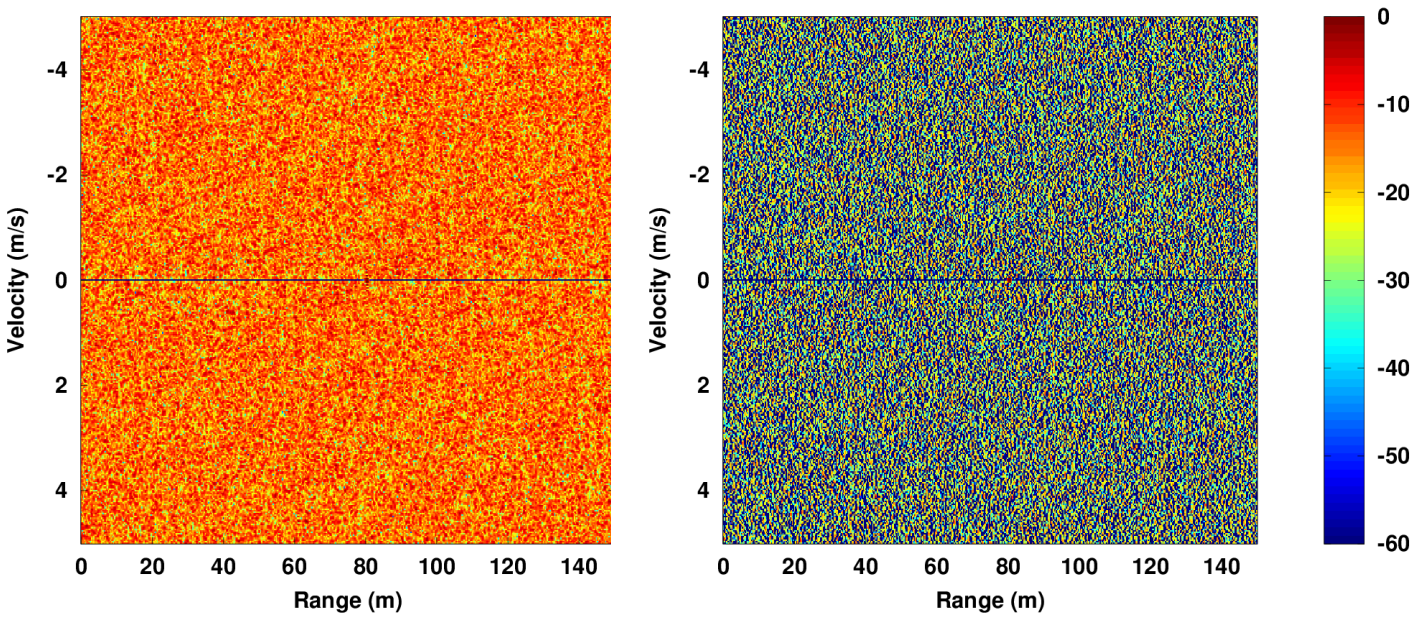

(a) Uncancelled sidelobes

(b) Initial estimate

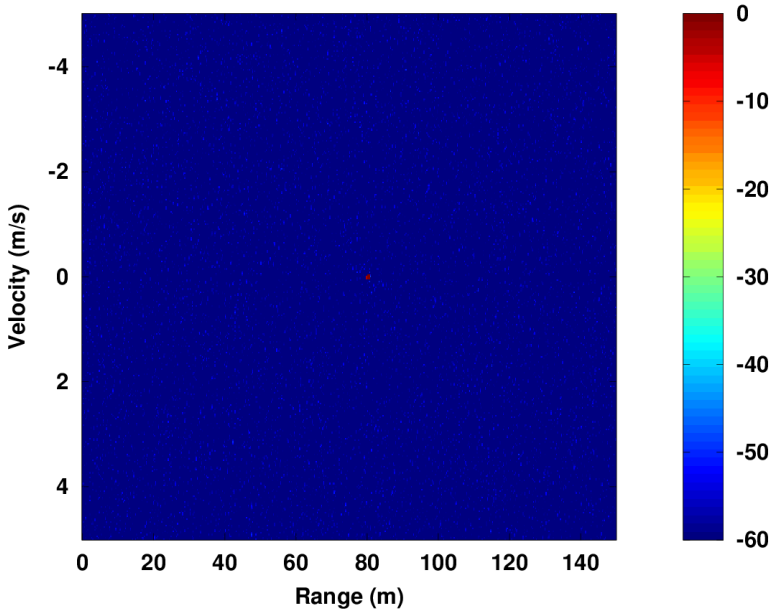

(c) Improved estimate after 5 iterations

Figure 4.13: Sidelobe cancellation of 20 dB scatterer using optimised estimate

However good performance for this technique requires tight accuracies in range, velocity and amplitude estimation due to the presence of residual sidelobes. These sidelobes will severely degrade the process when the algorithm mistakes it for scatterer peaks. The range and velocity estimations can be optimised and this will significantly improve the overall performance of this technique, at a cost of increased computation time.

In the multiple scatterer case, each point scatterer would generate its own sidelobe response and their coherent summation would cause neighbouring scatterers to be affected in terms of amplitude and phase. In this work, the CLEAN technique is applied non-coherently i.e the absolute values of the sidelobe's energy are subtracted. Therefore it would require adequate estimation of the scatterer's range, velocity and amplitude. While the range and velocity can be estimated to good accuracy, the amplitude estimation remains a challenge due to this coherent coupling between the scatterers. This would be even more difficult if the CLEAN technique were to be applied coherently because of the added challenge of trying to estimate the phase of the scatterer. This is the main limiting factor to the performance of the CLEAN approach.

The next chapter will apply the above techniques to simulated rotating scatterers in an attempt to touch on application areas such as ISAR. It will also go on to test these techniques under different dominant scatterer and SNR conditions.

Chapter 5

Simulation of Rotating Scatterers

5.1 Introduction

In this chapter, rotating scatterers are simulated to show how hopped frequency waveforms using the techniques described in Chapters 3 and 4 are used to resolve those scatterers in down range and cross range (velocity). This is to demonstrate the potential these techniques have for applications such as ISAR. These simulations will thereafter be done under dominant scatterer conditions, to see how these techniques will fare when smaller scatterers are masked under the sidelobes of brighter scatterers, and SNR. The performance will be tested in terms of accuracies in range and velocity estimations, since those measurements can be used in tracking applications.

5.2 Generating rotating scatterers

The point scatterers would be randomly distributed from the point of rotation in terms of distance from rotation (ρ) and angle (θ) as shown in Figure 5.1. At each PRI, the angles of the scatterers would change in the following way:

$$\theta_i = \theta_{i-1} + \omega PRI \tag{5.1}$$

where ω is the rotation rate (positive being counter-clockwise) and ρ is assumed constant throughout the rotation as no translational motion is assumed. The point of rotation is assumed to be 80 m in radial range and is within the boresight of the radar.

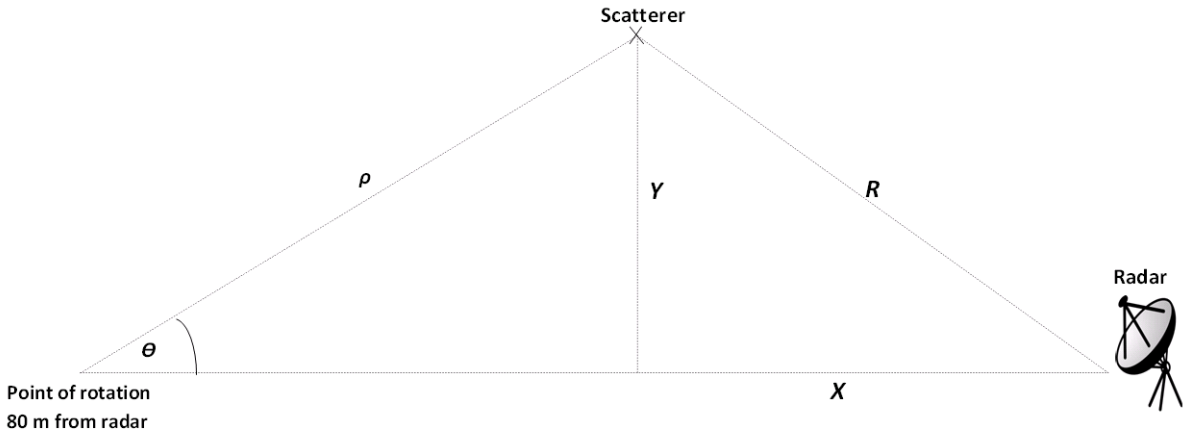

Figure 5.1: Diagram showing scatterer's distance from rotation (ρ), angle (θ), down range X, cross range Y and radial range (R)

At the end of each PRI, the radial range of each scatterer is recorded as shown in Figure 5.1:

$$\begin{aligned} X &= \rho\cos(\theta) + 80 \\ Y &= \rho\sin(\theta) \\ R &= \sqrt{X^2 + Y^2} \end{aligned} \tag{5.2}$$

where X is the down range, Y is the cross range and R is the radial range of the scatterer to the radar. This results in a vector of ranges for each scatterer while the target is rotating.

Looking at Equation 3.1, the term $(R_n + v_n t(m))$ shows a vector of ranges in the signal model. To incorporate the rotating scatterers into the simulation, R from

Eq. 5.2 will be substituted as a vector into the signal model and the process of resolving those scatterers in range and velocity (cross-range) will be done using the methods described in Chapters 3 and 4. In this way, an ISAR image of the rotating scatterers can be formed.

To demonstrate this, Figure 5.2(a) shows 5 randomly distributed scatterers. To generate the profiles, the maintained simulation parameters are 1 kHz PRF, 5 GHz centre frequency, and 512 transmitted pulses in the burst, each with a step size of 1 MHz thereby resulting in a total bandwidth of 512 MHz. The scatterers are rotating at 3° per second counterclockwise. Figure 5.2(b) shows the profiles of the 5 scatterers and that their peak locations correspond to their locations in Figure 5.2(a) but against the backdrop of high sidelobes.

Figure 5.2(c) plots the profiles after applying the CLEAN technique and the scatterer peaks are shown more clearly compared to Figure 5.2(b). Figure 5.2(d) plots the profiles when two sets of results from the CLEAN algorithm is combined through apodization and this results in a further reduction of sidelobes. Here the cross range scaling was done as follows [31]:

$$\begin{aligned} & CrossRange &&= \lambda_c/2\Delta\theta \\ \Longleftrightarrow\ & CrossRange &&= \lambda_c/2\omega(PRI)N \\ \Longleftrightarrow\ & CrossRange &&= v_{step}/\omega \end{aligned} \tag{5.3}$$

using the velocity resolution $v_{step} = \lambda_c/2(PRI)N$ from Equation 3.19. In practice, the challenge is to estimate the rotation rate ω which is non-trivial when the target is non-cooperative and is rotating non-uniformly. As was mentioned in Chapter 4, the scatterer peaks from two (or more) sets of results may not be aligned during the apodization process and this would cause part of the scatterers' mainlobe to be cancelled. This would be the case when the scatterers are rotating and could be mitigated by using a higher PRF for the same number of transmitted pulses in the burst i.e. lower dwell time on target, so that the likelihood of the peaks moving out of alignment would be lessened. However using a higher PRF would incur a loss in velocity resolution.

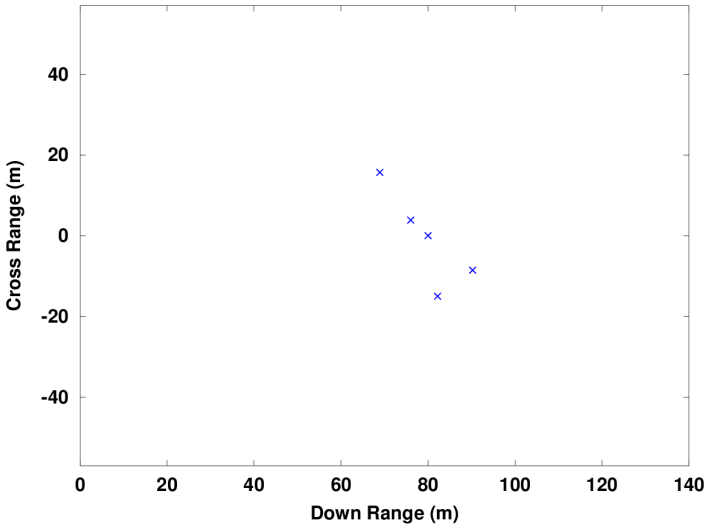

(a) 5 randomly distributed scatterers

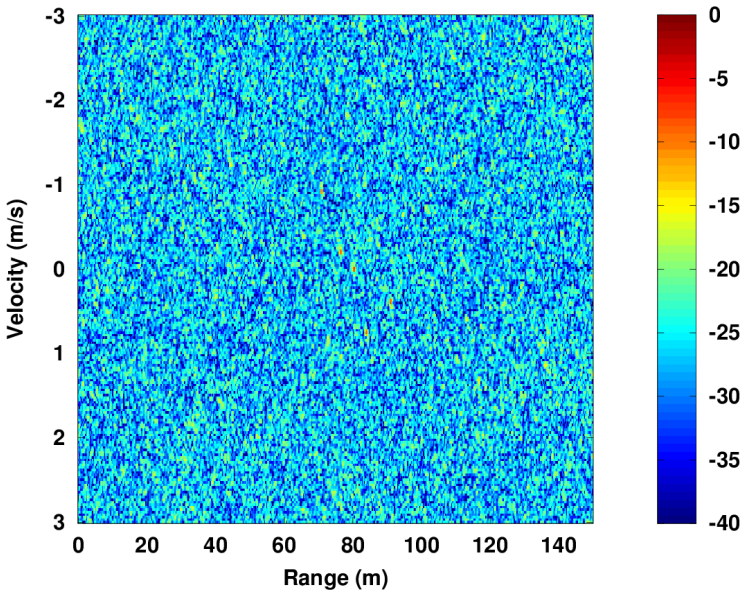

(b) Profiles of rotating scatterers

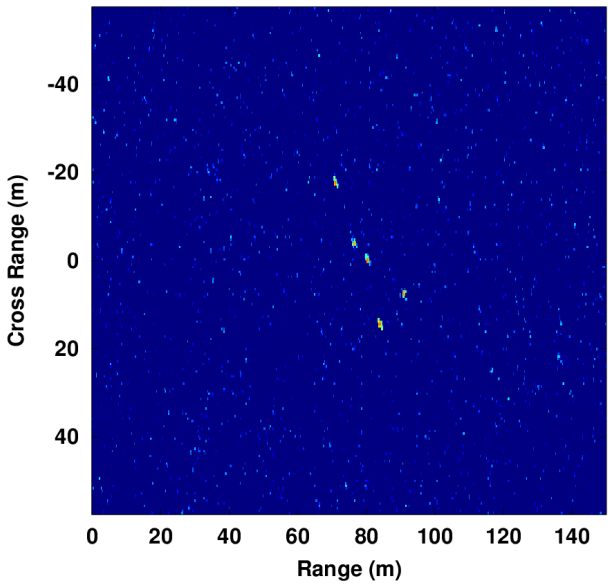

(c) Profiles after CLEAN technique

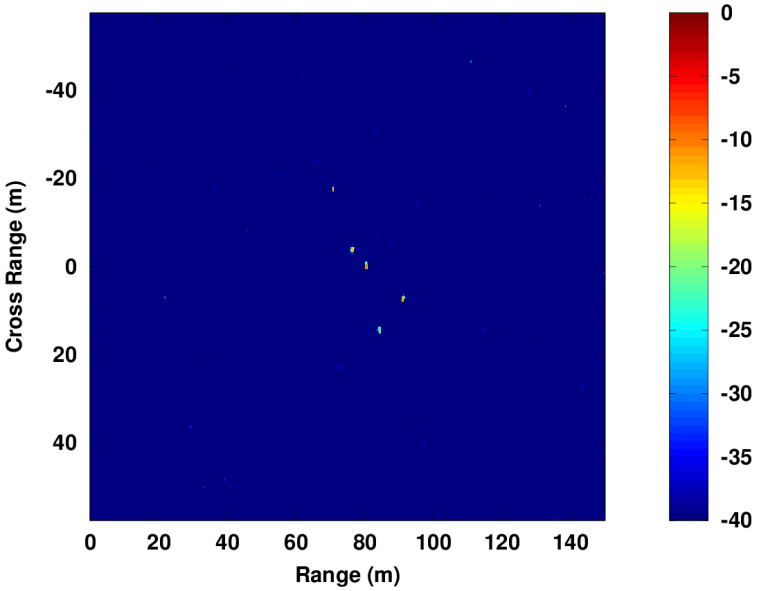

(d) Profiles after apodization with two sets of CLEAN results

Figure 5.2: Plots showing simulation of rotating scatterers and results

5.3 Evaluation under dominant scatterer conditions

One reason for adopting the CLEAN technique is to help uncover scatterers that are masked by the sidelobes of stronger scatterers. In this section, the CLEAN technique as applied onto the rotating scatterers will be evaluated under different dominant scatterer conditions. In this scenario, the amplitude of the dominant scatterer will be stepped from 0 to 30 dB while the rest of the scatterers will have a constant amplitude of 0 dB. In Section 4.4, a method to improve the range and velocity estimates of the CLEAN algorithm has been described and in this section, its performance will be compared to the CLEAN technique using only the initial estimates.

For each dominant scatterer case, 100 monte carlo runs were performed. Each run was done using a different random placement of scatterers and a different sequence of transmitted frequencies. A constant rotation speed of 5° per second was assumed. In each run, the range and velocity estimates of all 5 generated scatterers were compared against their true values and their errors have been recorded. Because each run had a different placement of scatterers, the true range and velocity scatterer values, using the vector of ranges R from Eq 5.2, were calculated as follows:

$$\begin{aligned} R_{true} &= R(0) \\ V_{true} &= mean(diff(R)) * PRI \end{aligned} \tag{5.4}$$

where $R(0)$ is the first value in R and $diff(R)$ is a vector of differences of the values in R. With the scatterers rotating at 5° and with 512 pulses being transmitted at 1 kHz PRF, this results in a total rotation of 2.56° in the burst which is within the small angle approximation for rotating scatterers. The approximation of Equation 5.4 is therefore valid because the scatterer's radial velocity can be assumed to be constant. Accuracies in the range and velocity measurements of radar targets is of interest since these measurements can be used as inputs to tracking algorithms.

Figure 5.3 shows a plot of results for this performance evaluation run. For each dominant scatterer amplitude, the average of the estimation error of all 5 scatterers for all 100 monte carlo runs were calculated and plotted. It shows that overall the range and velocity estimates from the improved CLEAN algorithm give a lower trend of estimation error compared to using the CLEAN algorithm without the optimisation, especially at the higher dominant amplitudes. It also shows that the errors tend towards convergence beyond 25 dB. The errors in velocity are less due to its bin size being smaller but it still shows a similar trend to the range estimates. Up to around 8 to 10 dB, the performance between the two trends, in terms of average estimation error, are roughly similar with no indication that the improved estimates give an improvement over the initial estimates. It could be that in the calculation of the average of these estimations, some of the errors could have been significant enough to affect these averages i.e. large outliers in errors. This would be the case if energy from high amplitude sidelobes are mistaken as scatterer peaks or if two scatterers are spaced so closely together that the CLEAN algorithm considers them as one scatterer and this results in it mistaking sidelobe energy for the next scatterer to be searched.

It would be useful to corroborate the results in Figure 5.3 by plotting the median of the errors. This is done in Figure 5.4 where the improved estimates show a consistently lower trend in estimation error compared to the initial estimates up to around 27 dB towards the point of convergence. This can also be seen in Figure 5.5 which plots the average number of correct estimations. An estimation is regarded as 'correct' when its error (in magnitude) is less than half the range or velocity bin size (0.146 m and 0.0146 m/s respectively). In other words, these are estimations that lie in the same bin as their true values. Figure 5.5 shows that throughout the evaluation, the improved estimates yielded more correct estimations compared to using only the initial estimates.

When looking at the trend of average estimation error in Figure 5.3, the initial estimates start to decline at around 8 dB for range and velocity whereas the improved estimates start to decline at around 12 dB for range and velocity.

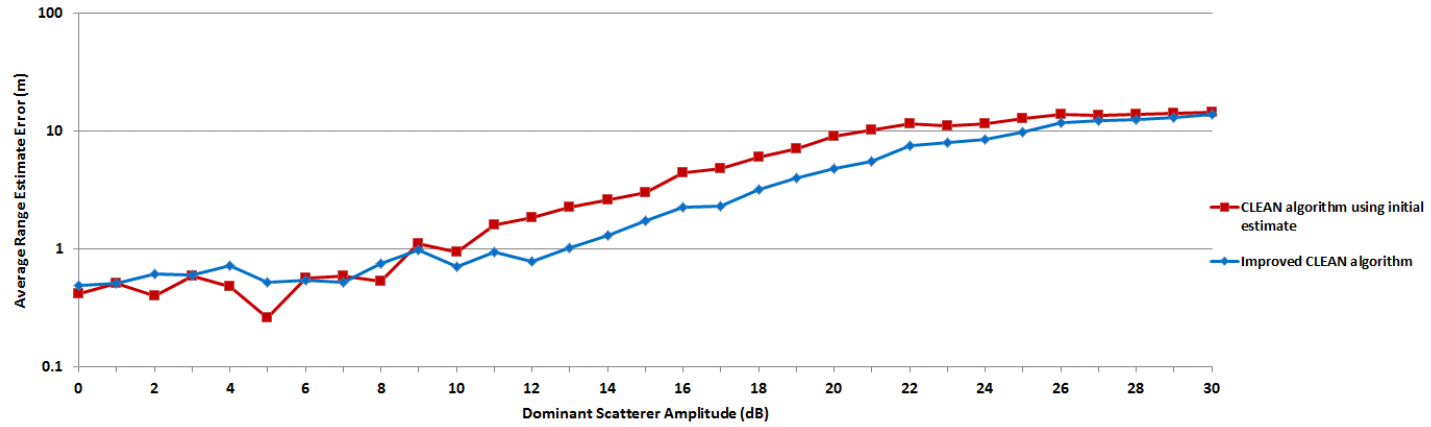

(a) Range estimates

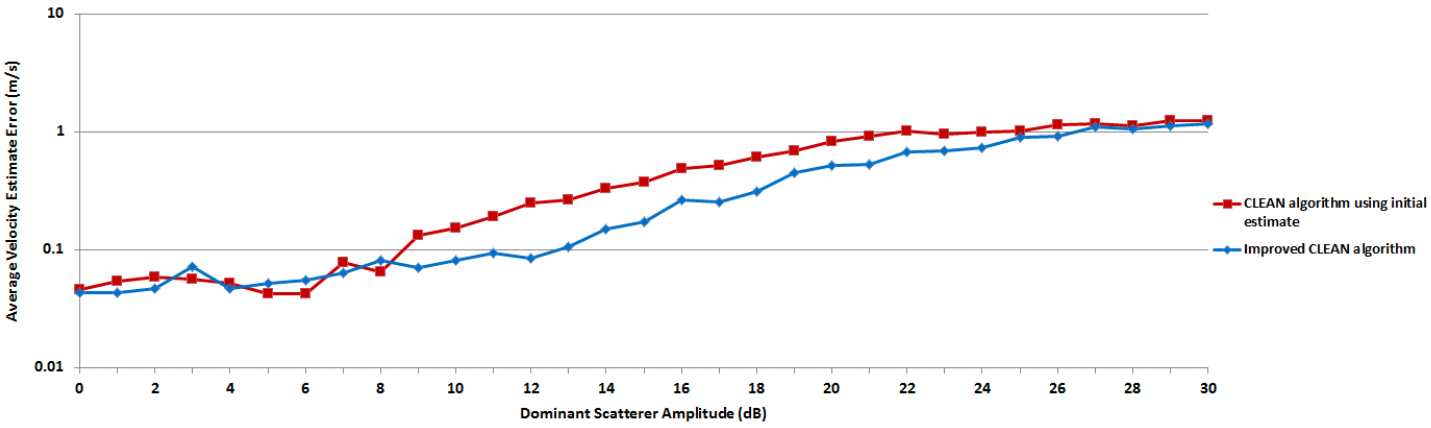

(b) Velocity estimates

Figure 5.3: Average estimation error for different dominant scatterer conditions

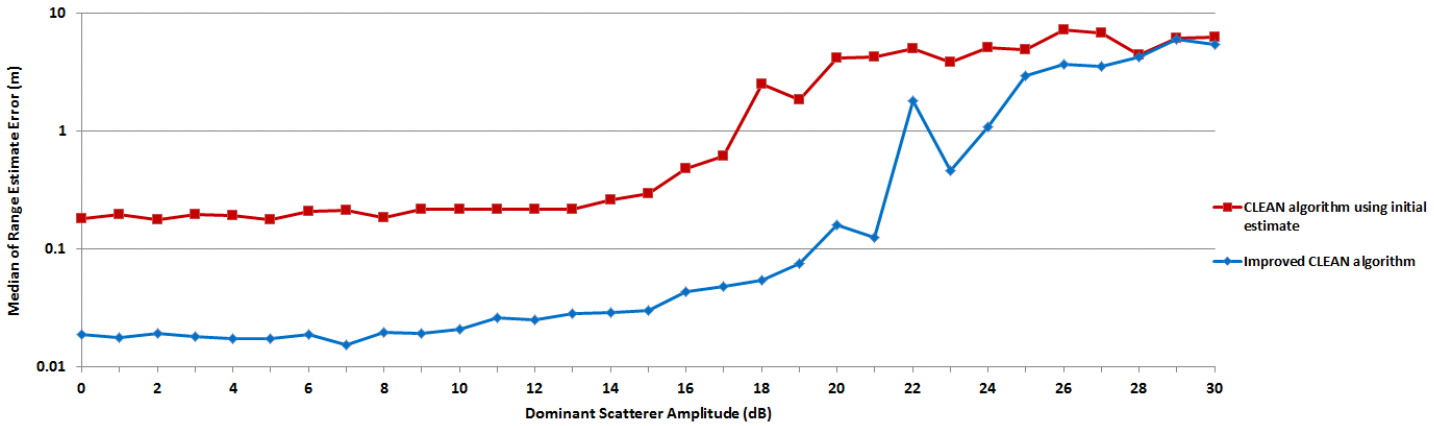

(a) Range estimates

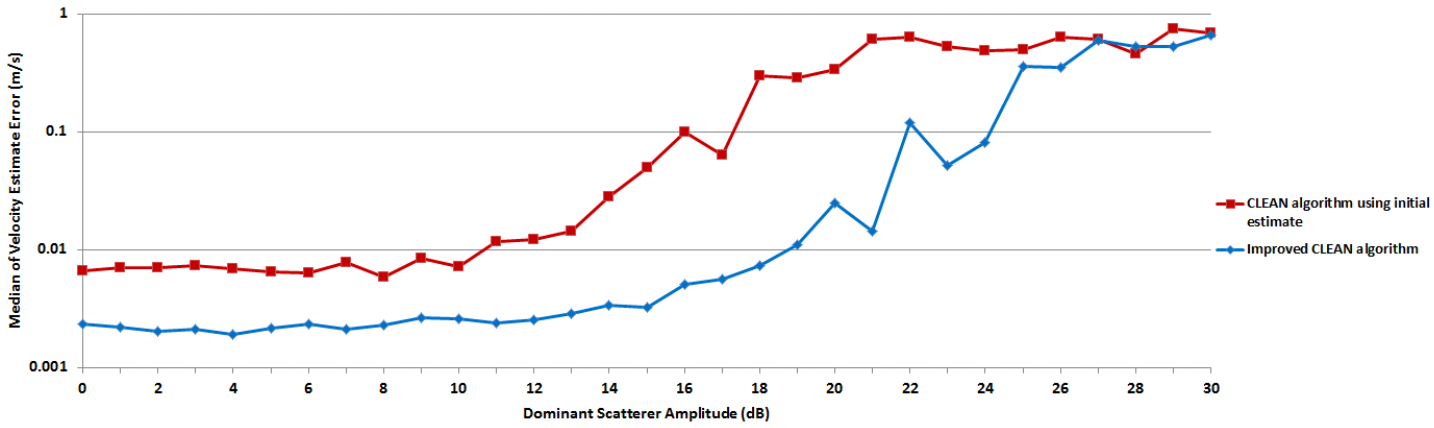

(b) Velocity estimates

Figure 5.4: Median of estimation errors for different dominant scatterer conditions

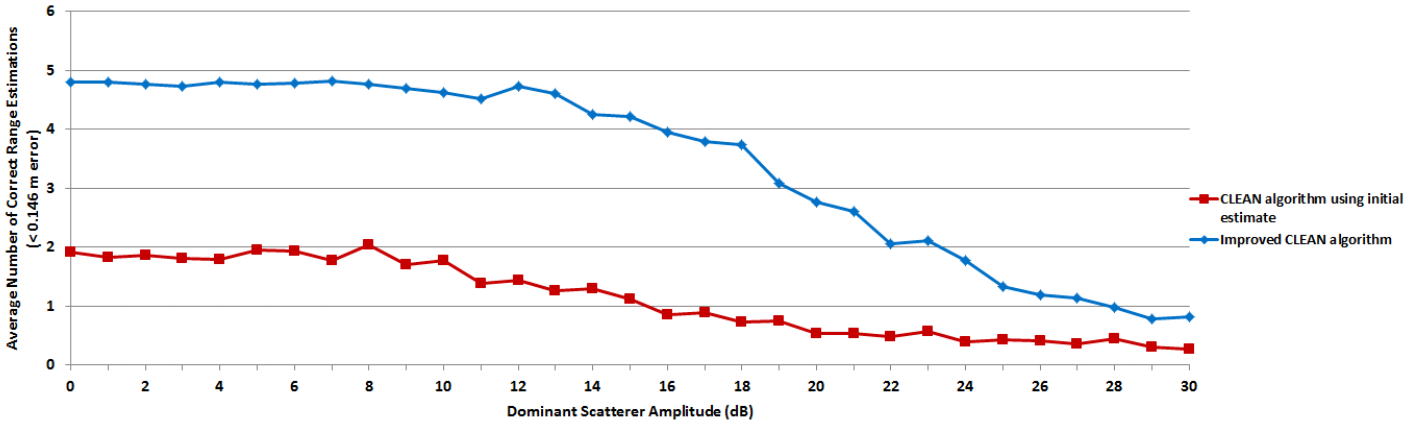

(a) Range estimates

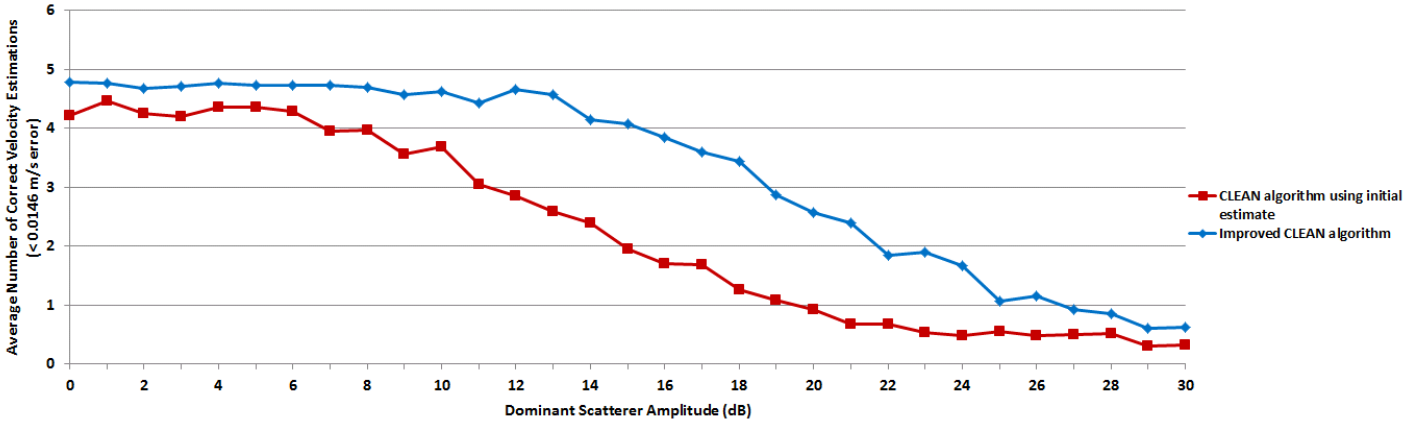

(b) Velocity estimates

Figure 5.5: Average number of correct estimations for different dominant scatterer conditions

In terms of median estimation error (Figure 5.4), the initial estimates decline at 12 dB for range and 10 dB for velocity whereas the improved estimates decline at 15 dB for range and velocity. Finally with regards to the number of correct estimations (Figure 5.5), the initial estimates start to decline at 8 dB for range and 6 dB for velocity whereas the improved estimates start to decline at around 11 dB for range and 13 dB for velocity. This demonstrates that the improved CLEAN algorithm show a lower trend of estimation error compared to the CLEAN algorithm using only initial estimates. The performance of the improved CLEAN algorithm also begin to decline at higher dominant scatterer conditions. Looking at the above results overall, keeping in mind that the aim is to see how well smaller scatterers can be uncovered from the sidelobes of stronger scatterers, the CLEAN technique using the optimisation process described in Chapter 4 can perform adequately with dominant scatterers up to around 13 dB and a gradual decay in performance is seen thereafter to the point of saturation beyond 28 dB.

5.4 Evaluation under SNR conditions

SNR is an important metric of performance for many radar operations. This is especially the case in EW environments where jammers flood the radar receivers with high levels of noise. It will therefore be useful to see how the techniques developed in this work and applied to the simulated rotating scatterers will fare in these different noise conditions. In this evaluation, the scatterers will have a constant amplitude of 0 dB while the input SNR will be stepped from 20 dB to -20 dB. Section 3.6 discussed the incorporation of noise into the simulations and this is the noise that will add into the signal before the HRR profiles are formed by the IFFT. The setup will be the same as was done for the dominant scatterer simulation with 100 monte carlo runs being used. The evaluation will involve recording the errors in range and velocity estimation for 5 scatterers. Accuracies in estimation is of special interest here due to many tracking operations being done in low SNR conditions, especially in jamming environments.

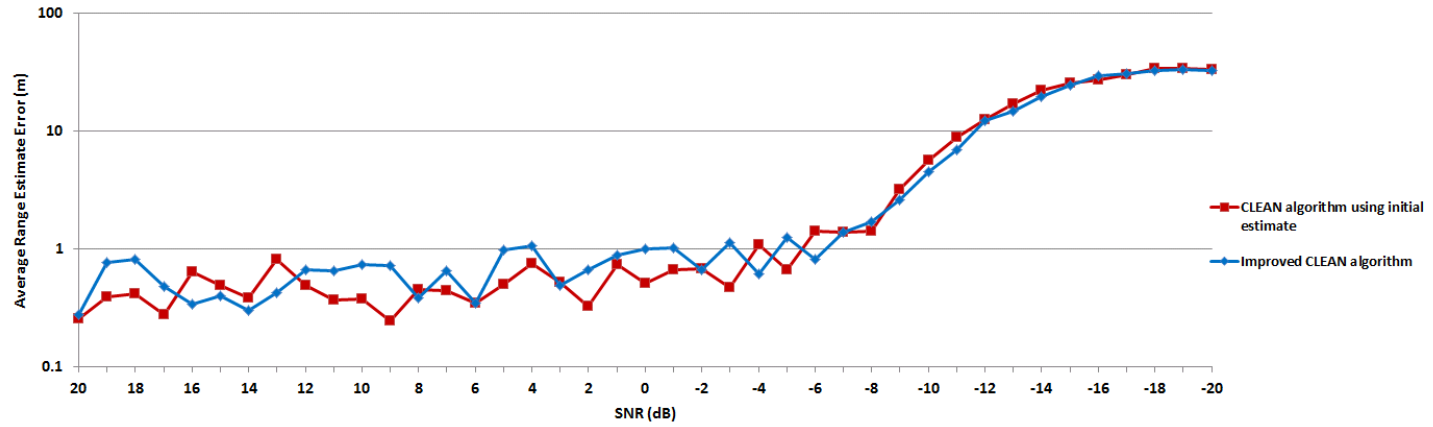

(a) Range estimates

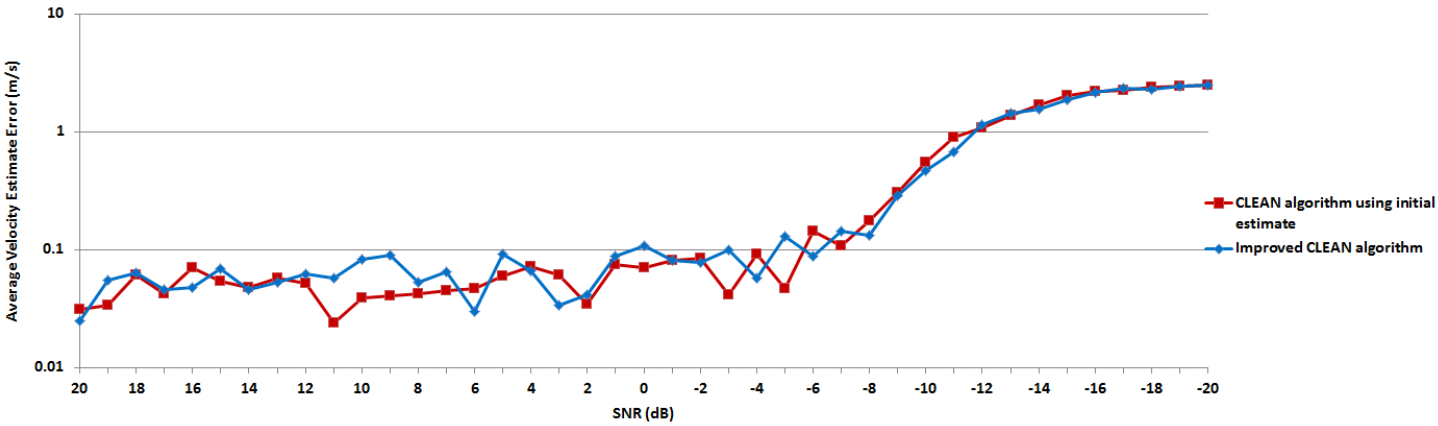

(b) Velocity estimates

Figure 5.6: Average estimation error for different SNR conditions

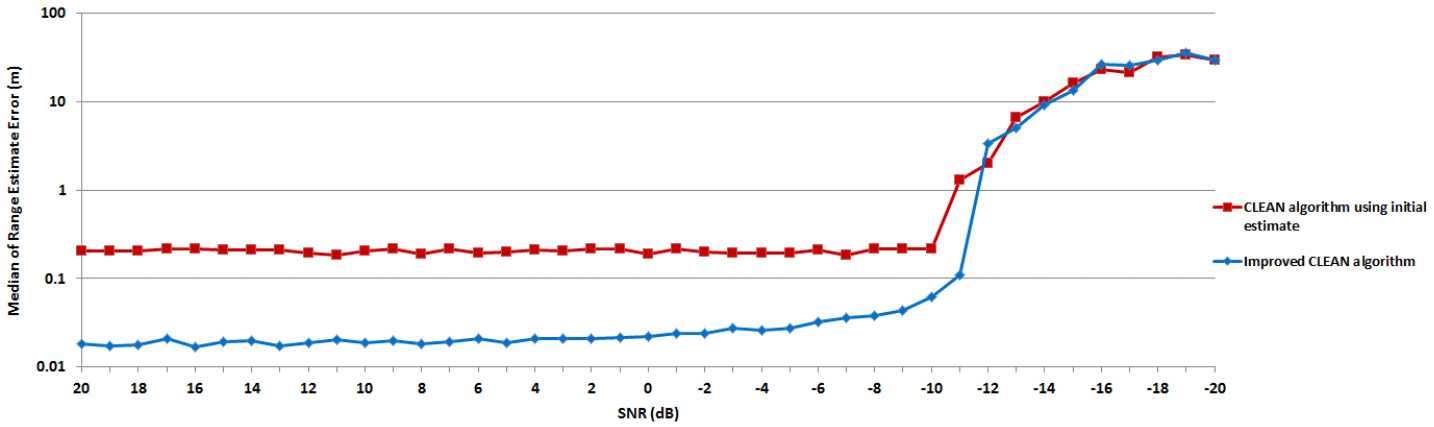

(a) Range estimates

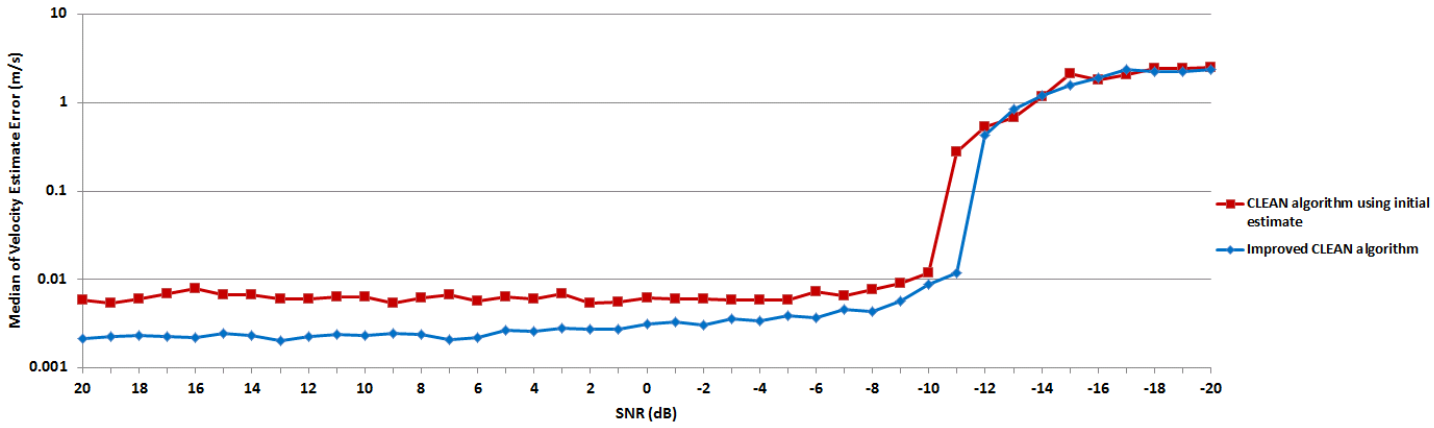

(b) Velocity estimates

Figure 5.7: Median of estimation errors for different SNR conditions

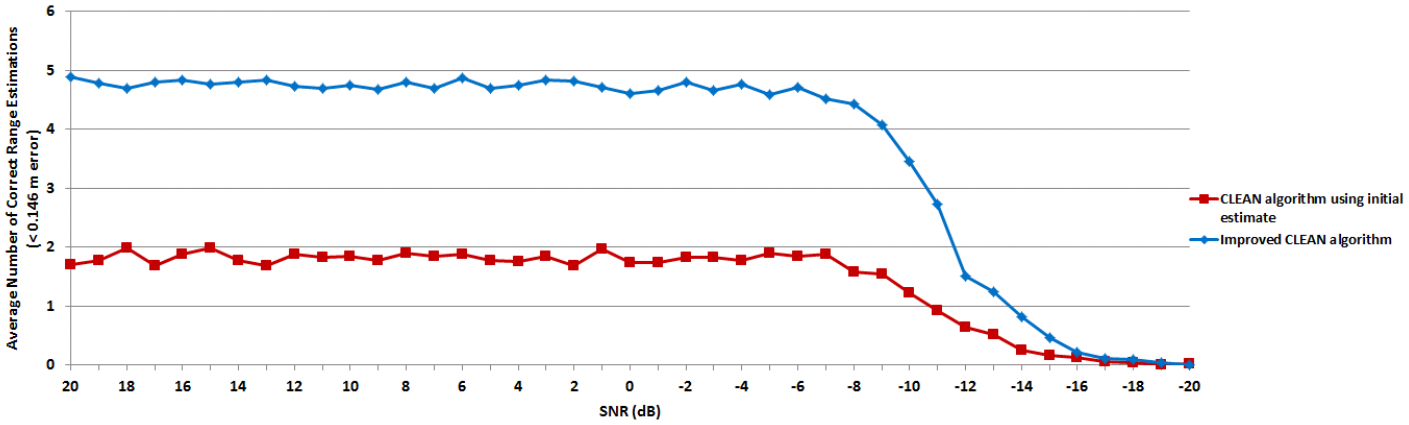

(a) Range estimates

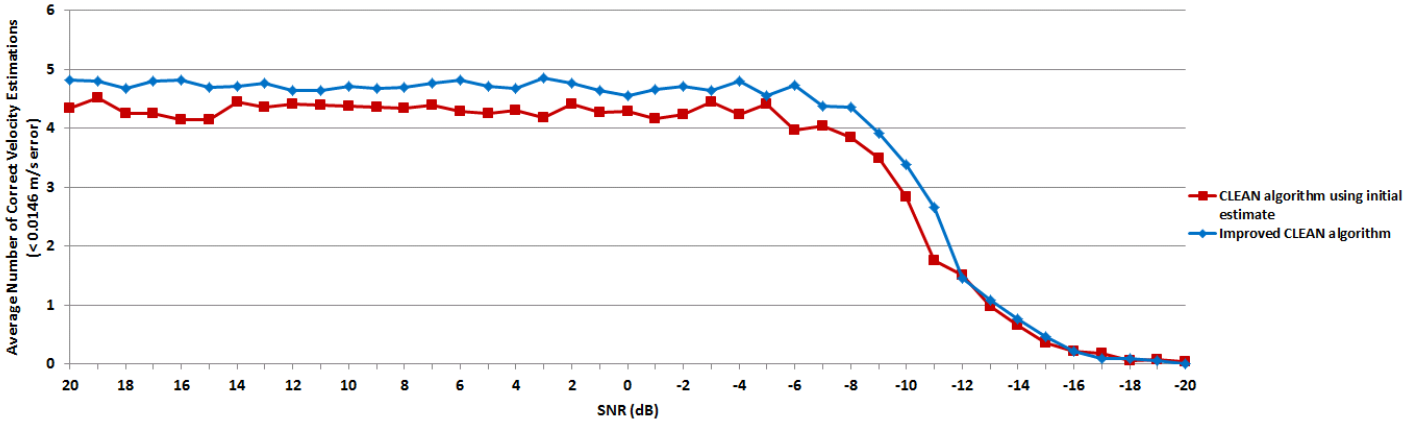

(b) Velocity estimates

Figure 5.8: Average number of correct estimations for different SNR conditions

Figure 5.6 plots the average range and velocity error against the different SNR conditions. It shows a roughly consistent trend in performance until it begins to degrade significantly at around -8 dB. Both the initial and improved estimates show a similar trend in performance. As was done in the previous section, it would be useful to corroborate these results by calculating and plotting the median of the errors, since averages can be affected significantly by large outliers, and this is done in Figure 5.7. Here the improved estimates are shown with a lower trend in estimation error compared to the initial estimates up until -12 dB. Looking at Figure 5.8 which plots the number of correct estimations, it shows that the improved estimates yield more correct estimations compared to the initial estimates up until -16 dB when the two trends start to overlap. It also shows that the performance of the improved estimates begin to decline at a slightly higher SNR compared to the initial estimates.

Overall, the CLEAN algorithm can be expected to perform adequately up until -10 dB. Then the performance degrades gradually until the algorithm is unable to yield any correct estimations beyond -18 dB, as shown in Figure 5.8.

5.5 Conclusion

In this chapter, the techniques making use of hopped frequency waveforms as described in Chapters 3 and 4 were applied to simulated rotating scatterers and it showed that they can be resolved in both down range and cross range (velocity).

Using these simulated scatterers, the performance of these techniques were further evaluated under different dominant scatterer amplitude and SNR conditions. The CLEAN algorithm can perform adequately up to conditions where the dominant scatterer is 13 dB above the other scatterers and a gradual decay in performance is seen thereafter up until 28 dB. At this point, no more than one scatterer (which is the dominant scatterer itself) is correctly detected and this is where the point of convergence occurs. In terms of SNR, the CLEAN technique has been shown to perform adequately above -10 dB and with degraded performance above -18 dB. At SNR below this, the algorithm fails to yield correct

estimations. One reason that these techniques can perform adequately in SNR conditions below 0 dB is due to the processing gain that comes with the IFFT operation to form the HRR profiles.

For both the dominant scatterer and SNR runs, the range and velocity estimates from the improved CLEAN algorithm of Section 4.4 were shown to have an improved performance over the CLEAN algorithm without the optimisation in terms of estimation error and number of correct estimations. Estimating the next scatterer requires finding its peak in the image and the sidelobes could be mistaken for that peak. At this point, the process will start to fail because the sidelobe subtraction that results from those spurious peak pixels would severely affect the peaks of the remaining scatterers. The remaining scatterer estimations would end up being erroneous. This will occur for the CLEAN algorithm using both the initial and improved estimates and therefore the large outliers from these erroneous estimations would yield a similar trend between the two when taking the average of these errors. However the performance advantage of the improved estimates can be seen when looking at the median of the errors and the number of correct estimations. As was mentioned in Chapter 4, the disadvantage of optimising the CLEAN algorithm is the increased computation time that is required.

These simulations show that the techniques developed in this work can potentially be applied to ISAR scenarios due to being able to resolve rotating scatterers in down range and cross range. Also, the range and velocity estimates of these scatterers can be obtained with reasonable accuracy in dominant scatterer and SNR conditions and can be used as measurements for tracking algorithms to track multiple scatterers. To improve on these simulations and make it more relevant to practical scenarios, extended rotating targets can be incorporated. Another consideration is that only uniform rotational motion was assumed here and the investigation can be extended to cases of complex rotation (in azimuth and elevation) as well as translational motion. Another consideration would be the effects of clutter in these simulations and this will be shown in Chapter 6.

Chapter 6

Simulation of Clutter

6.1 Introduction

This chapter touches on another area of practical consideration and that is to see how the techniques developed in this work apply to clutter conditions. It therefore starts off by describing how the clutter is incorporated into the simulations using correlated Gaussian noise. Then a performance evaluation is done under different SCR conditions using the rotating scatterers described in Chapter 5. Finally the chapter will conclude with a discussion of the results.

6.2 Clutter simulation

The clutter is modelled as correlated Gaussian noise to see the effect that it has on the techniques developed in this work. An m-file written by J. Strydom was used to generate the correlated noise samples for a given bandwidth. To fit this in the simulations, we assume that each sample represents a clutter reflectivity for a given range bin. The correlation bandwidth between the samples would represent the correlation between the range bins, using the fact that bandwidth is inversely proportional to range i.e. $\Delta r = c/2B$. This means that for smoother

terrains, such as grasslands or desert scenarios, more range samples would be correlated and this would mean a lower correlation bandwidth than, for example, urban scenarios. The SCR would determine the mean of this noise. An example of this is shown in Figure 6.1 where the clutter samples were generated with a correlation bandwidth of 1 MHz, to correlate 150 m of range, for an SCR of 20 dB.

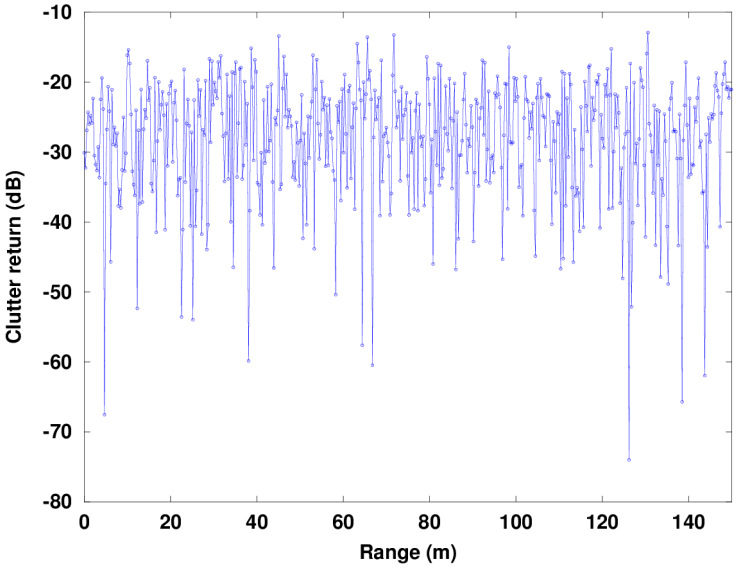

Figure 6.1: Range profile of simulated clutter for SCR of 20 dB

To apply this model of clutter to the simulations and to see how the methods described in Chapters 3 and 4 can be applied to it, each sample is modelled as a point scatterer as follows:

$$S_c(m) = \sum_{i=1}^{N} A_i \exp(\frac{-j4\pi f(m) R_i}{c}) \tag{6.1}$$

where A_i and R_i is the amplitude and range of each of the samples in the generated clutter noise respectively and N is the number of samples. This would be added into Equation 3.1 which is the signal containing the target. This model would hold if the clutter samples does not change from pulse to pulse and this can be assumed for stationary clutter.

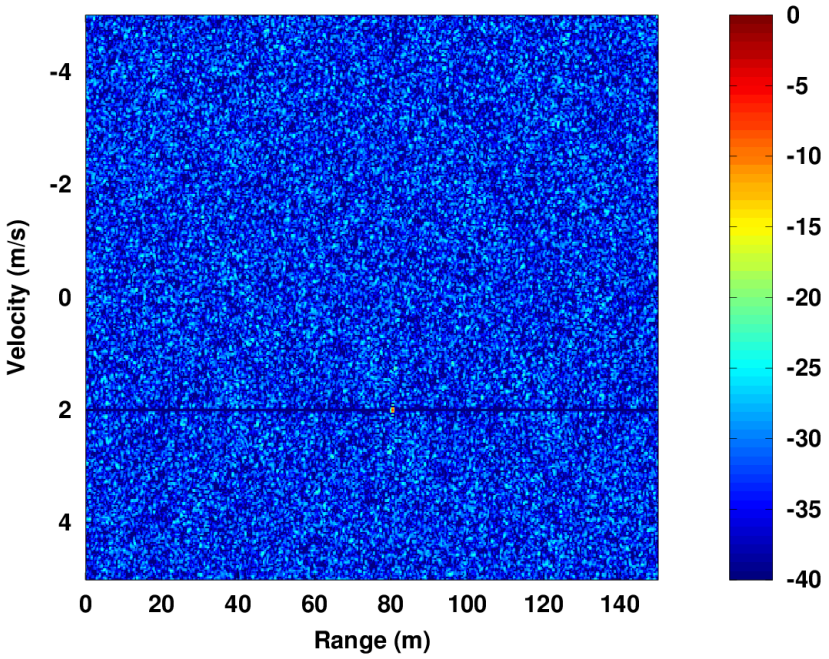

(a) No clutter

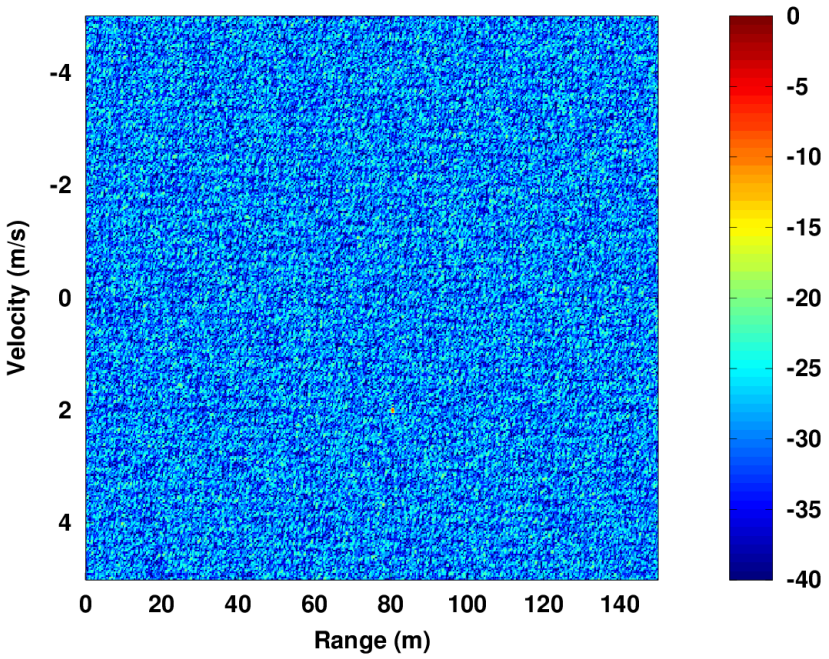

(b) Clutter at 20 dB SCR

Figure 6.2: Profiles of moving scatterer at 2 m/s

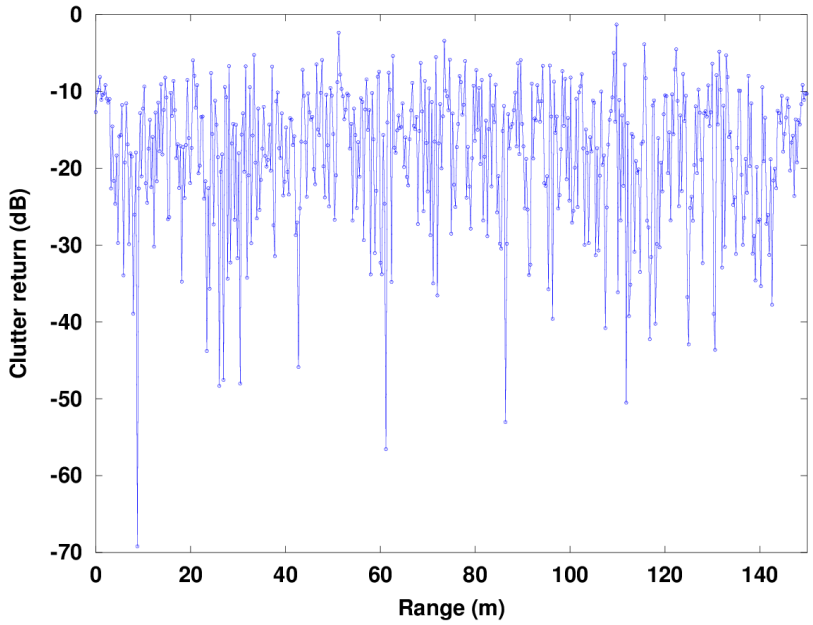

(a) Generated samples of 10 dB SCR clutter

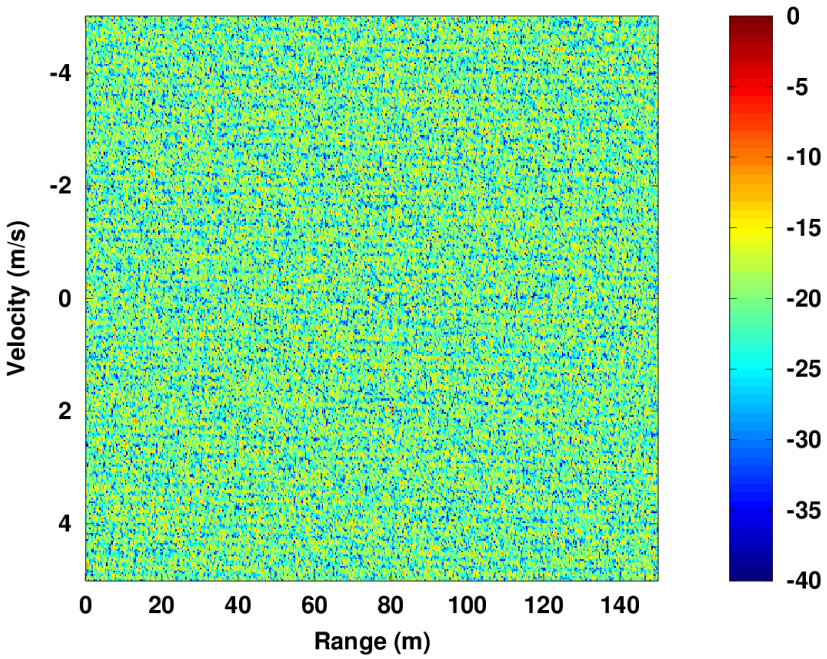

(b) Profiles of 2 m/s moving scatterer with 10 dB SCR clutter

Figure 6.3: Incorporation of 10 dB SCR clutter

Figure 6.2 compares the profiles of a moving scatterer at 2 m/s with and without the incorporation of the clutter samples shown in Figure 6.1. As shown in Equation 6.1, each clutter sample is treated as a point scatterer at different ranges along the zero velocity axis and therefore each clutter sample should have its own area of focusing at zero velocity. However the clutter point scatterers as a whole can be regarded as an extended target along the unambiguous range interval. It was mentioned in Section 4.5 that for a multiple scatterer case, each point scatterer would generates its own set of sidelobes and not only does this result in lower SFDR levels but their coherent summation would cause neighbouring scatterers to be affected in terms of amplitude and phase. For the clutter point scatterers stretching across 150 m of the unambiguous range, the sidelobes generated from all those scatterers would not only cause the overall sidelobe levels to increase but the points of focusing for the individual clutter point scatterers would be obscured. This is shown to be more severe when the clutter is at 10 dB SCR as shown in Figure 6.3.

6.3 Evaluation under SCR conditions

For this evaluation, the setup was the same as was done for the runs in Chapter 5 where 5 rotating scatterers were used, 100 monte carlo runs were done for each case and the performance was measured in terms of errors in range and velocity estimation. A 1 kHz PRF is assumed. In Appendix B, the clutter problem is looked at from a system's perspective and the SCR values for different system parameters, from best to worst case, were calculated and obtained. With these values, the SCR is stepped from 30 dB to -10 dB and the improved CLEAN algorithm described in Section 4.4 was used.

Figures 6.4 and 6.5 show the average and median of the results respectively. It shows an adequate performance in estimation error above 14 dB below which the performance degrades significantly. This can also be seen in Figure 6.6 where below 5 dB, the algorithm fails to yield correct estimations of the scatterers.

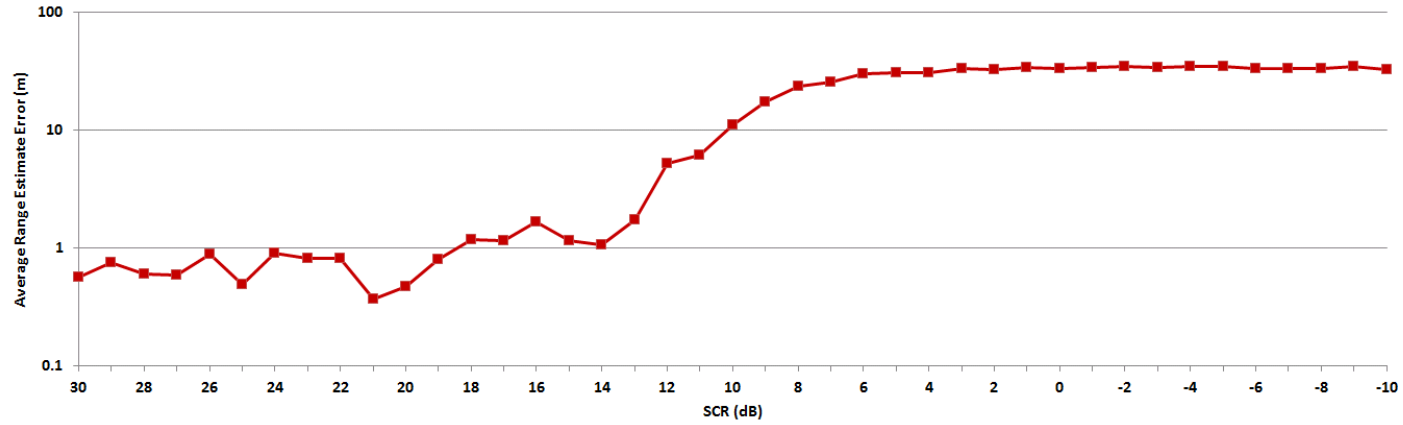

(a) Range estimates

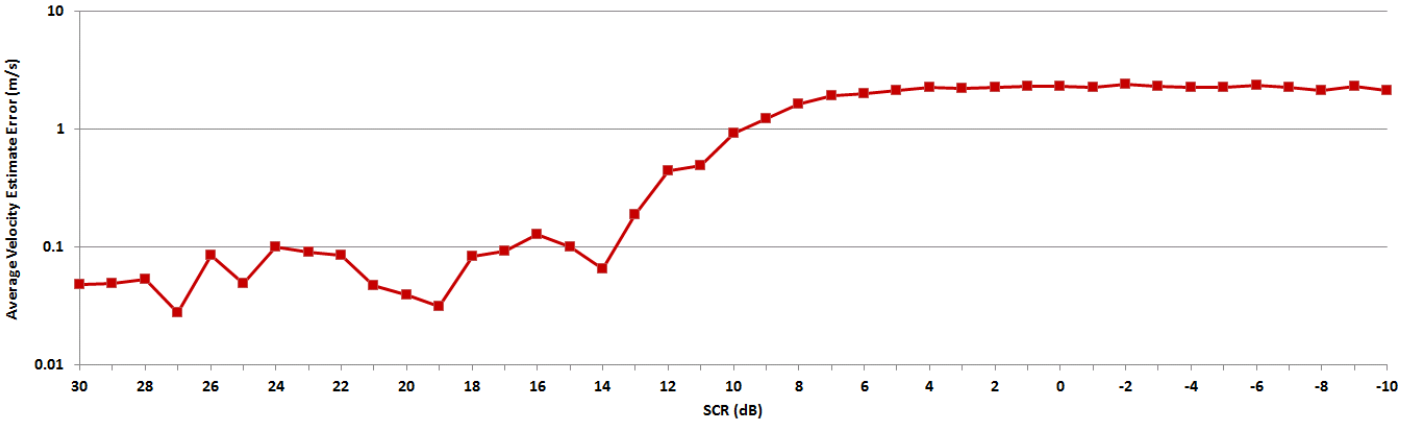

(b) Velocity estimates

Figure 6.4: Average estimation error for different SCR conditions

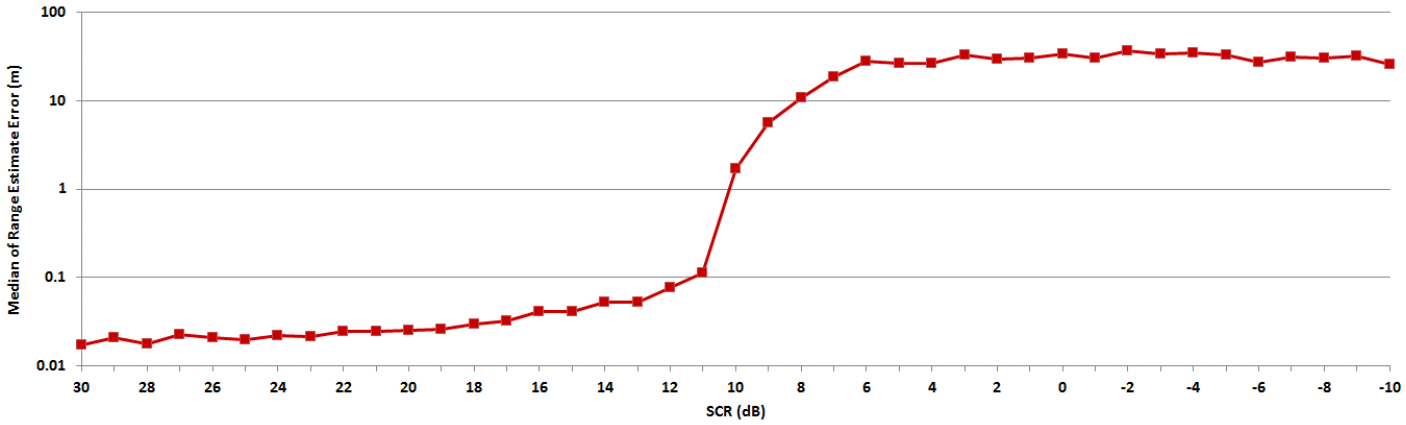

(a) Range estimates

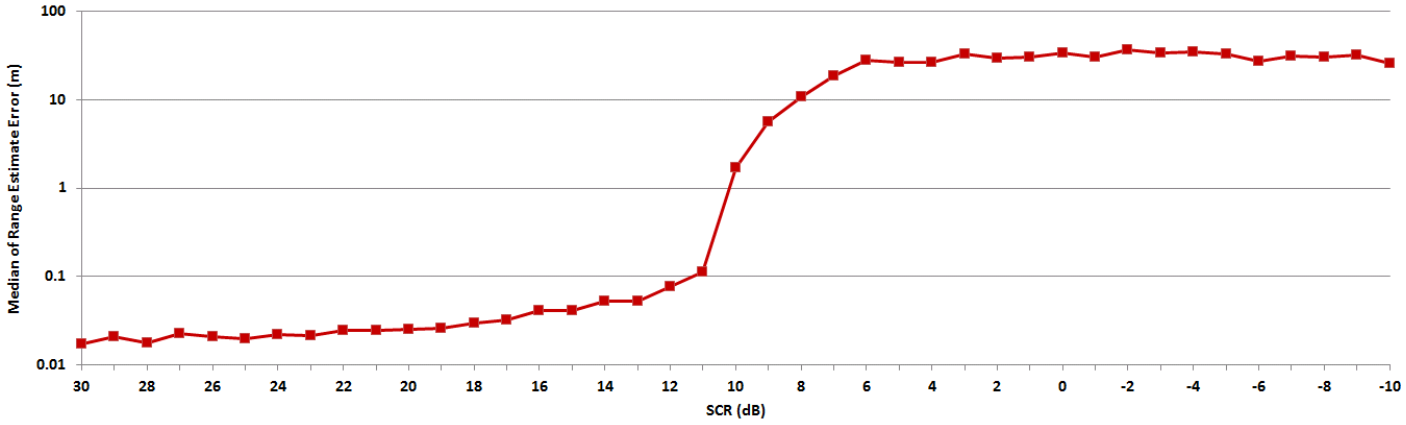

(b) Velocity estimates

Figure 6.5: Median estimation error for different SCR conditions

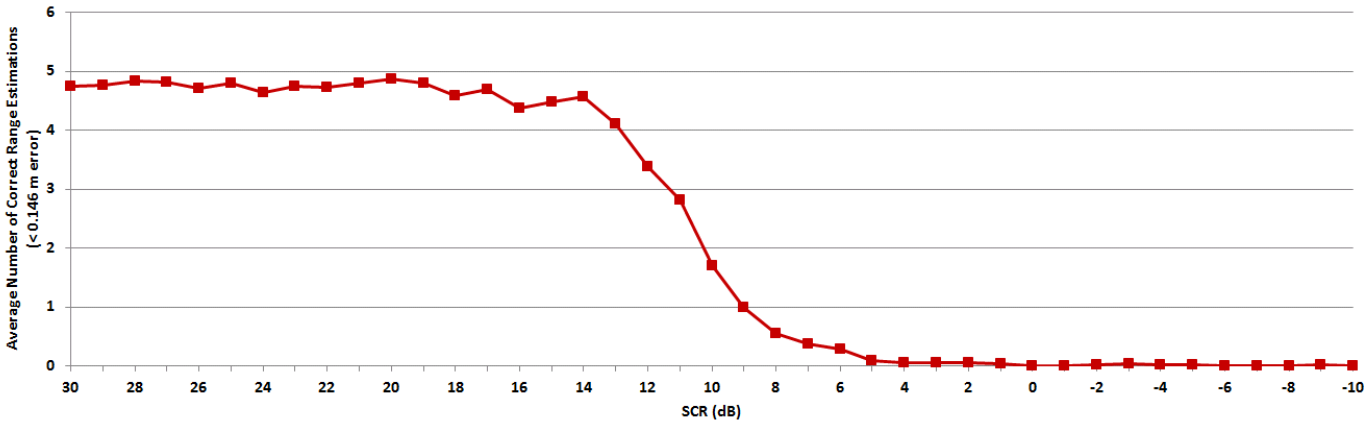

(a) Range estimates

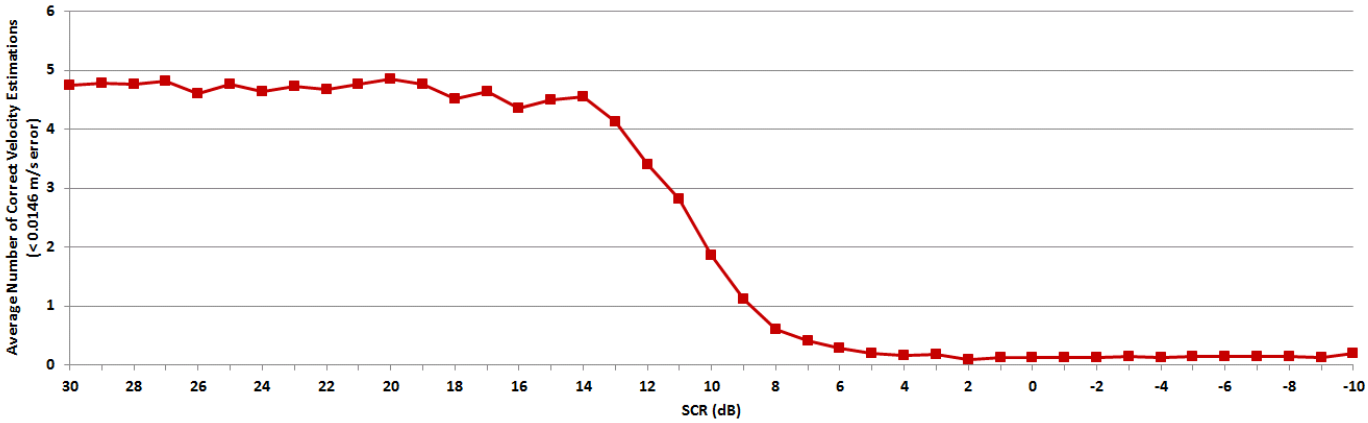

(b) Velocity estimates

Figure 6.6: Number of correct estimation for different SCR conditions

As was mentioned before, when generating the HRR profiles, each clutter sample would produce a sidelobe response and would contribute to the sidelobes in the profiles. Even at 10 dB SCR, as was shown in Figure 6.3(b), the scatterer peaks are masked by these sidelobes and this would therefore significantly degrade the performance of the CLEAN algorithm. Therefore the techniques developed in this work so far is not yet able to deal with low SCR and sub-clutter visibility. For now the evaluation was done only for the 1 kHz PRF case since it is shown in Tables B.3 and B.4 of Appendix B that the higher PRF cases result in even lower SCR values and the algorithm would not be able to fare in those conditions.

6.4 Conclusion

To incorporate clutter into the simulations, samples from correlated Gaussian noise were used where each sample was modelled as a clutter point scatterer. This clutter model is valid for samples that do not undergo change from pulse to pulse and this can be assumed for stationary clutter. This model of clutter would have to be modified when considering moving clutter. One way to do this would be to assign a random velocity component to the clutter point scatterers i.e. to incorporate $(R_i + V_i t)$ into Eq 6.1 where V_i would be a random velocity component of the clutter point scatterers.

Then a performance evaluation was done to test the techniques in this work, using the rotating scatterers, and they are shown to perform adequately above 14 dB SCR. Below that the performance degrades significantly. Therefore further improvements would have to be made on these techniques before they can be applied to scatterers in low SCR and sub-clutter visibility. One way to improve the performance of the techniques in these high clutter conditions is to incorporate some clutter mitigation scheme. This would involve some form of moving target indication (MTI) to isolate moving targets from near stationary clutter (and targets).

Chapter 7

Conclusions

7.1 Summary of results

In this work, hopped frequency waveforms were investigated to be able to obtain range and velocity measurements of targets and to resolve them. This would aid in the tracking of multiple scatterers by using the range and velocity measurements as inputs to tracking algorithms and would also allow imaging of rotating targets to take place due to being able to resolve between scatterers.

As was stated in Chapter 2, this method of using hopped frequencies to measure and resolve targets involved the following steps:

1. Apply motion compensation to the received signal at different velocities.
2. Form a two-dimensional matrix (in range and velocity) of HRR profiles where each profile is compensated at different velocities.
3. See where the profiles have the most focused mainlobe i.e no dispersion of the mainlobe energy. The true velocity of the scatterer(s) would likely be found by knowing which velocities those profiles were compensated for.

This method would allow imaging and tracking operations to take place with the advantages that come with hopped frequency waveforms such as range-Doppler

decoupling, reduced cross-talk between adjacent sensors and most importantly, robustness against ECM interference. This is due to the thumbtack ambiguity functions of hopped frequency waveforms. As seen in the results of Section 3.3, a peak is shown at the range and velocity location corresponding to the return from a particular scatterer and this allows that scatterer's measurements to be obtained. The other advantage is that this method allows the Doppler information to be extracted from a single return instead of on a burst-by-burst basis that is the case for conventional Doppler processing.

The disadvantage of hopped frequency waveforms using this approach is the high levels of sidelobes that each scatterer would contribute to the set of HRR profiles seen in the results. This creates a high noise floor, especially when dealing with multiple scatterers, that would interfere with imaging and tracking operations. As was seen in Section 3.5, transmitting and processing more pulses in the burst can allow a lower distribution of these sidelobes as well as better resolution. However this would require a higher bandwidth of the transmitted signal and dwell time on target. In Chapter 2, different methods for designing waveforms with desired ambiguity functions were described eg. using the Zak transform. However these methods aim to obtain a single sequence of hopped frequencies, or at least a set of such sequences, that would yield desirable ambiguity function characteristics and from an EW perspective, using only a certain set of hopped frequency sequences would limit their robustness against ECM. It was therefore useful to develop methods that could be applied to any sequence of hopped frequencies and would improve the SFDR of target measurements.

In Chapter 4, two approaches to improve the SFDR of target measurements were investigated. The first approach involved apodization. As was mentioned in Chapter 2, multi-apodization applies more than one window to a signal and the minimum output between those functions would be selected as that would allow the sidelobes to be reduced while still maintaining the mainlobe width of the unwindowed signal. Similarly, it was shown in Section 3.4 that different sequences of hopped frequencies correspond to different placement of sidelobes in the HRR profiles. This can be exploited by using different sets of results from different transmitted sequences of hopped frequencies and finding the minimum output

between those results. This would yield an overall set of HRR profiles with lower sidelobes and would help to improve the SFDR of the target measurements using the methods in this work. Figure 4.1 shows a reduction of the sidelobe levels by 10 to 15 dB after combining 10 sets of results. This approach can be applied to sequence of hopped frequencies which is an advantage against ECM due to frequency diversity.

However the apodization approach does not address the issue of large dwell times on target because transmitting, for example, 10 bursts of 512 pulses may not be practical for many radar operations. The other limitation to this approach is that the scatterer peaks would have to remain in the same range and velocity bin position while the entire apodization process is commencing otherwise the minimum output would cause that peak, or part thereof, to be cancelled. It also does not adequately deal with scatterers that are masked by the sidelobes of brighter scatterers. Therefore the other approach to improving the SFDR of the target measurements is through the use of the CLEAN technique. This technique involves finding the highest pixel in the image, generating its point spread function and using that to remove the energy that pixel contributes to the image. In Section 3.4, it was shown that the sidelobes that each scatterer contribute to the profiles is the ambiguity function of the transmitted set of hopped frequencies. As was shown in Equation 3.7, this can allow that scatterer's sidelobe contribution to be reproduced using the transmitted frequencies and time as well as the scatterer's estimated range, velocity and amplitude. This reproduced set of sidelobes would subtract from the profiles to remove the sidelobes from that scatterer. This would help to uncover smaller scatterers that are masked by the sidelobes of the more dominant scatterers.

Section 4.3 shows that just using a single sequence of transmitted frequencies, the sidelobe levels can be reduced to below -60 dB as seen in Figure 4.6. The CLEAN technique can also combine more than one of its results with apodization to yield even lower sidelobe levels. Therefore not only does the CLEAN technique give an improvement in SFDR over the approach using only apodization, but the dwell time requirements are being greatly lessened since one or two transmitted set of pulses can suffice for this operation.

However this approach, in order for it to perform adequately, requires tight error tolerances of the scatterer's estimated range, velocity and amplitude. This is because, as seen in Figure 4.9, errors in range, velocity and amplitude estimation of scatterers would result in high levels of residual sidelobes, especially for bright scatterers at 20 dB amplitude, and this would limit the CLEAN technique's ability to uncover smaller scatterers. As described in Section 4.4 and at the cost of increased computation, an optimisation was applied onto the CLEAN algorithm making use of the relationship between errors in range and velocity measurements and the residual sidelobe levels. While this method can improve the range and velocity measurements, improving the amplitude estimation remains a challenge. This leads on to one of the main limitations of the CLEAN approach which is that in this work, it is applied non-coherently onto a process that is coherent and does not take into account the phase information of the scatterers that would affect their peak amplitudes in the results. In order to apply the CLEAN technique coherently, the phase of the scatterers would have to be known.

Chapter 5 extends the applicability of the methods developed in this work by simulating rotating scatterers and showing how those scatterers are resolved in down range and cross range (velocity). This demonstrates how this work can be applied to an imaging scenario. An evaluation was done to see how these techniques, as applied onto the rotating scatterers, would fare under conditions of dominant scatterer amplitudes and noise. Dominant scatterer conditions were considered here to see how the CLEAN algorithm is able to uncover scatterers that are masked by the sidelobes of the dominant scatterer. This evaluation was done using monte carlo runs and the performance was evaluated in terms of errors in range and velocity measurements, since those measurements are of interest to tracking applications. It shows that the CLEAN algorithm performs adequately when the dominant scatterer is up to 13 dB in amplitude above the other scatterers. A gradual decay in performance is seen above that up until 28 dB which is the point of convergence. The techniques were also tested for different SNR. Here the techniques are able to perform adequately above -10 dB SNR and with degraded performance below that to -18 dB SNR. Below that the algorithm fails to yield correct estimations. A reason these techniques can

perform at SNR below 0 dB is the processing gain that comes with the IDFT operation. In these runs, the CLEAN algorithm using the improved estimates described in Section 4.4 are shown to have an improvement over the CLEAN algorithm without the optimisation i.e. using only the initial estimates. So far in this work, only point scatterer targets and uniform rotational motion were assumed.

Finally, to consider another area of practical importance, Chapter 6 investigates the simulation of clutter and how the techniques in this work fare under those conditions. In this work, the clutter is modelled as correlated Gaussian noise where each noise sample would represent a clutter point scatterer in range. Therefore each sample would contribute its own set of sidelobes to the profiles. This assumption would hold if these clutter samples do not undergo change from pulse to pulse and this can be assumed for stationary clutter. Moving clutter is not considered in this work. Like the performance evaluation done in Chapter 5, the techniques were tested for different SCR values using the rotating scatterers. Here the SCR is taken from the mean of the correlated noise samples. These SCR values were obtained from calculations done in Appendix B that looked at the clutter problem from a system's analysis. The techniques show adequate performance above 14 dB SCR and below that the performance degrades significantly. Therefore the techniques in this work are not able to deal with low SCR and sub-clutter visibility and some form of clutter mitigation, eg. moving target indication, would have to be incorporated so that these techniques are able to deal with these clutter conditions.

7.2 Future scope of work

7.2.1 Improving the model used in the simulations

In this work, the signal model as seen in Equation 3.1, makes the assumption that the scatterers are moving at a constant radial velocity and no intra-pulse modulation was assumed in the vector of frequencies $f(m)$. This work can be

extended to incorporate intra-pulse modulation such as Frank or Barker codes. It can also investigate acceleration, such as from manoeuvring targets, and how to account for that by possibly adding an acceleration term into the phase compensation and generating a 3D array of HRR profiles with acceleration as the third dimension. This would be an important consideration for the rotating scatterers used in this work since, for longer rotation times, the small angle approximation would not hold and the scatterers' radial velocities would not be constant.

Another consideration about the signal model is that it assumes point scatterer targets and this work can be extended to continuous targets. This would also apply to targets that are rotating for imaging purposes. In most cases, extended targets can be regarded as a collection of point scatterers sampled at the range resolution and it was shown in this work that each point scatterer contributes its own set of sidelobes to the profiles when using hopped frequency waveforms. Also to be taken into consideration is that for extended targets, adjacent scatterers would affect each other coherently and the sidelobe behaviour that results from this would have to be investigated. This would require a mathematical analysis into this behaviour.

With regards to the rotating scatterers used in this work, so far only uniform rotational motion was assumed and it was mentioned in Chapter 5 that this work can extend this model to translational and complex 3D rotation. In conventional ISAR processing, the translational motion is usually accounted for before ISAR imaging using the correlation or contrast cost functions. In this work, the translational motion could be compensated beforehand using the available techniques to do so and this would then leave only the rotational effects to dealt with using the techniques developed in this work. This would not be trivial if the rotation is non-uniform and this would have to be investigated.

Noise and interference is another consideration here. In this work, only AWG noise was considered and this can be extended by looking at the effects of phase noise. The other source of interference considered here was from clutter. In this work, the clutter model was limited to correlated Gaussian noise and non-Gaussian non-Rayleigh models such as K or Weibull distributed clutter can be

looked at especially if sea clutter is of consideration. This would mean that clutter that is non-stationary would have to be properly modelled. The incorporation of clutter would tie in with the investigation of extended targets since each clutter point scatterer would also contribute its own set of sidelobes. Therefore the clutter samples would affect each other coherently and this would affect the behaviour of the sidelobes.

7.2.2 Improving the techniques used in this work

One issue with the apodization approach was the number of results required to be combined to lower the sidelobe levels and this has implications on the required dwell times on target. One improvement to this approach is to find an optimal set of waveforms with results such that the apodization would yield the best improvement in sidelobe levels. Ideally this should be two waveforms where their results would have a complementary set of sidelobes and nulls and finding the minimum output between those results would theoretically cancel out the sidelobes while leaving the peak intact. Finding such a pair of sequences would require an optimisation approach and this could be done through the use of a genetic algorithm.

With regards to the CLEAN approach, it was also mentioned that improving the amplitude estimates remains a challenge due to the CLEAN technique being applied non-coherently and not taking the phase of the scatterers into account. Therefore estimating the phase and incorporating that into the CLEAN algorithm to make it coherent would be useful. This would be important when attempting to apply this technique to extended targets. It was mentioned in Chapter 2 that in [29], one approach to this problem is through the Sequence CLEAN method that uses search algorithms to find the best possible sequence to cancel the sidelobes from scatterer peaks. This method can be looked at to address extended targets but from a computational standpoint, it would be more useful if there was a way to have the CLEAN technique explicitly estimate the phase of the scatterers and not resort to using binary or tree search algorithms. It can also be extended to account for acceleration by working on a 3D array

of HRR profiles with acceleration on the third axis. These extensions to the CLEAN algorithm would add to its computational complexity and work can be done to make these algorithms more computationally efficient especially when dealing with tracking of fast targets.

More work can be done to compare the techniques developed in this work to conventional techniques of imaging and obtaining measurements for tracking algorithms, and also to other waveform design methods such as Zak transforms. Here the comparison could be done through a performance evaluation similar to what is done in Chapters 5 and 6 and the evaluation could be done in terms of errors in measurement, resolution, SFDR and computational efficiency.

7.2.3 Clutter mitigation

It was mentioned in Chapter 6 that some form of clutter mitigation would have to be incorporated in order to make the techniques in this work fare better under high clutter conditions.

One approach to this is to block all returns closer than a certain range in order to filter out nearby clutter and this would improve the SCR. This can be seen in Figure 7.1 which plots the clutter power of the ground returns at different ground ranges, using the parameters of Table B.2 to calculate the SCR in Appendix B, and most of the received clutter power can be seen at ground ranges closer than 1 km.

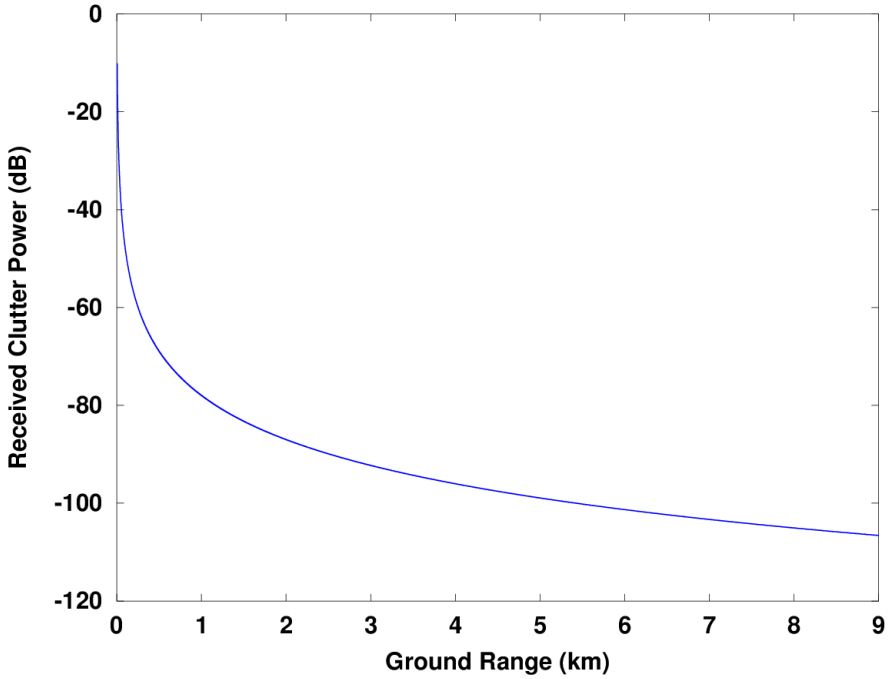

Figure 7.1: Plot showing received clutter power against ground range

Another approach would be to isolate fast moving targets from near stationary clutter. There are three possible approaches to this:

1. Based on traditional MTI, the profiles from a previous time instance can subtract into the result for the current time instance thereby cancelling out the clutter energy. This approach is more applicable for clutter that is not moving. However, just like the apodization approach, the scatterer peaks would have to remain in their range and velocity bin positions between the two time instances for this scheme to work.

2. Modifying the CLEAN algorithm such that all samples at a chosen velocity, as well as their sidelobe contributions, are removed from the profiles. This could be applied for both stationary and moving clutter. However since this approach deals with samples at all range bins for a given velocity, it is as though an extended target is being dealt with and this would require the CLEAN algorithm to be applied coherently.

3. Just like the windowing operation, this approach would involve designing some function that would be applied into the return signal before taking the IFFT to form the HRR profiles. This function would filter out the samples for a given velocity as well as their ambiguity responses. Since this approach would just involve multiplying this function into the return signal, this would bypass much of the computation that the other approaches entail. Designing such a function would require a mathematical analysis into the problem.

7.2.4 Application to practical radar systems and measured data

When the techniques in this work are able to deal with effects of acceleration, extended targets and real-world clutter conditions, it will be useful to apply this work to real world data. Here the measurements can be obtain from an actual radar system, such as MecORT from the CSIR, and the processing can at first be done offline with recorded data stored on a computer e.g. forming ISAR images from raw data. If these techniques are computationally efficient enough, they could then be applied in systems working in real time. This would be more applicable if these techniques were used to obtain measurements for tracking algorithms and the performance of the tracking system can be evaluated using these methods. Since one of the main considerations of this work is frequency diversity in an EW environment, this work can also be tested on systems that are under the effects of ECM and jamming.

Appendix A

Algorithm Flow Charts

This section describes the algorithms in flow chart format that are used for the techniques mentioned in Chapter 4. It goes on to describe the CLEAN algorithm, the peak detection algorithm and the algorithm to improve the CLEAN algorithm.

The peak detection algorithm is used to determine the indices of the peak pixels in the image and this is required to cancel the peak pixels during the CLEAN operation. An important consideration is choosing a threshold. If the difference between the peak and that pixel value is more than the threshold then that pixel would not be considered as part of the peak. This threshold would depend on the overall sidelobe levels and would therefore be calculated as follows:

$$Threshold = 20log_{10}(2(M)) \tag{A.1}$$

where dB values are used in the algorithm and M is the median of the entire image.

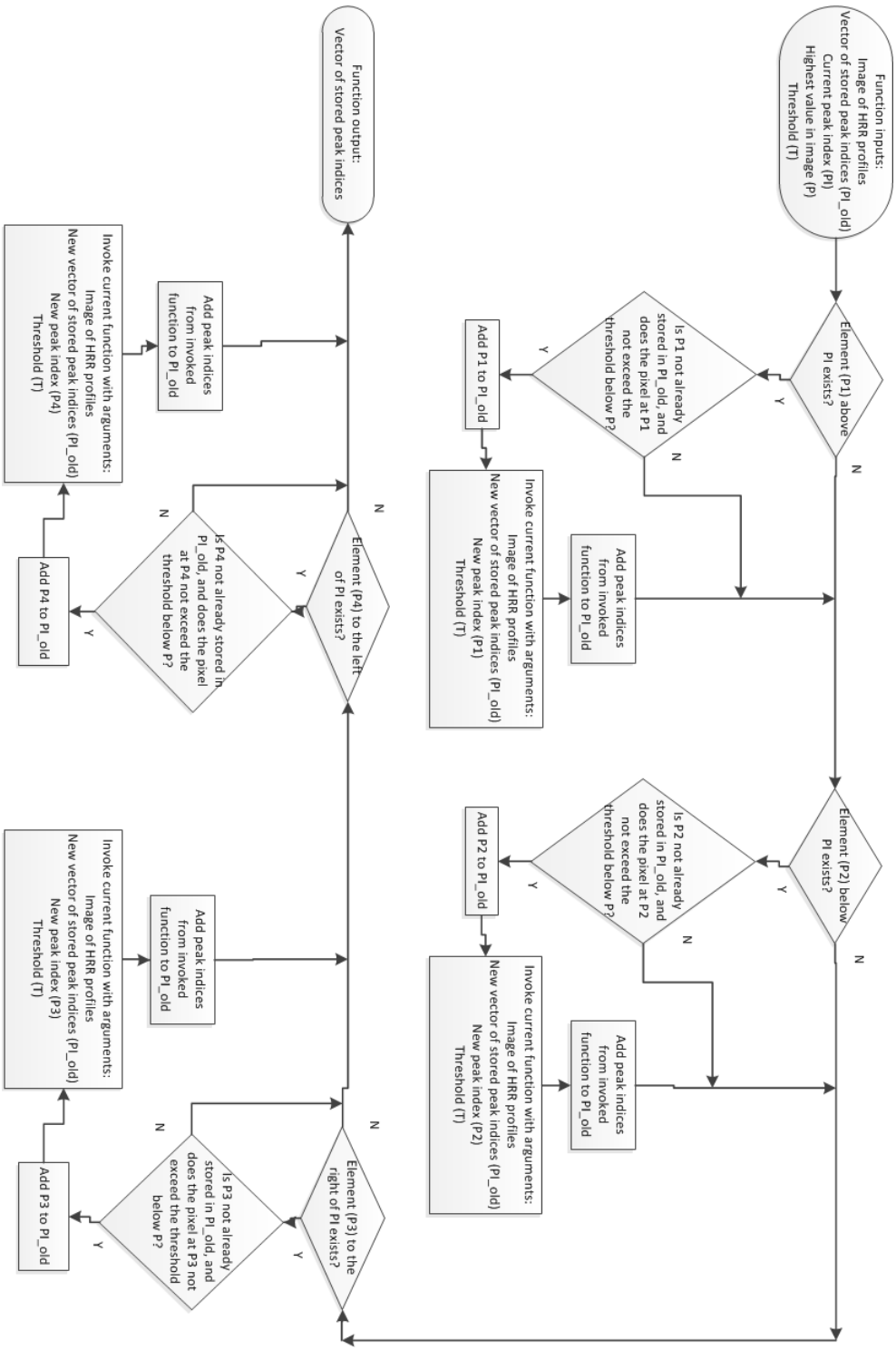

Figure A.1: Flow diagram of peak detection algorithm

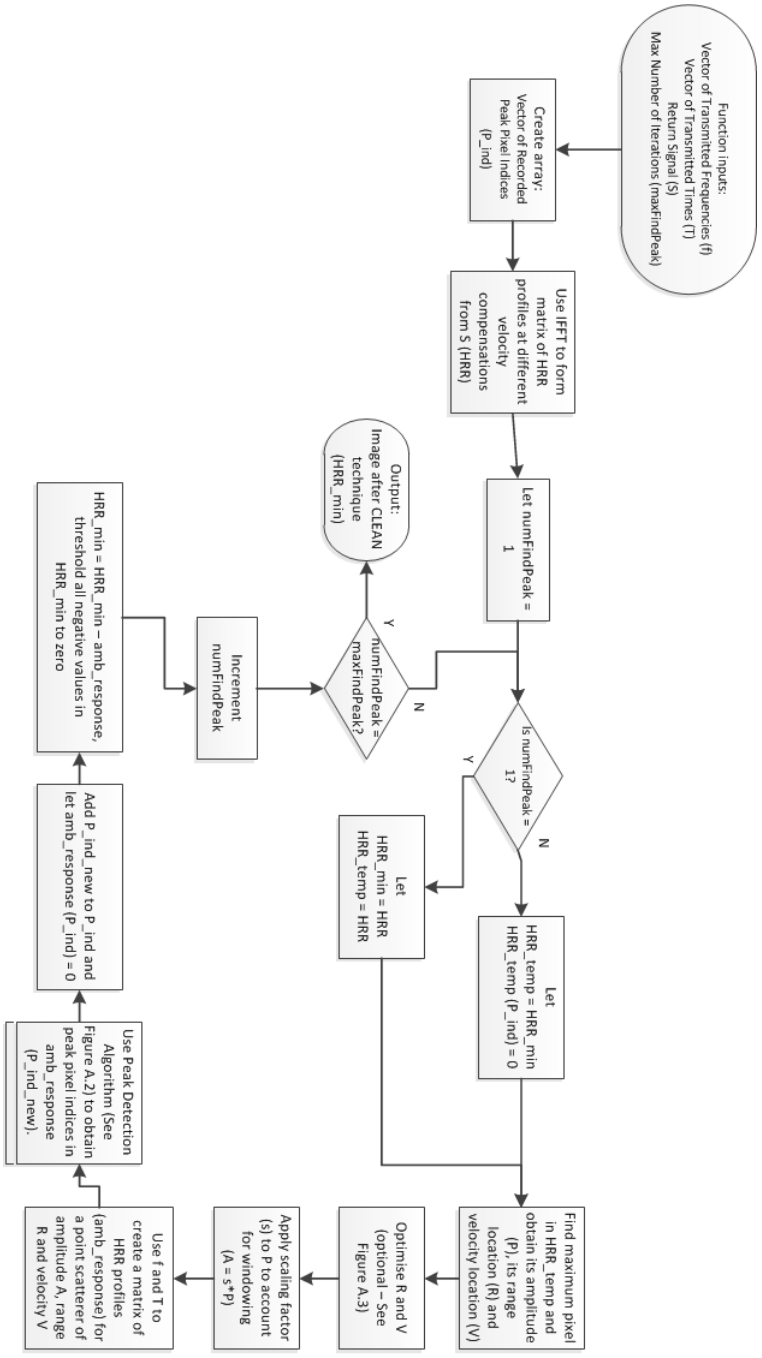

Figure A.2: Flow diagram of CLEAN algorithm

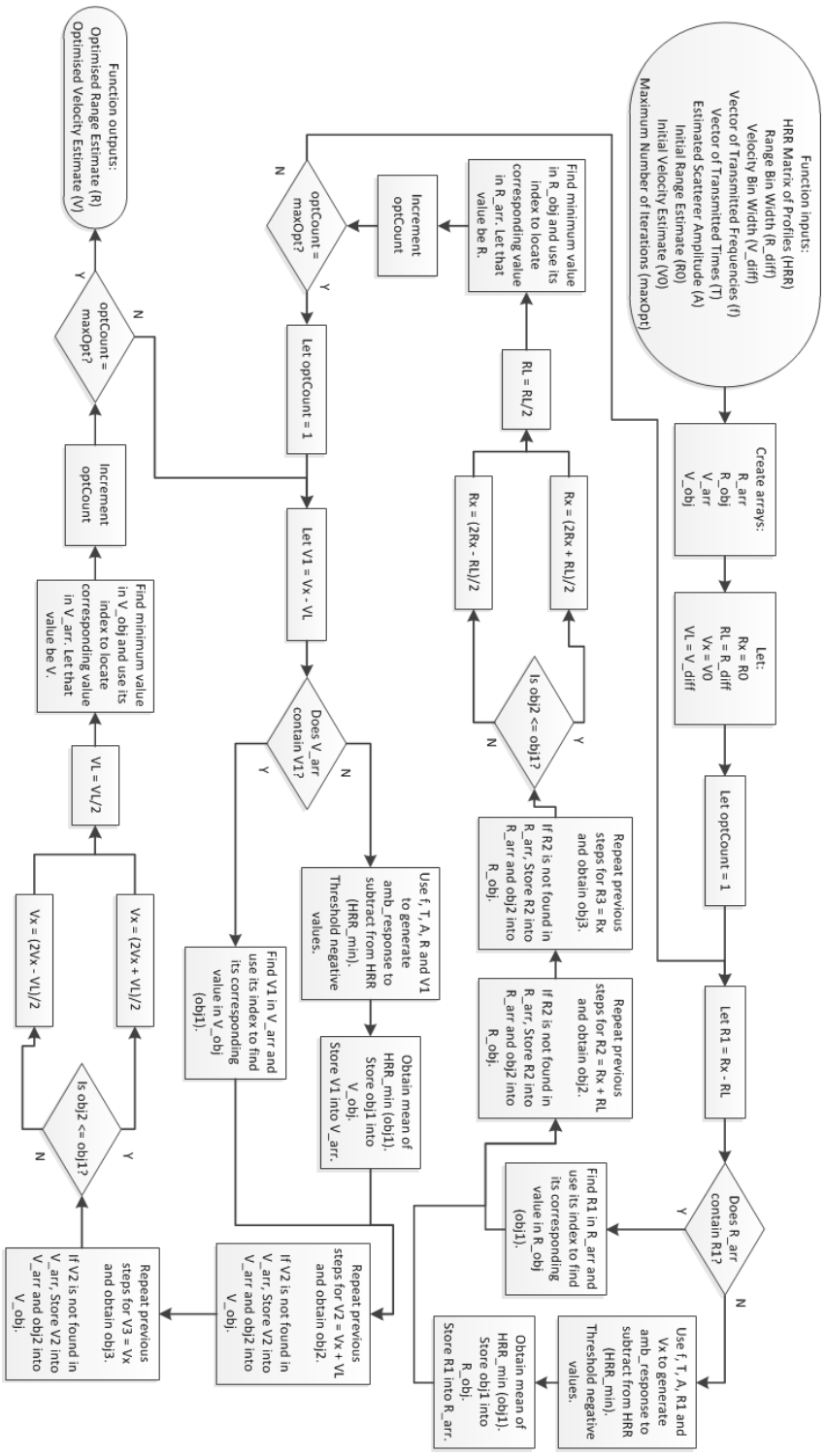

Figure A.3: Flow diagram to optimise CLEAN algorithm

Appendix B

System's Analysis of Clutter Problem

B.1 Overview of scenario and assumptions

The objective here is to find values of SCR that can be used in the simulations and this section will therefore will look at the clutter problem from a system's viewpoint. The scenario involves a ground-based radar illuminating an air target at a given elevation look up angle. While this is occurring, the sidelobes of the antenna as well as part of the mainlobe would be illuminating the ground at different incidence angles and the returns therefrom would give rise to clutter. Here the signal to clutter ratio (SCR) calculation concerns a particular target situated in a certain fine range bin (after HRR processing). For an unambiguous range extent, the clutter energy would result from the ground returns at many ambiguous ranges folding into the range bin containing the target. Other scenarios such as air-to-ground operations are not considered in this work.

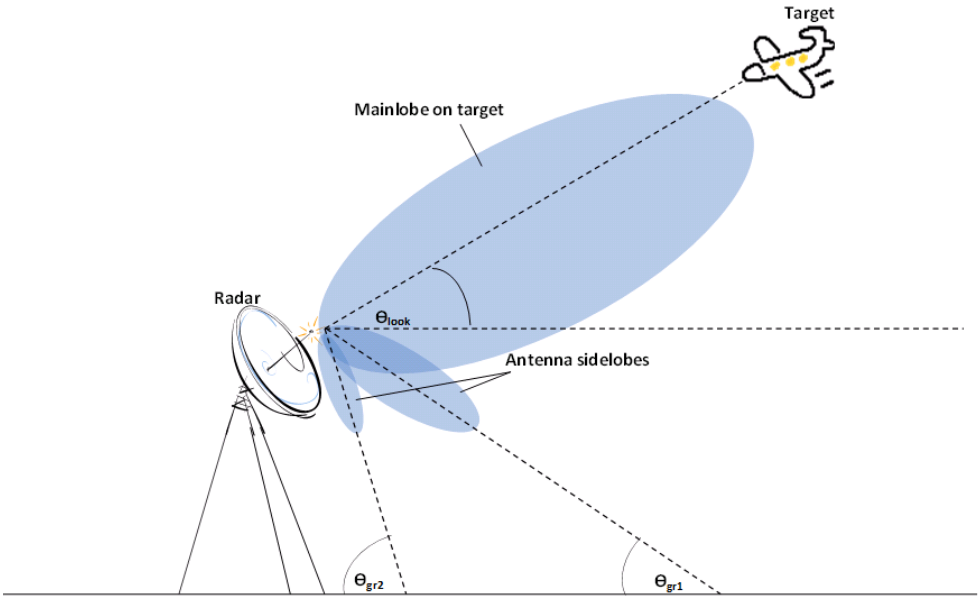

Figure B.1: Scene depicting ground radar illuminating air target

Figure B.1 shows the scenario of a radar illuminating an air target at an elevation look up angle (θ_{look}). As this is occurring, the ground is illuminated by the antenna sidelobes at different grazing angles (θ_{gr1} and θ_{gr2}) and this forms the clutter returns seen in the measured data. This would also occur for returns from the ground that are ambiguous in range and they would fold into the fine range bin containing the target. As shown in Figure B.2, at all azimuths, this would form an arrangement of illuminated patches of rings on the ground where, for the range bin containing the target, the ground clutter returns would be received and would compete with the return from the target. These rings would be spaced by the ambiguous range interval ($R_2 - R_1$) and would be of width Δr which is the width of the range bin. There is also a blind range (R_{blind}) that is due to the radar not receiving echoes during transmission and therefore the first range ambiguous ring would occur after this blind range.

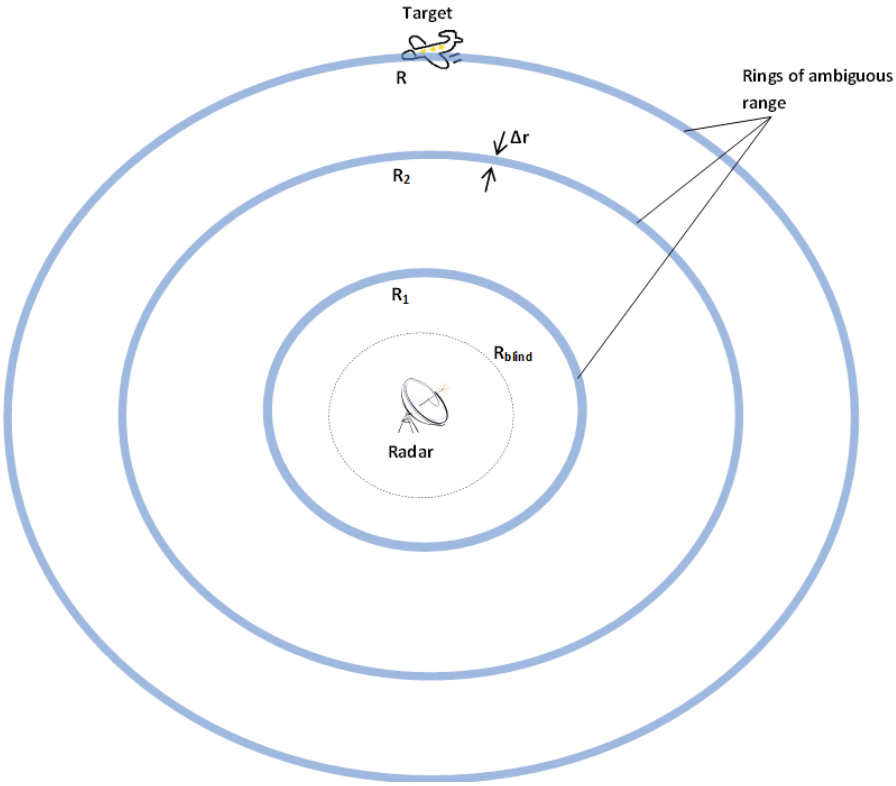

Figure B.2: Rings of ambiguous range for target at range R

In both elevation and azimuth, the antenna main lobe gain pattern is generated using the $sinc^2$ function. In azimuth, the gain pattern for all 360° is generated. To calculate the clutter return from a particular ring, the azimuth gain pattern (scaled by the antenna gain in elevation) would be integrated across all 360° of that ring.

Some mention has to be made on range ambiguity. When generating the HRR profiles, the range extent of those profiles would be dependent on the sampling rate of the IFFT. In this case, it is the frequency step size Δf that determines this range extent i.e $R_{amb} = c/2\Delta f$ and is also the course range bin size. Any return that occurs after R_{amb} would fold into the profiles. This is shown in Figure B.3 where for a target at range R, the energy at $R_1 = R + R_{amb}$ folds into the range bin at R and interferes with the target return. This would occur for all ambiguous ranges at multiples of R_{amb} up until the end of the PRI for the

pulse with frequency f_1. This is because when the next pulse is generated with frequency f_2, the filter in the receiver changes its frequency and we assume that no energy from the previous pulse is able to leak into the receiver. Therefore no returns for f_1 can be received when transmitting the subsequent set of pulses until f_1 is transmitted again at the next burst repetition interval (BRI). In our calculations, the returns after the BRI is not considered due to those ranges being large enough such that we can assume that the inverse R^4 attenuation would make those returns negligible.

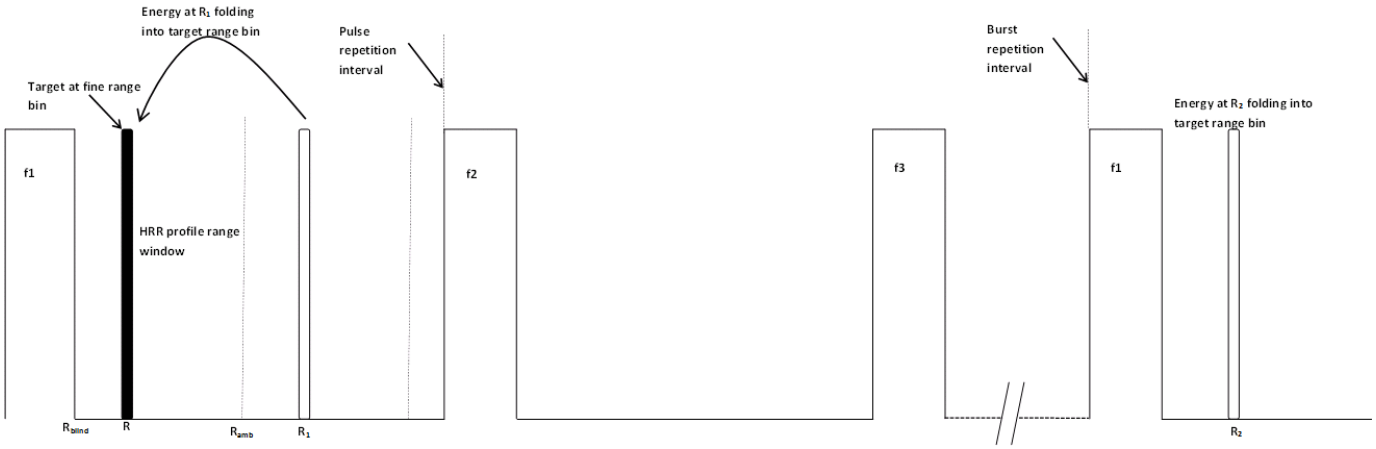

Figure B.3: Diagram showing ambiguous ranges in PRI

To calculate the incidence and grazing angles, the spherical earth geometry is used as shown in Figure B.4 where h is the height of the radar antenna, a is the earth radius, R_i is the radial range to the ground, θ_{in} is the incidence angle from the radar and θ_{gr} is the grazing angle to the earth surface. The incidence angle is needed to obtain the elevation antenna gain while the grazing angle is needed to obtain the surface reflectivity at that point on the ground. When using the spherical earth geometry, the radar horizon (R_h) has to be taken into account. This is the maximum range that the radar can detect ground clutter due to the curvature of the earth. To take into account the refraction of the radar beam, an earth radius scaled by 4/3 will be used i.e $a = (4/3) \times 6378km$.

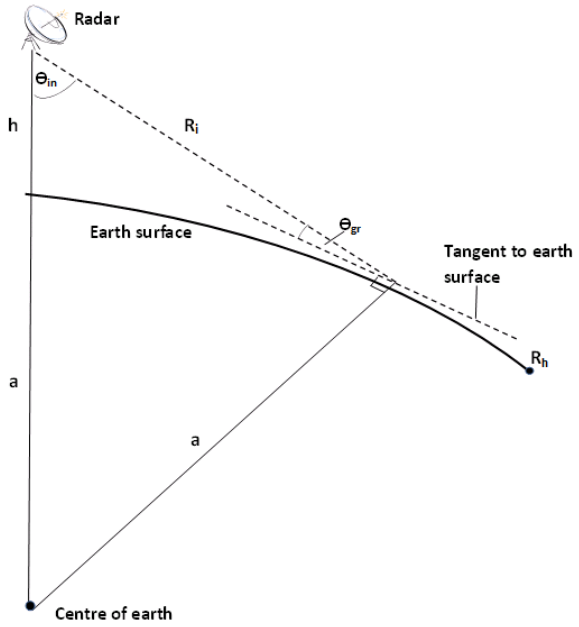

Figure B.4: Radar scenario with spherical earth geometry

Therefore the assumptions are:

- The full azimuth and elevation beam patterns are generated using the $sinc^2$ function.
- The target is always centred onto the peak of the mainlobe.
- A spherical earth geometry using a 4/3 earth radius to account for refraction of the beam.
- No returns will be considered before the blind range, and after the PRI or the radar horizon range whichever occurs first.
- All clutter is stationary with respect to the radar.
- Multipath effects are not considered.

B.2 SCR calculation

Table B.1: List of parameters for SCR calculation

Name of Parameter	Parameter Symbol	Calculation
Carrier frequency	f_c	
Frequency step size	Δf	
Pulse repetition frequency	PRF	
Number of pulses in the burst	M	
Wavelength	λ	$\lambda = c/f_c$, c is the speed of light
Bandwidth	B	$B = M \times \Delta f$
Range resolution (assuming no windowing loss)	Δr	$\Delta r = c/2B$
Coarse range bin	R_{amb}	$R_{amb} = c/2\Delta f$
Ambiguous range interval (for pulse)	R_{PRI}	$R_{PRI} = c/2PRF$
Height of radar	h	
3 dB azimuth beamwidth	θ_{azbeam}	
3 dB elevation beamwidth	θ_{elbeam}	
Elevation look up angle	θ_{look}	
Peak transmitted power	P_t	
Peak mainlobe gain	G_{main}	
Duty cycle	DC	
Pulse length	τ	$\tau = DC/PRF$
Blind range	R_{blind}	$R_{blind} = c\tau/2$
Radar horizon range	R_h	$R_h = \sqrt{2ha}$, $a = (4/3) \times 6378km$
Range of target	R	
Target RCS	σ_t	

Table B.1 shows the parameters that are used in the calculation of SCR. To generate the antenna gain functions, the following formula is used for elevation:

$$G_{el}(\theta_{in}) = G_{main} \times sinc^2((\theta_{in} + \theta_{look})/\alpha) \tag{B.1}$$

where α is a scaling to get to the 3 dB beamwidth of θ_{elbeam}. Figure B.5(a) shows an example of a generated elevation antenna gain pattern with $\theta_{elbeam} = 10°$ and $\theta_{look} = 30°$. This gain will be obtained from the incidence angle θ_{in}.

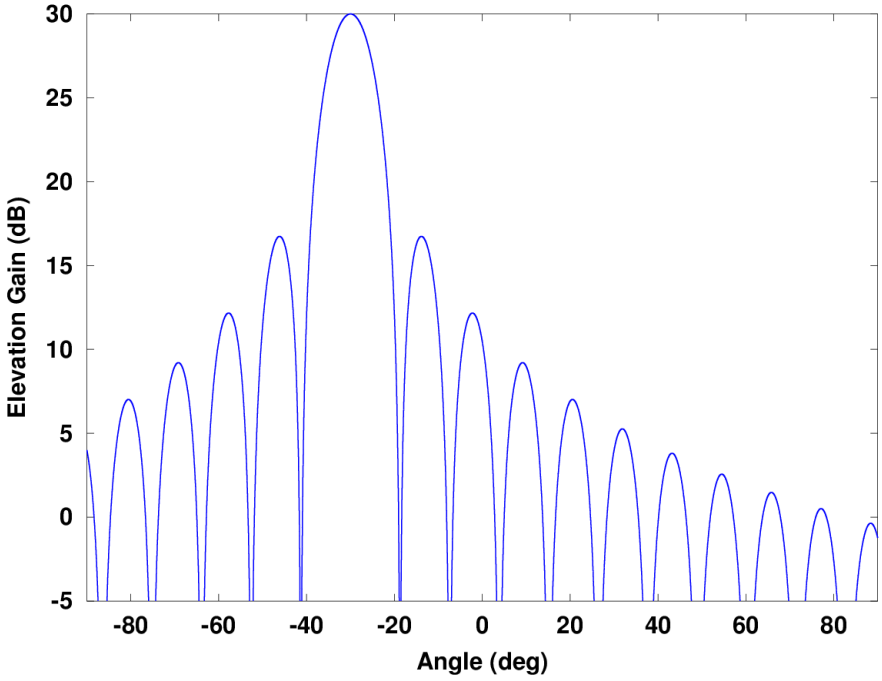

(a) $\theta_{elbeam} = 10°$ and $\theta_{look} = 30°$

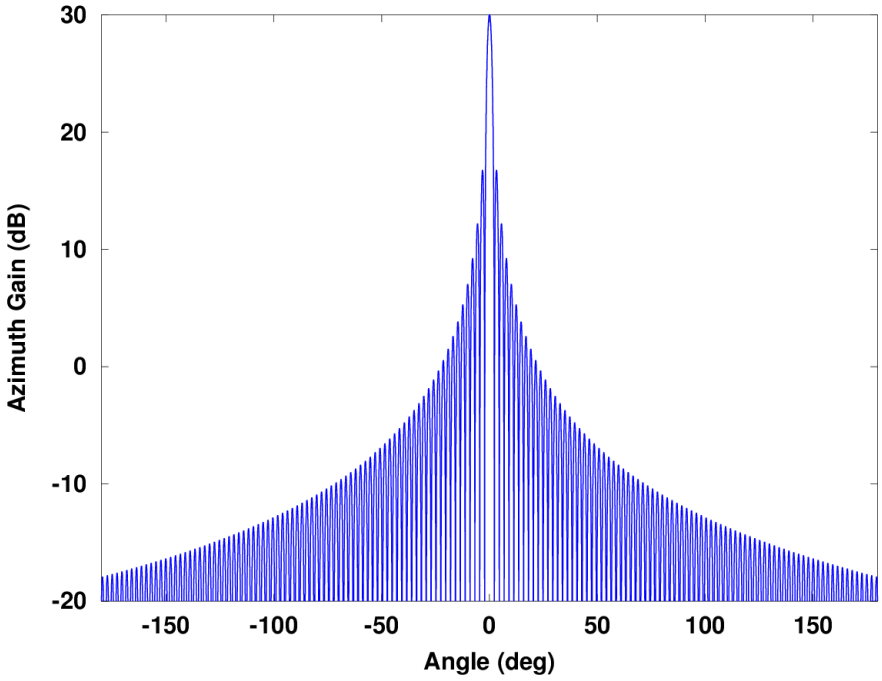

(b) $\theta_{azbeam} = 2°$

Figure B.5: Plots showing elevation and azimuth antenna gain patterns

Similarly, the azimuth gain function (weighted by the elevation gain) is generated by:

$$G_{az}(\theta) = G_{el}(\theta_{in}) \times sinc^2(\theta/\beta) \tag{B.2}$$

where β is a scaling to get to a 3 dB beamwidth of θ_{azbeam}. Figure B.5(b) shows an example of a generated azimuth antenna gain pattern with $\theta_{azbeam} = 2°$. In both cases, the peak mainlobe gain $G_{main} = 30dB$.

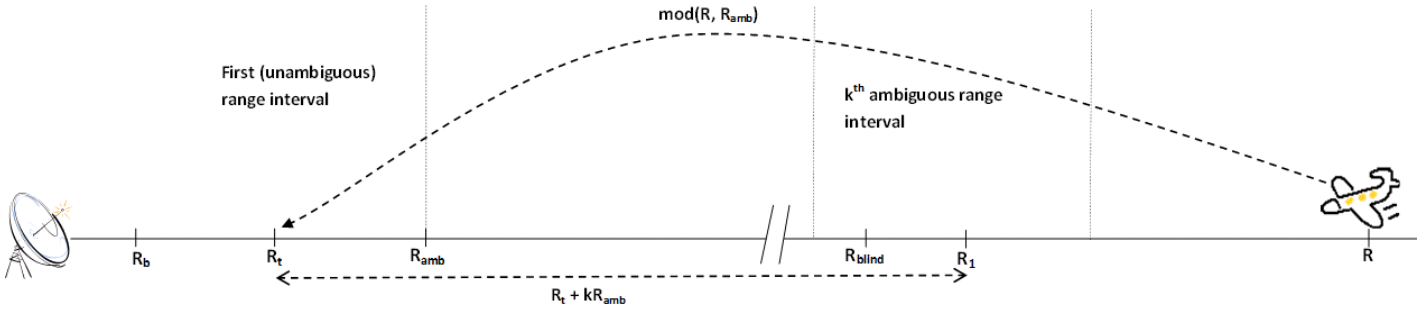

Figure B.6: Range axis showing how R_1 is determined

The first illuminated ring patch would occur after the blind range (R_{blind}) at range R_1. This is determined in the following way (shown in Figure B.6):

1. Determine how many ambiguous range intervals after the unambiguous range interval R_{blind} falls into: $k = floor(R_{blind}/R_{amb})$, where k is rounded to the lowest integer.
2. Find where the target range would fold into the unambiguous range interval: $R_t = mod(R, R_{amb})$, mod being the modulo operation.
3. If $R_t + kR_{amb} > R_{blind}$, then $R_1 = R_t + kR_{amb}$.
4. Otherwise proceed to the next range interval after the blind range, $R_1 = R_t + (k+1)R_{amb}$.

Then for each ambiguous range ring ($R_n = R_1 + nR_{amb}$), the following calculations are performed:

Looking at the spherical earth geometry in Figure B.4, the incidence angle from the radar is calculated by:

$$\theta_{in} = cos^{-1}((h+a)^2 + {R_n}^2 - a^2)/(2R_n(h+a)) \tag{B.3}$$

where the cosine rule is applied. The grazing angle is found relative to the tangent of the earth surface by:

$$\begin{gathered} \theta_e = cos^{-1}({R_n}^2 + a^2 - (h+a)^2)/(2R_n a) \\ \theta_{gr} = \theta_e - 90^\circ \end{gathered} \tag{B.4}$$

The grazing angle θ_{gr} would be used to obtain the surface reflectivity coefficient $\sigma_c(\theta_{gr})$ using a tool developed by K. Naicker, which makes use of a table of coefficients based on a clutter model developed by Georgia Tech Research Institute (GTRI).

The clutter power from each ring will be calculated by integrating the azimuth antenna gain across 360° of the ring. To do this, an incremental area of the ring has to be defined:

$$dA = \Delta r(R_n - 0.5\Delta r)d\theta \tag{B.5}$$

where $d\theta$ is the angular step size of the azimuth gain function. The clutter power from each ring is thereafter calculated by:

$$P_n = \sum_{\theta=-\pi}^{\pi} \frac{P_t \lambda^2 \sigma_c(\theta_{gr})}{(4\pi)^3 R_n^4} G_{az}(\theta)^2 dA \tag{B.6}$$

This iterative process will terminate when either $R_n > R_{PRI}$ i.e for ranges beyond the PRI or when $R_n > R_h$ i.e for ranges beyond the radar horizon. The total

clutter power from all the ambiguities folded into the range bin of the target is:

$$P_{clut} = \sum P_n \tag{B.7}$$

Then for the target of interest, the signal power is found by:

$$P_{sig} = \frac{P_t G_{main}^2 \lambda^2 \sigma_t}{(4\pi)^3 R^4} \tag{B.8}$$

Finally, the SCR is calculated as follows:

$$SCR = \frac{P_{sig}}{P_{clut}} \tag{B.9}$$

B.3 Obtaining SCR values

Table B.2: List of parameter values for SCR calculation

Name of Parameter	Parameter Symbol	Value
Carrier frequency	f_c	$5GHz$
Frequency step size	Δf	$1MHz$
Pulse repetition frequency	PRF	$1kHz$
Number of pulses in the burst	M	512
Bandwidth	B	$M \times \Delta f = 512MHz$
Range resolution (assuming no windowing loss)	Δr	$c/2B = 0.3m$
Coarse range bin	R_{amb}	$c/2\Delta f = 150m$
Height of radar	h	$5m$
Radar horizon range	R_h	$\sqrt{2ha} = 9.2km$
3 dB azimuth beamwidth	θ_{azbeam}	2°
3 dB elevation beamwidth	θ_{elbeam}	10°
Peak mainlobe gain	G_{main}	$30dB$
Duty cycle	DC	5%
Target RCS	σ_t	$1m^2$

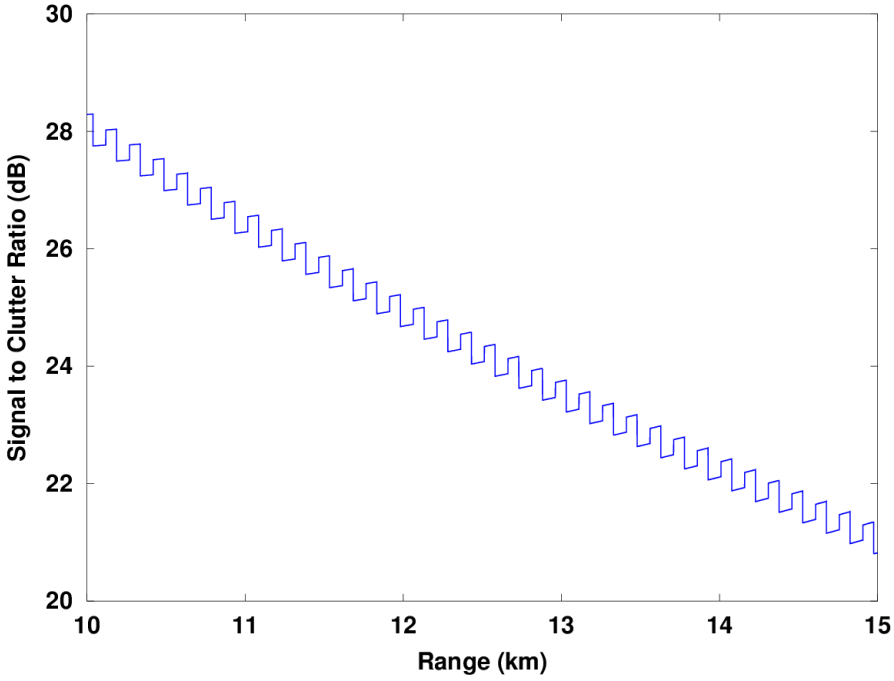

(a) SCR values

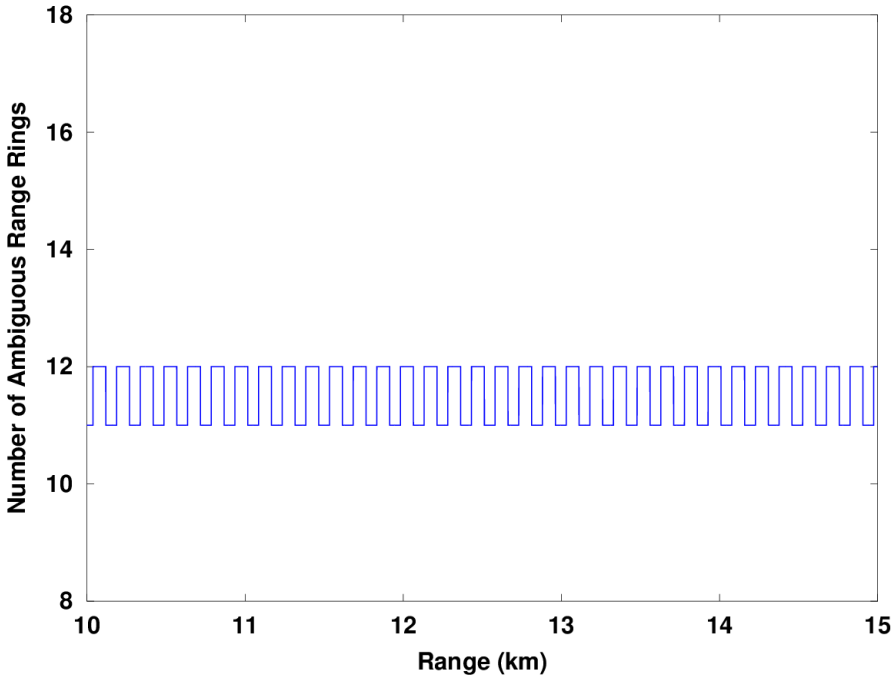

(b) Number of range rings in calculation

Figure B.7: Plot of SCR values for $\theta_{look} = 5°$

Table B.2 shows the parameters that have been chosen to calculate the SCR values. For a best case scenario, we consider a radar with a look up angle of 5°. Figure B.7(a) shows the SCR values that have been obtained with this look up angle for target ranges from 10 km to 15 km. The SCR plot shows a decreasing trend, from 28 dB to 22 dB, due to the signal power decreasing for further ranges, a consequence of the inverse R^4 law. The jagged behaviour of the plot is due to the change in the number of range rings to calculate the SCR and this can be seen in Figure B.7(b).

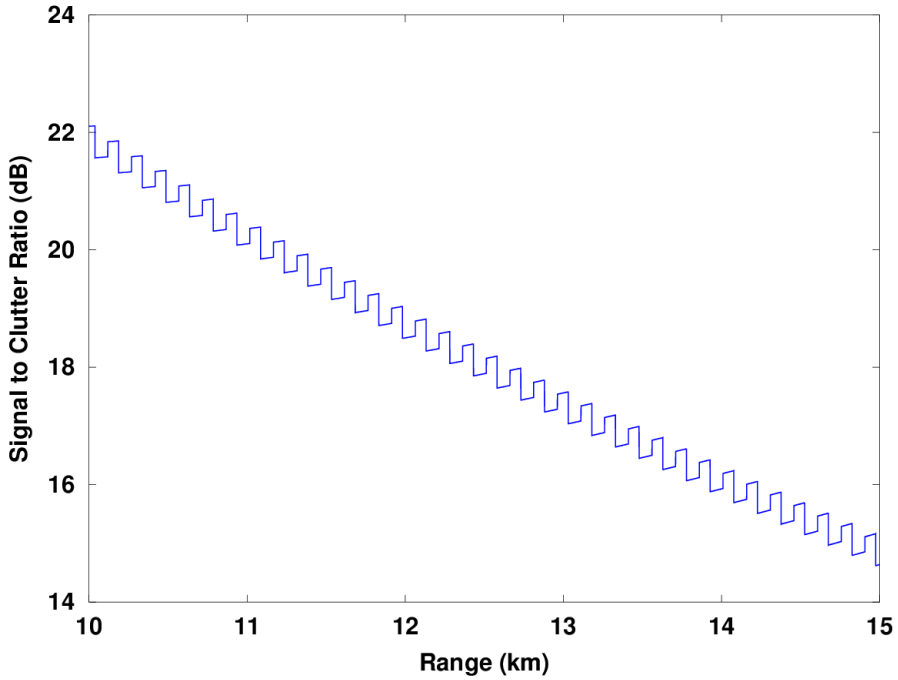

Figure B.8: Plot of SCR values for $\theta_{look} = 0°$

Figure B.8 shows what happens when the beam is transmitting horizontally ($\theta_{look} = 0°$). Here the SCR values are lower, from 22 dB to 15 dB, due to the beam illuminating more of the ground and this results in a higher clutter power.

In the spherical earth geometry, the grazing angles were calculated using Eq. B.4. With the radar at 5 m and at ranges of between 10 and 15 km, the grazing angles are quite small and this results in low values of σ_c. In other words, the scenario assumes that there is no undulation on the earth's surface. Therefore, for a

more worst case scenario, undulation is incorporated onto the earth's surface by assuming a constant grazing angle of 60°. Figure B.9 shows the SCR values obtained when incorporating undulation, while still maintaining a horizontal beam. Because the values of σ_c are higher, this results in a higher clutter power and therefore SCR values that are significantly lower, from -2 dB to -9 dB, which reflect conditions of sub-clutter visibility.

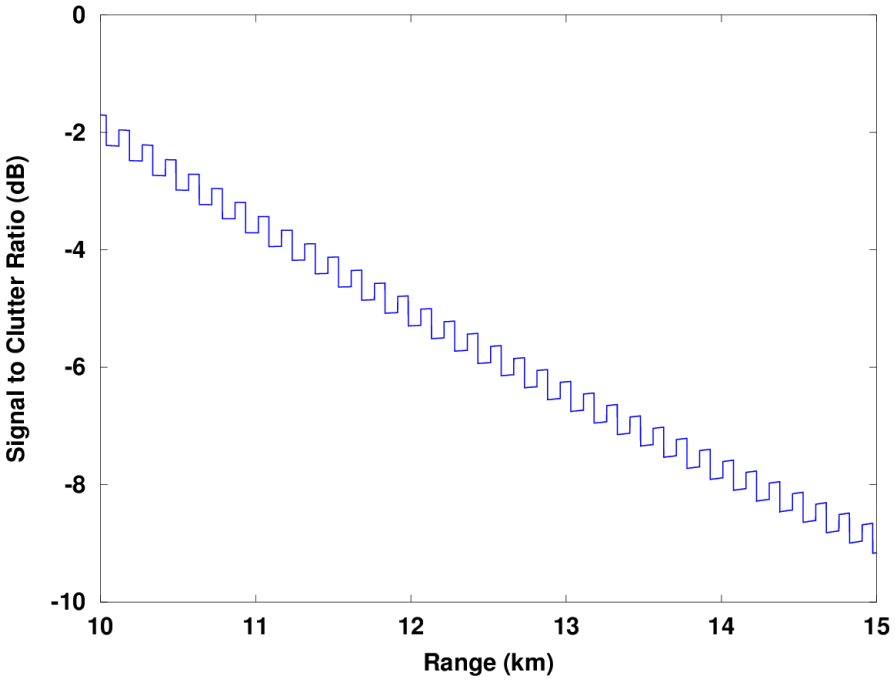

Figure B.9: Plot of SCR values with undulation incorporated ($\theta_{gr} = 60°$)

In the simulations shown thus far, a PRF of 1 kHz was assumed. In practice, higher PRFs are needed so as to deal with faster targets such as aircraft. Therefore Table B.3 and B.4 show the values of SCR calculated for different PRFs. Table B.3 shows the results for a target RCS of 1 m^2 while Table B.4 shows the results for a target RCS of 10 m^2. The SCR values in Table B.4 are higher due to the higher signal power involved. However, the SCR values at these PRFs are significantly more lower compared to the 1 kHz PRF case due to the fact that higher PRFs involve smaller transmitted pulse lengths. This means that the blind ranges are less and therefore ground returns that are more closer to

the radar are received and this results in a higher ground clutter power due to the inverse R^4 law.

Table B.3: SCR values for different PRF for $\sigma_t = 1m^2$

PRF	SCR at 10 km	SCR at 15 km
5 kHz	-20.172	-27.729
10 kHz	-25.963	-33.996
20 kHz	-32.945	-38.615

Table B.4: SCR values for different PRF for $\sigma_t = 10m^2$

PRF	SCR at 10 km	SCR at 15 km
5 kHz	-10.172	-17.729
10 kHz	-15.963	-23.996
20 kHz	-22.945	-28.615

Bibliography

[1] A. Wilkinson, R. Lord, and M. Inggs, "Stepped-frequency processing by reconstruction of target reflectivity spectrum," in *Communications and Signal Processing, 1998. COMSIG '98. Proceedings of the 1998 South African Symposium on*, pp. 101–104, 1998.

[2] Z. Liu and S. Zhang, "A novel method of translational motion compensation for hopped-frequency isar imaging," in *Radar Conference, 2000. The Record of the IEEE 2000 International*, pp. 255–260, 2000.

[3] Y. Liu, H. Meng, G. Li, and X. Wang, "Range-velocity estimation of multiple targets in randomised stepped-frequency radar," *Electronics Letters*, vol. 44, pp. 1032–1034(2), August 2008.

[4] S. R. J. Axelsson, "Analysis of random step frequency radar and comparison with experiments," *Geoscience and Remote Sensing, IEEE Transactions on*, vol. 45, no. 4, pp. 890–904, 2007.

[5] J. Högbom, "Aperture synthesis with a non-regular distribution of interferometer baselines," *Astron. Astrophys. Suppl*, vol. 15, no. 1974, pp. 417–426, 1974.

[6] "Ieee standard radar definitions," *IEEE Std 686-2008 (Revision of IEEE Std 686-1997)*, pp. c1–41, May 2008.

[7] A. Stanton and W. Nel, "Investigation into the use of high range resolution (hrr) waveforms for velocity estimation of scatterers," *CSIR internal report*, feb. 2012.

[8] F. Prodi and E. Tilli, "Motion compensation for a frequency stepped radar," in *Waveform Diversity and Design Conference, 2007. International*, pp. 255–259, 2007.

[9] E. Tilli and F. Prodi, "Use of HRR data for target acceleration estimation: A simple but effective approach," in *Radar Conference, 2008. EuRAD 2008. European*, pp. 224–227, 2008.

[10] Y. Liu, H. Meng, H. Zhang, and X. Wang, "Motion compensation of moving targets for high range resolution stepped-frequency radar," *Sensors*, vol. 8, no. 5, pp. 3429–3437, 2008.

[11] G. Schwarz, "Estimating the dimension of a model," *The Annals of Statistics*, vol. 6, pp. 461–464, 03 1978.

[12] Y. Liu, H. Meng, G. Li, and X. Wang, "Velocity Estimation and Range Shift Compensation for High Range Resolution Profiling in Stepped-Frequency Radar," *Geoscience and Remote Sensing Letters, IEEE*, vol. 7, no. 4, pp. 791–795, 2010.

[13] T. Huang, Y. Liu, G. Li, and X. Wang, "Randomized stepped frequency isar imaging," in *Radar Conference (RADAR), 2012 IEEE*, pp. 0553–0557, 2012.

[14] A. De Freitas and J. de Villiers, "Multiple scatterer tracking in high range resolution radar," in *Information Fusion (FUSION), 2012 15th International Conference on*, pp. 1683–1688, IEEE, 2012.

[15] S. Sussman, "Least-square synthesis of radar ambiguity functions," *Information Theory, IRE Transactions on*, vol. 8, no. 3, pp. 246–254, 1962.

[16] J. Wolf, G. Lee, and C. Suyo, "Radar waveform synthesis by mean square optimization techniques," *Aerospace and Electronic Systems, IEEE Transactions on*, vol. AES-5, no. 4, pp. 611–619, 1969.

[17] I. Gladkova, "Zak transform and a new approach to waveform design," *Aerospace and Electronic Systems, IEEE Transactions on*, vol. 37, no. 4, pp. 1458–1464, 2001.

[18] I. Gladkova, "Design of frequency modulated waveforms via the zak transform," *Aerospace and Electronic Systems, IEEE Transactions on*, vol. 40, no. 1, pp. 355–359, 2004.

[19] H. Griffiths and L. Vinagre, "Design of low-sidelobe pulse compression waveforms," *Electronics Letters*, vol. 30, no. 12, pp. 1004–1005, 1994.

[20] E. De Witte and H. Griffiths, "Improved ultra-low range sidelobe pulse compression waveform design," *Electronics Letters*, vol. 40, no. 22, pp. 1448–1450, 2004.

[21] J. E. Cilliers and J. C. Smit, "Pulse compression sidelobe reduction by minimization of l¡ sub¿ p¡/sub¿-norms," *Aerospace and Electronic Systems, IEEE Transactions on*, vol. 43, no. 3, pp. 1238–1247, 2007.

[22] S. Budišin, "Efficient pulse compressor for golay complementary sequences," *Electronics Letters*, vol. 27, no. 3, pp. 219–220, 1991.

[23] A. Pezeshki, A. R. Calderbank, W. Moran, and S. D. Howard, "Doppler resilient golay complementary waveforms," *Information Theory, IEEE Transactions on*, vol. 54, no. 9, pp. 4254–4266, 2008.

[24] F. J. Harris, "On the use of windows for harmonic analysis with the discrete fourier transform," *Proceedings of the IEEE*, vol. 66, no. 1, pp. 51–83, 1978.

[25] H. C. Stankwitz, R. J. Dallaire, and J. R. Fienup, "Nonlinear apodization for sidelobe control in sar imagery," *Aerospace and Electronic Systems, IEEE Transactions on*, vol. 31, no. 1, pp. 267–279, 1995.

[26] B. Sarkar, R. Panigrahi, and A. Mishra, "Sidelobe suppression in wigner distribution using non-linear apodization," in *India Conference (INDICON), 2009 Annual IEEE*, pp. 1–4, 2009.

[27] J. Tsao and B. D. Steinberg, "Reduction of sidelobe and speckle artifacts in microwave imaging: the clean technique," *Antennas and Propagation, IEEE Transactions on*, vol. 36, no. 4, pp. 543–556, 1988.

[28] M. Martorella, N. Acito, and F. Berizzi, "Statistical clean technique for isar imaging," *Geoscience and Remote Sensing, IEEE Transactions on*, vol. 45, no. 11, pp. 3552–3560, 2007.

[29] R. Bose, A. Freedman, and B. D. Steinberg, "Sequence clean: A modified deconvolution technique for microwave images of contiguous targets," *Aerospace and Electronic Systems, IEEE Transactions on*, vol. 38, no. 1, pp. 89–97, 2002.

[30] R. Bose, "Sequence clean technique using bga for contiguous radar target images with high sidelobes," *Aerospace and Electronic Systems, IEEE Transactions on*, vol. 39, no. 1, pp. 368–373, 2003.

[31] Z. She and Z. Zhu, "Cross-range scaling of inverse synthetic aperture radar," in *Aerospace and Electronics Conference, 1994. NAECON 1994., Proceedings of the IEEE 1994 National*, pp. 175–180, IEEE, 1994.